

Meteorological Research Institute-Earth System Model Version 1 (MRI-ESM1)
— Model Description —

BY

Seiji Yukimoto, Hiromasa Yoshimura, Masahiro Hosaka, Tomonori Sakami,
Hiroyuki Tsujino, Mikitoshi Hirabara, Taichu Y. Tanaka, Makoto Deushi,
Atsushi Obata, Hideyuki Nakano, Yukimasa Adachi, Eiki Shindo, Shoukichi Yabu,
Tomoaki Ose and Akio Kitoh

気象研究所技術報告

第 64 号

気象研究所地球システムモデル第 1 版 (MRI-ESM1)

—モデルの記述—

行本誠史、吉村裕正、保坂征宏、坂見智法、
辻野博之、平原幹俊、田中泰宙、出牛真、
小畑淳、中野英之、足立恭将、新藤永樹、藪将吉、
尾瀬智昭、鬼頭昭雄

気 象 研 究 所

Preface

Climate models are used in various fields, for example, to study the mechanisms of the modern climate and its interannual variability, to make climate projections for the near future and for hundreds of years to come, and to conduct paleoclimate simulations. As our knowledge of climate processes has grown over the past few decades, the complexity of climate models has increased, and additional physics has been incorporated into them. In addition to atmospheric chemical processes such as those related to aerosols and ozone, feedback processes between the carbon cycle and climate change have now been incorporated into a climate model, called the Earth System Model (ESM).

The Meteorological Research Institute (MRI) of Japan has been developing models for many years, beginning with an atmospheric general circulation model (AGCM) developed in the 1980s. In the 1990s, we developed a global atmosphere–ocean coupled climate model (MRI-CGCM1) and performed climate projection experiments under an idealized global warming scenario. In the early 2000s, a new version of this CGCM (MRI-CGCM2) was developed by incorporating the spectral dynamical framework of the Japan Meteorological Agency operational model. A revised version of this model (MRI-CGCM2.3) was used in the 3rd phase of the Coupled Modeling Intercomparison Project, the results of which contributed to the 4th Assessment Report of the Intergovernmental Panel on Climate Change. Global climate change projection data produced by MRI CGCMs have also been used to derive the lateral boundary conditions for MRI regional climate models.

The first version of the MRI Earth System Model (MRI-ESM1) has now been developed. This model enables us to represent both the climate system and terrestrial and oceanic material transport, as well as their interaction. MRI-ESM1 is the base model for the fifth phase of the Coupled Modeling Intercomparison Project (CMIP5). It is my great pleasure to announce the completion of MRI-ESM1 and the publication of this technical report describing the model. MRI-ESM1 was developed at MRI under the special research program “Comprehensive Projection of Climate Change around Japan due to Global Warming (FY2005–FY2009).” Its development was made possible by the collaboration of participating scientists from several research laboratories and departments of the MRI. I would like to express here my deep gratitude for the huge efforts put forth by all of those who participated in the development of the model and the cooperation displayed among them. I expect that this model will produce many important scientific results.

Akio Kitoh

Director

Climate Research Department

序

将来の気候変動予測を行う道具である気候モデルは地球システムモデルへと発展を遂げ、現在の気候の再現と気候変動のメカニズム研究、温暖化予測さらには古気候研究など幅広い分野で用いられている。この 20 年間に、気候変動のメカニズム研究や気候予測に使われる気候モデルは、大気大循環のみのモデルから、海洋混合層を付加したモデル、大気海洋結合大循環モデル、植生モデルやエアロゾルモデル・大気化学モデルの付加、炭素循環モデルとの結合などがあり、今では地球システムモデルへと大いに発展してきた。最近では、エアロゾルが放射・雲・降水過程に及ぼす直接効果・間接効果を導入し、オゾンをはじめとした大気化学プロセスがオンラインで同時計算できるモデルが登場している。さらに温室効果ガスの排出シナリオを与え、海洋による二酸化炭素の吸収や陸上植生との炭素交換過程を計算し、大気中の二酸化炭素濃度の変化とそれによる気温・降水量変化から炭素交換過程へのフィードバックが見積もられるようになってきている。

気象研究所では、これまで長期にわたって全球気候モデルの開発を行ってきた。1980 年代には大気大循環モデルを開発し大気モデリング相互比較実験には当初から参加してきた。1990 年代にはいると、大気大循環モデルに全球海洋大循環モデルを結合した全球大気海洋結合モデル MRI-CGCM1 を開発し、温暖化予測実験を行った。その後、2000 年代初頭には、それまでの格子モデルから、新たに気象庁現業モデルを基に開発したスペクトル大気大循環モデルを導入し、全球大気海洋結合モデル MRI-CGCM2 を開発し、温室効果気体と硫酸エアロゾルの直接効果のシナリオ実験を行った。その MRI-CGCM2 にいくつかの改良が加えられた MRI-CGCM2.3 では、第 3 期気候モデル比較プロジェクト CMIP3 に参加し、気候変動に関する政府間パネル(IPCC)第 4 次評価報告書に貢献してきた。これら各世代の全球気候モデルによる気候変化予測の結果は、気象研究所における地域気候モデルによるダウンスケーリングにも用いられ、日本付近の気候変化予測に役立ってきた。

これらの歴史を背景に、気象研究所では気象庁気候変動予測研究費による特別研究「温暖化による日本付近の詳細な気候変化予測に関する研究」（平成 17 年度～平成 21 年度）を立ち上げ、その副課題として「温暖化予測地球システムモデルの開発」を、気候研究部、環境・応用気象研究部、海洋研究部の担当者により行ってきた。ここに気象研究所地球システムモデル MRI-ESM1 の完成を迎え、モデルの解説を気象研究所技術報告として出版できることは大なる喜びである。地球システムモデル開発は、多くのコンポーネントモデルを一つの目的のためにたばねる共同作業である。モデル開発関係者の多大な努力と協力に深く感謝の意を表す。今後、温暖化予測実験に留まらず、このモデルを用いた数多くの成果が出てくることを期待する。

気候研究部長

鬼頭昭雄

Abstract

The Meteorological Research Institute (MRI) of Japan developed the Earth System Model MRI-ESM1 to enable us to simulate both the climate system and global material transport, along with their interaction. Its core component, the atmosphere–ocean coupled global climate model MRI-CGCM3, represents a substantial advance from the previous model, MRI-CGCM2.3, which made important contributions to the fourth assessment report of the Intergovernmental Panel on Climate Change. The global atmospheric model MRI-AGCM3, used as the atmospheric component of MRI-CGCM3, incorporates various new physical parameterizations, including a cumulus convection scheme, a high-accuracy radiation scheme, a two-moment bulk cloud model that explicitly represents aerosol effects on clouds, and a new, sophisticated land-surface model, into the dynamics framework by a conservative semi-Lagrange method. MRI.COM3, also newly developed at MRI, is used for the global ocean-ice component of MRI-CGCM3. We adopted for MRI.COM3 a tripolar grid coordinate system, in which the North Pole is not a singular point, because MRI.COM3 supports general orthogonal curvilinear coordinates. The sea-ice model has also been updated; it now represents the sub-grid ice-thickness distribution by thickness categories, and incorporates ice rheology dynamics in addition to detailed thermodynamics. The MASINGAR mk-2 aerosol model takes into account five kinds of atmospheric aerosols, sulfate, black and organic carbon, mineral dust, and sea salt. The MRI-CCM2 atmospheric chemistry climate model (ozone model) is used to treat chemical reactions and the transport of atmospheric species associated with both tropospheric and stratospheric ozone. To represent the global carbon cycle, terrestrial ecosystem carbon cycle and ocean biogeochemical carbon cycle processes are incorporated into the land-surface model and the ocean model, respectively. The Scup coupler developed at MRI is used to integrate each component model, the atmospheric, ocean, aerosol, and ozone models, into MRI-ESM1. This flexible coupler can couple models with different resolutions and grid coordinates with variable coupling intervals. This advantage not only leads to efficient execution of the earth system model but also allows the efficient and independent development of the component models.

要旨

気象研究所において、気候システムと地球全体の物質循環、およびそれらの間の相互作用を再現する地球システムモデルが開発された。その中核となるコンポーネントである大気海洋結合全球気候モデル MRI-CGCM3 は、気候変動に関する政府間パネル（IPCC）の第4次評価報告書に大きく貢献した以前のモデル MRI-CGCM2.3 から大きく進歩した。MRI-CGCM3 の大気部分としては、全球大気モデル MRI-AGCM3 が用いられており、積雲対流スキーム、高精度な放射スキーム、エーロゾルの雲への影響を陽に表現する2モーメントバルク雲モデル、さらに、新しく精緻な陸面モデルなど、種々の新しい物理過程パラメタリゼーションが、セミ・ラグランジュ法による力学フレームに組み込まれている。MRI-CGCM3 の海洋・海水部分として、これも新しく気象研究所で開発された MRI.COM3 が用いられている。MRI.COM3 では一般直交曲線座標をサポートしているため、ここでは北極が特異点にならない3極座標系を採用している。海氷モデルも新しくなり、詳細な熱力学過程に加え、格子内の氷厚分布をカテゴリーで表現し、また氷の粘塑性体力学も取り入れている。エーロゾルモデルの MASINGAR mk-2 は、硫酸、黒色炭素、有機炭素、鉱物ダスト、および海塩の5種類の大気エーロゾルを扱っている。大気化学気候モデル（オゾンモデル）である MRI-CCM2 は、成層圏および対流圏オゾンに関連する大気化学種の反応および輸送を扱うために用いられている。全球の炭素循環を表現するため、陸域炭素循環および海洋生物地球化学炭素循環過程が、それぞれ陸面モデルおよび海洋モデルに組み込まれている。カップラーScup は気象研究所で開発され、大気、海洋、エーロゾル、およびオゾンの各コンポーネントモデルを統合して MRI-ESM1 として構成するために用いられている。この柔軟性のあるカップラーは異なる解像度、格子座標を様々な結合間隔で結合することを可能にしている。このような特長は、地球システムモデルの効率的な実行を可能にするだけでなく、コンポーネントモデルを効率的に独立して開発することも可能にしている。

Contents

1. Introduction	1
2. Outline of MRI-ESM1	4
3. Atmospheric model (MRI-AGCM3)	8
3.1. Dynamics framework	8
3.2. Cumulus convection	15
3.3. Radiation	22
3.4. Cloud model	25
3.5. Planetary boundary layer	28
3.6. Land surface models	30
3.7. Ocean surface processes	33
3.8. River and lake model	36
4. Ocean-ice model (MRI.COM3)	38
4.1. Ocean model	38
4.2. Sea ice model	42
4.3. Exchange of properties with the atmospheric component	47
5. Aerosol model (MASINGAR mk-2)	50
5.1. Coupling with the atmospheric general circulation model MRI-AGCM3	50
5.2. Coupling with the chemistry climate model MRI-CCM2	51
5.3. Processes in the global aerosol model	51
6. Atmospheric (Ozone) chemistry model (MRI-CCM2)	57
7. Ice-sheet and Iceberg discharge	60
8. Carbon cycle	61
8.1. Terrestrial carbon cycle	61
8.2. Oceanic Carbon Cycles	64
9. Coupler (Scup)	69
References	71

1. Introduction

Climate models are the most important tools available today for enhancing our scientific understanding of the great complexity of the climate system and for projection of future climate change. The Meteorological Research Institute (MRI) of Japan has been developing climate models for several decades. The first atmospheric general circulation model (AGCM), referred to as MRI-GCM-I (Tokioka et al., 1984; Kitoh et al., 1995), was coupled to a global ocean general circulation model (OGCM) (Nagai et al., 1992) to create MRI's first-generation atmosphere–ocean coupled global climate model (MRI-CGCM1). Tokioka et al. (1995) used MRI-CGCM1 to conduct a global warming experiment in which they examined transient responses to a cumulative increase in the atmospheric carbon dioxide (CO₂) concentration of 1%/year. The results of this experiment contributed to the 2nd Assessment Report of the Intergovernmental Panel on Climate Change (IPCC, 1996). A global spectral AGCM developed from the operational weather prediction model of the Japan Meteorological Agency (JMA) with a horizontal resolution of ~280 km was used to replace the earlier AGCM grid (4° × 5° horizontal resolution) in MRI-CGCM1. The resulting model became MRI's second-generation CGCM, MRI-CGCM2 (Yukimoto et al., 2001). Several climate change projection experiments (Noda et al., 2001) based on scenarios forced by greenhouse gases and sulfate aerosol concentrations were conducted with MRI-CGCM2. An improved version of the MRI-CGCM2 (MRI-CGCM2.3; Yukimoto et al., 2006) was used in the 3rd phase of the Coupled Model Intercomparison Project (CMIP3) of the World Climate Research Programme, which compared 23 models from institutions around the world. In this intercomparison, MRI-CGCM2.3 was found to exhibit excellent climate reproducibility, which led to its being a significant contributor to the 4th Assessment Report of the IPCC (IPCC-AR4; IPCC, 2007).

Climate change projection results from each generation of MRI's CGCM have been downscaled with providing boundary conditions to regional climate models (e.g., Sasaki et al., 2006; Takayabu et al., 2007), which, when utilized for detailed projections of climate change, have performed well in simulating the climate around Japan.

The projections of future climate change in IPCC-AR4 were based on numerous experiments with more than 20 CGCMs that yielded results with quantitative confidence levels. As a result, IPCC-AR4 contained a stronger conclusion than the previous assessment reports. That stronger statement was possible because many of the participating models were able to account for the observed climate

change in the twentieth century, which suggests that these models can predict future climate change with higher confidence than before. The range of the uncertainties in the projections, however, remained as large as in the 3rd Assessment Report (IPCC, 2001), and the main source of the uncertainty in climate sensitivity was caused by cloud feedback. Bony and Dufresne (2005) suggested that the different responses of low clouds over subtropical oceans to global warming among the simulations was the most important factor causing the sensitivity spread among the models. The uncertainty related to aerosols radiative forcing was also a large uncertainty factor. In particular, there are many questions about the modeling of the indirect effects of aerosols, which must take into account sophisticated cloud microphysics (involving a large computational cost). In addition, climate models are now expected to represent important interactions between climate and atmospheric chemistry, for instance, ozone changes associated with climate change and anthropogenic trace gases such as chlorofluorocarbons (CFCs), and volcanic impacts on climate.

Also important is the accurate quantitative estimation of feedback processes between the carbon cycle and climate change. IPCC-AR4 estimated this feedback by using earth system models of intermediate complexity, which are simplified, low-resolution models. A more realistic earth system model (ESM) based on a CGCM that incorporates the full complexity of physical processes, with sufficiently high resolution, and sophisticated carbon cycle process simulation is required to achieve a more accurate quantitative estimation of this feedback.

A major theme of the next IPCC Assessment Report, IPCC-AR5 (which will have CMIP5 as its scientific basis, and is expected to appear in 2013), in addition to the long-term projections (~2100 and later) as presented in past IPCC reports, is near-term prediction, targeting climate change 20 to 30 years in the future and including the prediction of decadal variability as an initial value problem. More regionally precise information on climate change in the near future is required for near-term projection, and climate models must be able to accurately reproduce the decadal to multi-decadal variability observed in the latter half of the twentieth century, as well as the present-day mean climate.

Earth system models for IPCC-AR5 have been developed at several climate modeling centers. An ESM has also been developed at MRI under the special research program "Comprehensive Projection of Climate Change around Japan due to Global Warming." In conjunction with the ESM development, a global AGCM has been developed at MRI in collaboration with JMA and the Advanced Earth Science and Technology Organization. This AGCM has performed well in reproducing the overall atmospheric

fields (Mizuta et al., 2006). A very high resolution (20-km mesh) version of the AGCM has produced many excellent present and future climate simulation results with regard to, for example, typhoons (Oouchi et al., 2006), the Baiu (Kusunoki et al., 2006), regional climate, and extreme events. This report describes the ESM that MRI has developed, called MRI-ESM1, which incorporates these successful results, in preparation for the CMIP5 experiments that will contribute to IPCC-AR5.

2. Outline of MRI-ESM1

The configuration of MRI-ESM1 is illustrated in Fig. 1. The atmosphere–ocean coupled model forming its core component is MRI-CGCM3, which itself consists of MRI’s latest AGCM and OGCM versions. The AGCM includes terrestrial biosphere carbon cycle processes, and the OGCM includes ocean biogeochemical processes. Transports and exchanges of atmospheric CO₂ at the land and ocean surfaces integrate the terrestrial and ocean carbon cycles, allowing representation of the global carbon cycle. The AGCM is coupled with an aerosol model and an atmospheric chemistry–climate model (CCM) (focused on ozone chemistry), which allows representation of the interaction between climate and variations in several aerosols, ozone, and trace gases. Not only is the CCM coupled with the AGCM, the aerosol model and the CCM are coupled with each other, which enables simulation of interactions such as heterogeneous chemical reactions on aerosol surfaces.

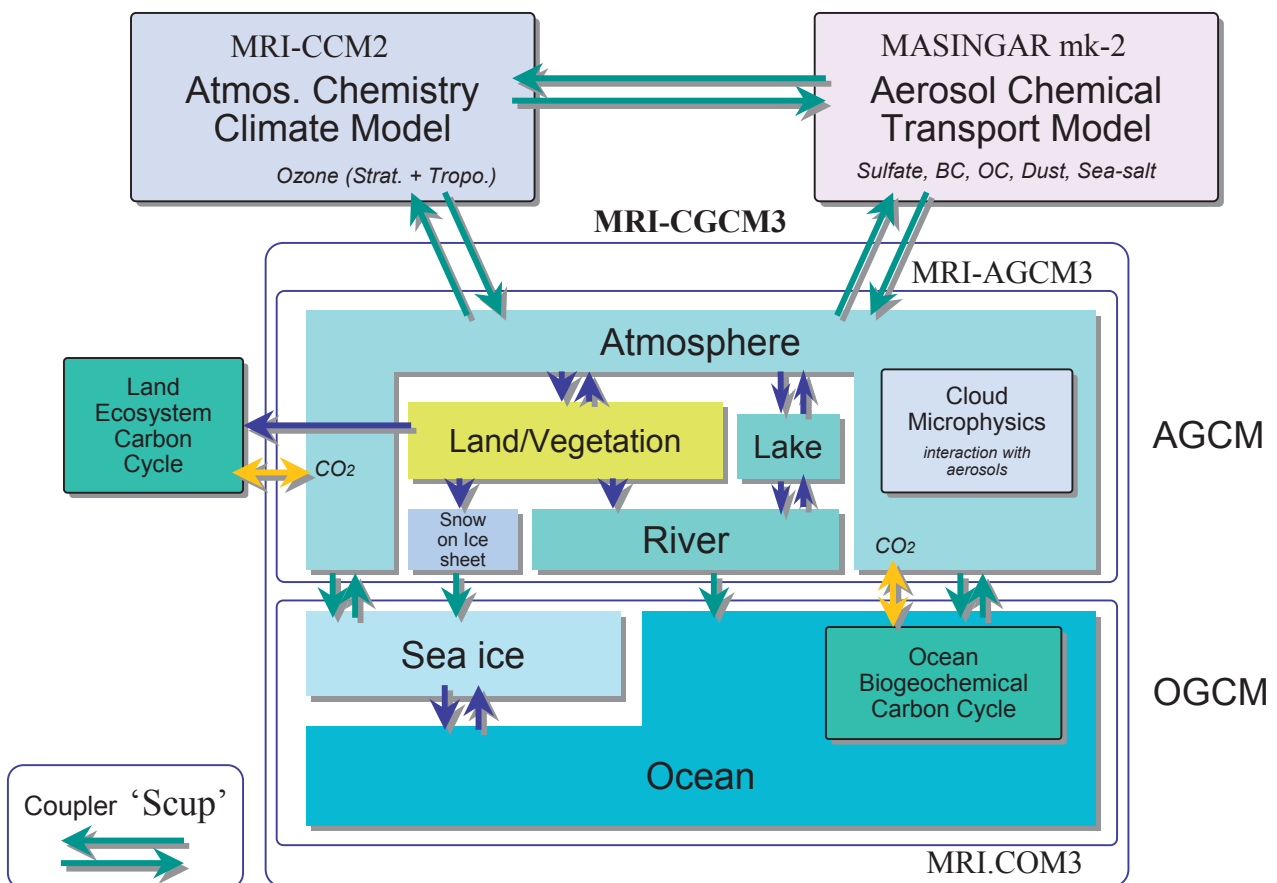


Figure 1 Configuration of the component models in MRI-ESM1. Green arrows denote data exchange with using Scup between the component models.

The AGCM, called MRI-AGCM3, was developed at MRI (Mizuta et al., 2006) and is based on JMA's operational weather prediction model. Its dynamics framework uses a semi-Lagrangian method (Yoshimura, in preparation; see Section 3.1) that has the important advantages of computational efficiency and good conservational properties for mass, static energy, and any tracers. In addition to the parameterizations of the operational model, many new or improved parameterizations of various physical processes have been developed. In particular, new parameterization schemes for important processes, cumulus convection, radiation, clouds, the planetary boundary layer (PBL), and terrestrial hydrology have been introduced. These newly introduced schemes are incorporated as optional alternatives to the conventional schemes.

For cumulus convection, either a new scheme developed by Yoshimura et al. (in preparation; see Section 3.2.2) or a Kain-Fritsch scheme (e.g., Kain and Fritsch, 1990; Section 3.2.3) can be selected, or a prognostic Arakawa-Schubert-type scheme, which was modified from the original scheme (e.g., Arakawa and Schubert, 1974; Randall and Pan, 1993a, 1993b) for the operational model. For radiation processes, the parameterization scheme used in the operational model (see Section 3.3) has been introduced as an alternative to the scheme used in MRI-CGCM2.3 (Shibata and Aoki, 1989; Shibata and Uchiyama, 1992). A cloud microphysics scheme has also been incorporated into MRI-AGCM3 so that the indirect effects of aerosols on radiative forcing can be represented. This cloud microphysics scheme is a two-moment bulk formulation (Section 3.4) that explicitly represents two concentrations, i.e., mass (mixing ratio) and number concentrations, separately for cloud droplets and ice crystals. To model the PBL, in addition to the conventional Mellor-Yamada (Mellor and Yamada, 1974) level 2 scheme, a modification of that scheme developed by Nakanishi (2001) and Nakanishi and Niino (2004, 2006, 2009) (Section 3.5) can now be selected. A new land-surface model called HAL (Hosaka, in preparation; Section 3.6) has been developed that can handle arbitrary numbers of snow and soil layers and mosaic vegetation types, and it allows individual property parameters to be set for special land-surface types such as rice fields and urban areas. This land-surface model is much more flexible than that in MRI-CGCM2.3, which is a simple biosphere model (SiB: Sellers et al., 1986; Sato et al., 1989) modified to handle more soil layers (Hirai et al., 2007). River channels and lakes are also modeled (Section 3.8) as part of a closed global water cycle.

The ocean component of MRI-CGCM3 is a global version of MRI.COM3 (Tsujino et al., 2010; Section 4) developed at MRI that supports general orthogonal curvilinear coordinates. We employ a

tripolar coordinate system that does not have the North Pole as a singular point, because MRI-ESM1 covers the world's oceans, including the Arctic Ocean; south of latitude 64°N, the coordinate axes parallel latitude and longitude. A sophisticated sea-ice model was introduced in MRI.COM3, following the Los Alamos sea-ice model (CICE; Hunke and Lipscomb, 2006), which formulates dynamics processes such as categorized thickness distribution, ridging, and rheology, in addition to the thermodynamics processes in the sea ice model of MRI-CGCM2.3, which was based on a free-drift model developed by Mellor and Kantha (1989).

The aerosol model, called MASINGAR mk-2 (Section 5), is an advanced version of MASINGAR (Tanaka et al., 2003). The model handles five types of aerosols: sulfate, black carbon, organic carbon, mineral dust, and sea salt. For mineral dust and sea salt, the aerosols are calculated for several particle size bins. Processes related to aerosols treated in the model include natural and anthropogenic sources, chemical reactions in the air, transport, diffusion and mixing by atmospheric circulation and convection, and dry and wet deposition.

The atmospheric chemistry climate model MRI-CCM1 (Shibata et al., 2005), which was developed at MRI, primarily targets ozone in the stratosphere. The version incorporated into MRI-ESM1, MRI-CCM2 (Deushi and Shibata, 2010; Section 6), is based on MRI-CCM1, but the number of chemical species and (photo) chemical reactions that the model can handle is expanded, allowing MRI-CCM2 to simulate both tropospheric and stratospheric ozone. MRI-CCM2 can be coupled with the MASINGAR mk-2 aerosol model, which enables the ESM to simulate chemical–aerosol interactions, such as heterogeneous chemical reactions at the aerosol surface. For example, the effects of a stratospheric aerosol derived from a volcanic eruption on stratospheric ozone behavior can be taken into account.

One of the most important targets of ESMs is the global carbon cycle, which comprises mainly (at least on timescales of centuries up to a millennium) terrestrial biosphere carbon cycle processes, ocean biogeochemical processes, surface exchange and transport by atmospheric circulation, and anthropogenic emissions. The chemical creation of CO₂ in the atmosphere (calculated by MRI-CCM2), though it is a very small amount, is also included. Two optional schemes are available for parameterization of terrestrial biosphere carbon cycle processes. One is a simple scheme that uses empirical formulae based on air and soil temperatures and precipitation (Obata, 2007). The other is a more sophisticated scheme that takes into account photosynthesis related to vegetation represented by the land-surface model (Obata, in preparation; Section 8.1). For ocean biogeochemical processes, there

are also two options: a simple model developed by Obata and Kitamura (2003), and a more complex scheme that explicitly calculates nitrate (i.e., nutrients), phytoplankton, zooplankton, and detritus (Section 8.2). The integrated land and ocean carbon cycle scheme into MRI-ESM1 realistically simulates the exchange of carbon at the land or ocean surface with the atmosphere (CO₂ flux) and the three-dimensional redistribution of the altered atmospheric CO₂ concentration by processes such as advection, vertical mixing due to diffusion, and cumulus convection.

An ESM generally consists of a number of complex components, each of which is independently developed by a specialized modeling group, and the component models must work together. For efficient development, it must be possible to integrate the component models into the ESM without any troublesome modification being required. One of the most important strong points of MRI-ESM1 is that the component models can be flexibly coupled with the Scup coupler (Yoshimura and Yukimoto, 2008; Section 9). Scup allows the flexible exchange of data between component models with different resolutions or grid coordinates and different time intervals. The data exchange, moreover, is done with good conservation of both three-dimensional data and horizontal two-dimensional data, which is essential for climate models and ESMs. This functionality means that MRI-ESM1 can perform the many kinds of experiments planned for CMIP5 by flexible configuration of the component models and parameterization schemes.

3. Atmospheric model (MRI-AGCM3)

The atmospheric component (including land and ocean surfaces) model, MRI-AGCM3, was developed from a model by Mizuta et al. (2006) by the addition of a number of physical parameterization options and improvements, summarized in Table 1. The dynamics framework of MRI-AGCM3, which Mizuta et al. (2006) did not document in detail, is described in Section 3.1. In the subsequent sections, the major physical parameterizations developed for MRI-AGCM3 are described: cumulus convection (Section 3.2), radiation (Section 3.3), cloud model (Section 3.4), PBL (Section 3.5), land-surface model (Section 3.6), ocean surface processes (Section 3.7), and river-lake model (Section 3.8). Other components of MRI-AGCM3 are basically the same as in the original model of Mizuta et al. (2006).

3.1. Dynamics framework

In the MRI-AGCM3 global spectral atmospheric model, hydrostatic primitive equations are used as prognostic equations. A two-time-level semi-implicit semi-Lagrangian scheme is used for time integration. This scheme permits a longer time-step than the formerly used semi-implicit Eulerian scheme and realizes high efficiency. The vertically conservative semi-Lagrangian advection scheme is also globally conservative and therefore suitable not only for short-term weather predictions but also for long-time-period integrations such as experiments for projecting climate change.

The prognostic equations are given in Section 3.1.1, the vertically conservative semi-Lagrangian scheme is explained in Section 3.1.2, and the time integration scheme is described in Section 3.1.3.

3.1.1. Prognostic equations

The following hydrostatic primitive equations are used as prognostic equations.

$$\frac{\partial}{\partial t} \left(\frac{\partial p}{\partial \eta} \right) + \nabla \cdot \left(\mathbf{v}_H \frac{\partial p}{\partial \eta} \right) + \frac{\partial}{\partial \eta} \left(\dot{\eta} \frac{\partial p}{\partial \eta} \right) = 0 \quad (3.1)$$

$$\frac{dq}{dt} \equiv \frac{\partial}{\partial t} q + \mathbf{v}_H \cdot \nabla q + \dot{\eta} \frac{\partial}{\partial \eta} q = P_q \quad (3.2)$$

$$\frac{dT}{dt} = F_T + P_T + K_T \quad (3.3)$$

Table 1. List of MRI-AGCM3 options

Scheme/Model	Option name	References
Dynamics	1. Euler (obsolete)	JMA (2002)
	2. Semi-Lagrange	Section 3.1
Cumulus convection	1. AS type	Section 3.2.1, JMA (2002)
	2. Yoshimura	Section 3.2.2
	3. KF type	Section 3.2.3
Radiation	1. Shibata	Shibata and Aoki (1989) Shibata and Uchiyama (1992)
	2. JMA2004R1	Section 3.3
Cloud	1. Smith	Smith (1990)
	2. Tiedtke	Tiedtke (1993)
	3. MRI-TMBC	Section 3.4
PBL	1. Mellor-Yamada	Section 3.5.1 Mellor and Yamada (1974, 1982)
	2. MYNN	Section 3.5.2 Nakanishi (2001), Nakanishi and Niino (2004)
	3. Non-local	Section 3.5.3 Troen and Mahrt (1986), Holtslag and Boville (1993).
Land surface	1. JMA/SiB	Sellers et al. (1986), Sato et al. (1989)
	2. SiB0109	Hirai et al. (2007)
	3. HAL	Section 3.6
Ocean surface	1. JMA	JMA (2002)
	2. MRI	Section 3.7
River and lake	0. OFF	N/A
	1. GRiveT	Section 3.8
Gravity wave drag	1. Iwasaki	Iwasaki et al. (1989)
	2. Hines (experimental)	Hines (1997)
Terrestrial carbon cycle	1. Obata_2007	Obata (2007)
	2. Obata_2010	Section 8.1

$$F_T \equiv \frac{\kappa T_v \omega}{[1 + (c_{pv}/c_{pd} - 1)q]p} \quad (3.3a)$$

$$\frac{d(\mathbf{v}_H + 2\boldsymbol{\Omega} \times \mathbf{r})}{dt} = \mathbf{F}_{v_H} + \mathbf{P}_{v_H} + \mathbf{K}_{v_H} \quad (3.4)$$

$$\mathbf{F}_{v_H} \equiv -\nabla\Phi - R_d T_v \nabla \ln p \quad (3.4a)$$

$$\frac{\partial\Phi}{\partial\eta} = -\frac{R_d T_v}{p} \frac{\partial p}{\partial\eta} \quad (3.5)$$

$$T_v \equiv T \left\{ 1 + \left(\frac{R_v}{R_d} - 1 \right) q \right\}. \quad (3.6)$$

Here, the following notations are used.

- t : Time
- p : Pressure
- p_s : Surface pressure
- η : Hybrid $p - \sigma$ vertical coordinate ($\sigma \equiv p/p_s$)
- $\dot{\eta}$: $\dot{\eta} \equiv d\eta/dt$
- \mathbf{v}_H : Horizontal wind
- q : Water vapor mixing ratio
- T : Temperature
- T_v : Virtual temperature
- R_d : Gas constant of dry air
- R_v : Gas constant of water vapor
- c_{pd} : Specific heat of dry air at constant pressure
- c_{pv} : Specific heat of water vapor at constant pressure
- ω : Vertical pressure at p coordinate, $\omega \equiv dp/dt$
- κ : $\kappa \equiv R_d/c_{pd}$
- F_T : Heating by adiabatic compression (expansion)
- \mathbf{F}_{v_H} : Pressure gradient force
- $P_q, P_T, \mathbf{P}_{v_H}$: Contribution by physical processes
- K_T, \mathbf{K}_{v_H} : Horizontal viscosity
- $\boldsymbol{\Omega}$: Angular velocity of the rotation of the earth

\mathbf{r} : Position vector from the center of the earth

∇ : Horizontal gradient on the η surface.

The η coordinate is a hybrid vertical coordinate that steadily changes from the terrain following σ coordinate near the surface to the p coordinate near the top (Simmons and Burridge, 1981). $\eta = \eta(p, p_s)$ is a monotonic function of p that satisfies $\eta(0, p_s) = 0$ and $\eta(p_s, p_s) = 1$. p can be defined as a function of η and p_s , and $A(\eta)$ and $B(\eta)$ are introduced to satisfy

$$p(\eta, p_s) = A(\eta) + B(\eta) \cdot p_s. \quad (3.7)$$

$A(\eta) = 0$ is satisfied in the lower layers near the surface (σ -coordinate), and $B(\eta) = 0$ is satisfied in the upper layers (p -coordinate).

3.1.2. Advection with a vertically conservative semi-Lagrangian scheme

The vertically conservative semi-Lagrangian scheme (briefly described by Yoshimura and Matsumura, 2003, 2005) is used for the advection calculation. The equation

$$\frac{\partial}{\partial t} q + \mathbf{v}_H \cdot \nabla q + \dot{\eta} \frac{\partial}{\partial \eta} q = 0 \quad (3.8)$$

is used to explain the calculation of the advection of q . Equation (3.8) is the same as Eq. (3.2) except that the right-hand side of Eq. (3.8) is 0 to simplify its explanation. The advection of T and \mathbf{v}_H , Eqs. (3.3) and (3.4), is calculated in basically the same way as that of q . From Eqs. (3.1) and (3.8),

$$\frac{\partial}{\partial t} \left(\frac{\partial p}{\partial \eta} q \right) + \nabla \cdot \left(\mathbf{v}_H \frac{\partial p}{\partial \eta} q \right) + \frac{\partial}{\partial \eta} \left(\dot{\eta} \frac{\partial p}{\partial \eta} q \right) = 0 \quad (3.9)$$

is derived, which is the conservation equation of water vapor. When $q = 1$, Eq. (3.9) is the same as Eq. (3.1), the mass conservation equation. From Eqs. (3.1) and (3.9),

$$\frac{d_H}{dt} \left(\frac{\partial p}{\partial \eta} \right) = -D \frac{\partial p}{\partial \eta} - \frac{\partial}{\partial \eta} \left(\dot{\eta} \frac{\partial p}{\partial \eta} \right) \quad (3.10)$$

$$\frac{d_H}{dt} \left(\frac{\partial p}{\partial \eta} q \right) = -D \frac{\partial p}{\partial \eta} q - \frac{\partial}{\partial \eta} \left(\dot{\eta} \frac{\partial p}{\partial \eta} q \right) \quad (3.11)$$

are derived, where $d_H/dt \equiv \partial/\partial t + \mathbf{v}_H \cdot \nabla$ represents horizontal advection and $D \equiv \nabla \cdot \mathbf{v}_H$ represents horizontal divergence.

Equations (3.10) and (3.11) are vertically discretized. There are K full levels in the vertical direction

and \mathbf{v}_H, T, q are positioned at each full level ($k=1, 2, 3, \dots, K$). η is positioned at the half levels ($k=1/2, 3/2, 5/2, \dots, K+1/2$), which are the boundaries between the full levels. At the lower boundary ($k=1/2$), $p=p_s$, $\eta=1$, and $\dot{\eta}=0$ are satisfied. At the upper boundary ($k=K+1/2$), $p=0$, $\eta=0$, and $\dot{\eta}=0$ are satisfied. From Eq. (3.7), the pressure at the half level is obtained by

$$p_{k-1/2} = A_{k-1/2} + B_{k-1/2} p_s. \quad (3.12)$$

Equations (10) and (11) are vertically discretized (integrated from $k+1/2$ to $k-1/2$) as

$$\frac{d_H}{dt}(\Delta p_k) = -D_k \Delta p_k - \left(\dot{\eta} \frac{\partial p}{\partial \eta} \right)_{k-1/2} + \left(\dot{\eta} \frac{\partial p}{\partial \eta} \right)_{k+1/2} \quad (3.13)$$

$$\frac{d_H}{dt}(\Delta p_k q_k) = -D_k \Delta p_k q_k - \left(\dot{\eta} \frac{\partial p}{\partial \eta} q \right)_{k-1/2} + \left(\dot{\eta} \frac{\partial p}{\partial \eta} q \right)_{k+1/2}, \quad (3.14)$$

where Δp_k is defined as

$$\Delta p_k \equiv p_{k-1/2} - p_{k+1/2}. \quad (3.15)$$

The left-hand sides of Eqs. (3.13) and (3.14) represent horizontal advection, the first terms on the right-hand sides represent horizontal divergence (convergence), and the second and third terms on the right-hand sides represent vertical flux.

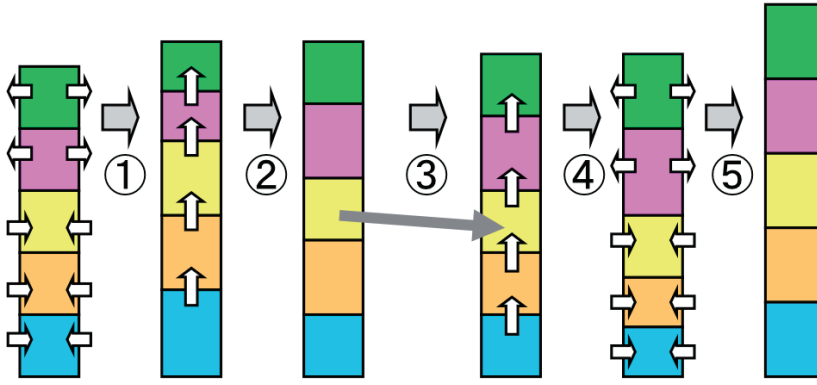
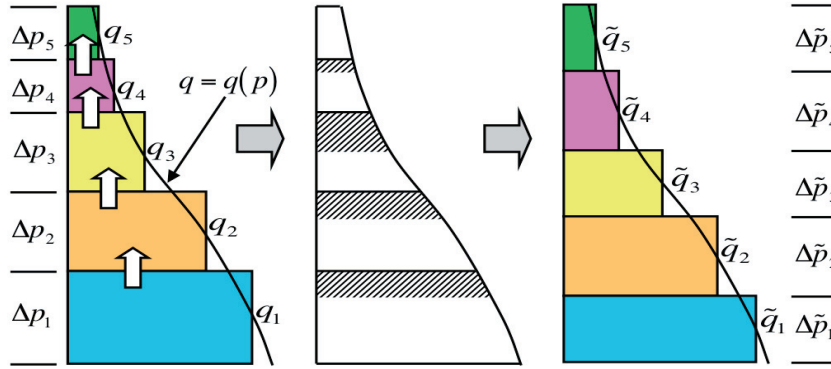
Three-dimensional advection is calculated by executing the time integration of these equations in the following order:

- ① Horizontal divergence
- ② Vertical flux
- ③ Horizontal advection
- ④ Vertical flux
- ⑤ Horizontal divergence.

Figure 2 shows the change in Δp_k due to the time integration of Eq. (3.13). The vertical flux (steps ② and ④) is calculated by the conservative semi-Lagrangian scheme. Figure 3 shows changes in Δp_k and q_k due to the vertical flux. The diagram on the left shows Δp_k and q_k before the vertical flux calculation. The distribution of $q = q(p)$ is obtained from q_k , which satisfies

$$\int_{p_{k+1/2}}^{p_{k-1/2}} q(p) dp = q_k \Delta p_k. \quad (3.16)$$

The hatched part of the diagram in the center of Fig. 3 represents q moving to the upper layer. The values of $\Delta \tilde{p}_k$ and \tilde{q}_k after the vertical flux calculation are shown in the right diagram. \tilde{q}_k is calculated as


 Figure 2 Change of Δp_k due to time integration in one time step

 Figure 3 Change of Δp_k and q before and after vertical flux calculation

$$\tilde{q}_k = \frac{1}{\Delta \tilde{p}_k} \int_{\tilde{p}_{k+1/2}}^{\tilde{p}_{k-1/2}} q(p) dp. \quad (3.17)$$

In the actual calculation, the integrated value from the upper boundary

$$Q(p) = \int_0^p q(p) dp \quad (3.18)$$

is used instead of $q(p)$ to make the calculation faster. The values of Q at the half levels are obtained from

$$Q(p_{k+1/2}) = \int_0^{p_{k+1/2}} q(p) dp = \sum_{l=k+1}^K q_l \Delta p_l \quad (3.19)$$

There are several methods for calculating the distribution of $Q(p)$ from $Q(p_{k+1/2})$ and q_k . To calculate material transport, such as of water vapor, the Piecewise Rational Method (PRM; Xiao and Peng, 2004), a monotonic and conservative method, is used. For the advection of T and \mathbf{v}_H , the cubic Lagrange interpolation method is used. $Q(\tilde{p}_{k+1/2})$ is obtained from the $Q(p)$ distribution, and \tilde{q}_k is calculated from

$$\tilde{q}_k = \frac{1}{\Delta \tilde{p}_k} \{Q(\tilde{p}_{k-1/2}) - Q(\tilde{p}_{k+1/2})\}, \quad (3.20)$$

which is derived from Eqs. (3.17) and (3.18).

This scheme for the vertical flux calculation is basically the same as that for the vertical coordinate transformation in the Scup coupler (Yoshimura and Yukimoto, 2008). The vertical flux calculation can also be considered a vertical coordinate transformation.

In step ③, the horizontal advection is calculated by a conventional semi-Lagrangian scheme. A quasi-cubic interpolation method (Ritchie et al., 1995) is used for horizontal interpolation. A quasi-fifth-order interpolation method is used only for the advection of horizontal wind, to improve precision. A correction method similar to that described by Priestley (1993) and by Gravel and Staniforth (1994) is used for global conservation in the calculation of material advection.

3.1.3. Time integration method

A generalized prognostic equation from Eqs. (3.1) through (3.4),

$$\frac{dX}{dt} = F(X), \quad (3.21)$$

is considered. A two-time-level semi-implicit semi-Lagrangian scheme (e.g., Temperton et al., 2001) and SETTLS (Hortal, 2002) are adopted to discretize Eq. (3.21) as

$$\frac{X^+ - X_D^0}{\Delta t} = \frac{1}{2} \{F^{(+)} + \beta(-L^0 + L^-)\}_D + \frac{1}{2} \{F^0 + \beta(-L^0 + L^+)\} \quad (3.22)$$

$$F^{(+)} \equiv 2F^0 - F^-, \quad (3.23)$$

where Δt is a time-step; $L(X)$ is the linearized term of $F(X)$; the subscript D means the three-dimensional departure point; the superscripts $-$, 0 , and $+$ mean past time ($t - \Delta t$), present time (t), and future time ($t + \Delta t$), respectively; and the superscript $(+)$ means the future time by time extrapolation. β is a second-order decentering parameter and is set to 1.2, slightly larger than 1.0, which enhances the stabilizing effect of the semi-implicit scheme. Since the right-hand side of Eq. (3.22) is the time average of the present time and the future time and the spatial average of the departure point and the arrival point, Eq. (3.22) has second-order precision in time and space. Equation (3.22) is transformed as

$$X^+ - \frac{1}{2}\beta\Delta t L^+ = \left[X^0 + \frac{1}{2}\Delta t \{F^{(+)} + \beta(-L^0 + L^-)\}_D \right] + \frac{1}{2}\Delta t \{F^0 + \beta(-L^0)\}. \quad (3.24)$$

The right-hand side of Eq. (3.24) is calculated explicitly. The value at the three-dimensional departure

point is obtained by the advection calculation with the vertically conservative semi-Lagrangian scheme. Since L^+ is a linear function of X^+ , X^+ can be obtained from Eq. (3.24). In spectral models, Eq. (3.24) can be solved independently of the horizontal wavenumber and therefore X^+ can be obtained easily.

3.2. Cumulus convection

3.2.1. Arakawa-Schubert-type scheme

The Arakawa-Schubert (AS)-type scheme (Arakawa and Schubert, 1974), one of the most popular for cumulus convection parameterization, is based on the assumption that there exists an ensemble (or group) of cumulus clouds at various heights in one grid column of the model, and that each individual cumulus cloud of the ensemble occupies a sufficiently small area of the grid. The updraft within the cumulus convection, by which heat and moisture are carried to the upper level while condensing the saturated moisture, and dry cold air from the surroundings is taken in (a process called entrainment), is parameterized by the cloud model. The generation of convection and its strength are determined by the destabilization of the grid-scale stratification, which is evaluated by the cloud work function (Arakawa and Schubert, 1974). The ensemble effect of the cumulus convection on the compensated subsidence and cloud top detrainment is parameterized by the cloud mass flux method. The JMA's operational scheme, though based on the original scheme of Arakawa and Schubert (1974), has been improved and developed variously.

Some of the modifications are the following:

1. A prognostic mass flux method is used to express the condition of away from quasi-equilibrium (Randall and Pan, 1993a, 1993b; Pan and Randall, 1993, 1998)
2. The cumulus downdraft is also considered (Cheng and Arakawa, 1997).
3. A mid-level convection scheme is included to express the mid-latitude convection accompanying the front and synoptic-scale disturbances.

Cumulus updraft

In an AS-type scheme, an ensemble of cumulus clouds at various heights is assumed, which the cloud base is at the top of the boundary layer. The prognostic equations for the cloud base mass flux are as follows:

$$A = \int_{z_B}^{z_T} g \frac{T^u - \bar{T}}{\bar{T}} \eta dz = \int_{z_B}^{z_T} g \frac{s^u - \bar{s}}{C_p \bar{T}} \eta dz \quad (3.25)$$

$$\frac{\partial M_B^u}{\partial t} = F(A, M_B^u) \quad (3.26)$$

Here A is the cloud work function; T^u and s^u are the temperature and the dry static energy, respectively, of a parcel in the cumulus updraft; T and s are the temperature and dry static energy, respectively, of the environment; M_B^u is the cloud base mass flux; and η is the standardized mass flux, which depends on the cloud base mass flux. F is the function of the damping formulation based on Randall and Pan (1993a, 1993b) and Pan and Randall (1998). Some modifications of function F are adopted in MRI-AGCM3. The top of each cumulus cloud corresponds to one vertical level in the model, and the ensemble size (i.e., the number of cumulus clouds) depends on the vertical resolution of the model.

In each cumulus cloud, an entrainment rate λ and a mass flux M^u is assumed:

$$\frac{1}{M^u} \frac{dM^u}{dz} = \lambda \quad (3.27)$$

so,

$$M^u = M_B^u \exp(\lambda(z - z_B)) \quad (3.28)$$

The suffix B refers to the cloud base level.

To reduce computational costs, Eq. (3.28) is linearized following Moorthi and Suarez (1992),

$$M^u = M_B^u (1 + \lambda(z - z_B)) = M_B^u \eta. \quad (3.29)$$

Therefore, the sub-grid-scale values of each cumulus cloud, such as the mass flux and entrainment rate and the cloud work function, can be estimated from the grid-scale values of these parameters. The cloud base mass flux M_B is a role of the closure in the AS parameterization. In MRI-AGCM3, the cloud base is fixed and it is assumed that detrainment occurs only from the cloud top. Additionally, a minimum value of λ is set, and a cumulus cloud with $\lambda = 0$ is excluded (Tokioka et al., 1988).

Cumulus downdraft

In convective clouds, there are not only a vertical updraft but also a strong downdraft, caused by cooling due to evaporation of raindrops and the loading of precipitation particles. Heating and drying of the lower layer become excessive, compared with observation, if this downdraft is not considered (Arakawa and Cheng, 1993), so it is necessary to parameterize it. In MRI-AGCM3, a simplified method instead of that of Arakawa and Cheng (1993) is used. The cumulus downdraft is expressed not as a cloud ensemble like the cumulus updraft but as a single cumulus cloud. The downdraft is assumed to start from a height that is above the cloud base and where the cloud base mass flux of the updraft becomes half.

It is also assumed that entrainment and detrainment rates have the same values above the cloud base and only the detrainment rate is considered beneath the cloud base.

Mid-level convection

Convection due to frontal system and mid-latitude synoptic-scale disturbances is not expressible with an AS-type scheme because that scheme assumes that the cloud base is above the boundary layer or at a fixed low level. Therefore, cumulus convection must be expressed by the root of the convection in such a free atmosphere. This is called a mid-level convection scheme.

The conditions associated with mid-level cumulus convection are as follows:

1. There should exist above the cloud base level a higher moist static energy than the one determined by the AS scheme.
2. This level is the cloud base of the mid-level cumulus convection.
3. There should exist an upward motion of the grid scale.

Only one cumulus cloud is assumed, and an ensemble is not considered. A constant entrainment rate is given beforehand, allowing the cloud top level and the vertical profile of the mass flux to be estimated.

The closure assumption is based on the cloud work function, but the buoyancy effect is strengthened according to the strength of the upward motion.

3.2.2. Yoshimura cumulus scheme

A new mass-flux-type cumulus scheme has also been developed (Yoshimura et al. in preparation; hereafter, the Yoshimura cumulus scheme) that considers an ensemble of convective updrafts between the minimum and maximum turbulent entrainment/detrainment rates. Traditional mass-flux-type cumulus schemes can be divided largely into two types: the AS type and the Tiedtke (1989) type. In an AS-type scheme, multiple convective updrafts with different heights depending on entrainment rates are explicitly calculated, but each updraft is represented as a simple entraining plume for computational efficiency. In a Tiedtke-type scheme, only a single convective updraft with a certain turbulent entrainment/detrainment rate is calculated, but the updraft is represented as a more detailed entraining and detraining plume. In the Yoshimura cumulus scheme, convective updrafts with the minimum and maximum entrainment/detrainment rates are calculated as detailed entraining and detraining plumes as in a Tiedtke-type scheme, and multiple convective updrafts with different heights as in an AS-type scheme are represented by considering continuous convective updrafts between the minimum and maximum turbulent entrainment/detrainment rates.

Convective updraft

In the Yoshimura cumulus scheme, organized entrainment, organized detrainment, turbulent entrainment, and turbulent detrainment are considered in the convective updraft (Fig. 4), as in the Tiedtke cumulus scheme.

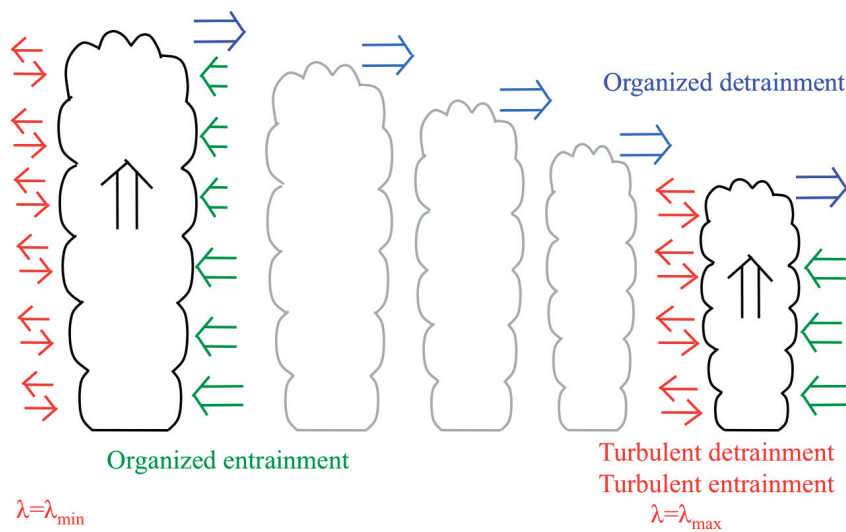


Figure 4 Schematic diagram for convective updraft. Red arrows indicate turbulent entrainment/detrainment. Green and blue arrows indicate organized entrainment and organized detrainment respectively. The left end (right end) is convective updraft with minimum entrainment rate λ_{\min} (maximum entrainment rate λ_{\max}). Convective updrafts between minimum and maximum entrainment rates are continuously present.

Two kinds of organized entrainment are considered. One is entrainment from a layer with large moist static energy from which updrafts originate. When the air with large moist static energy is in the boundary layer, the usual (deep or shallow) convection occurs. When it is above the boundary layer, mid-level convection occurs. The second kind is entrainment nearly proportional to the grid-scale mass convergence and the convective updraft mass flux.

Turbulent entrainment and detrainment are proportional to the convective updraft mass flux. The turbulent entrainment and detrainment rates are set to the same value. The minimum turbulent entrainment/detrainment rate λ_{min} is set to $0.5 \times 10^{-4} \text{ m}^{-1}$, and the maximum λ_{max} at the cloud bottom, is set to $3.0 \times 10^{-4} \text{ m}^{-1}$. Two convective updrafts, one with the minimum and one with the maximum turbulent entrainment/detrainment rates, are calculated. Convective updrafts between the minimum and maximum entrainment rates are assumed to be continuously present. Temperatures, virtual temperatures, water vapor mixing ratios, turbulent entrainment/detrainment rates, and other variables in the convective updrafts are obtained by linear interpolation between the two convective updrafts with the minimum and the maximum entrainment rates. When the virtual temperature of a convective updraft is lower than the virtual temperature in the environment at some vertical level, the convective updraft becomes negatively buoyant, leading to organized detrainment at that level.

In the Yoshimura cumulus scheme, the number of calculations is $O(N)$, where N is the number of vertical model levels. In an AS-type cumulus scheme, the number is $O(N^2)$ if each convective updraft is calculated as a detailed entraining and detraining plume. The Yoshimura cumulus scheme is superior in this respect.

Closure assumption

Magnitudes of the convective updrafts are determined by using a closure assumption (Nordeng, 1994), which is based on convective available potential energy (CAPE). First, the convective updrafts are provisionally calculated by assuming that convective updrafts are uniformly present between the minimum and maximum entrainment rates. The provisional mass flux of Cumulus k is obtained, where Cumulus k is defined as the cumulus cloud that contains the convective updrafts whose cloud top is at the k -th vertical level. Next, the magnitude of the mass flux of Cumulus k is estimated by assuming that Cumulus k reduces $\text{CAPE}(k) \times a(k)$ in a relaxation time τ , where $\text{CAPE}(k)$ is the CAPE of Cumulus k and $a(k)$ is the proportion of the provisional mass flux of Cumulus k at the cloud bottom.

The sum of $a(k)$ is 1.0.

Convective downdraft

A part of the sum of the detrainments from the convective updrafts is equally mixed with the environment air, which is saturated and cooled to the wet-bulb temperature by evaporation of cloud water and precipitation at each vertical level. When the mixture is negatively buoyant, it originates a convective downdraft. A single convective downdraft is calculated. The negatively buoyant mixture becomes the organized entrainment to the convective downdraft. The turbulent entrainment/detrainment rate is $2.0 \times 10^{-4} \text{ m}^{-1}$. The mass flux of the convective downdraft is limited to not more than 0.3 times the sum of the mass fluxes of the convective updrafts. When the convective downdraft becomes positively buoyant at some level, the entire downdraft mass flux is detrained at that level as organized detrainment. If the downdraft does not become positively buoyant, organized detrainment from the downdraft occurs at the sub-cloud layer.

Vertical transport

In the Yoshimura cumulus scheme, a conservative and monotonic semi-Lagrangian scheme is used for vertical transport by convection. The PRM is used for vertical interpolation of prognostic variables in the environment. This is the same method as that used for vertical flux calculation in the dynamics process described in Section 3.1.2. This semi-Lagrangian scheme relaxes the time-step limitation imposed by the CFL condition and enables positive-definite natural material transport.

Horizontal momentum transport

The vertical transport of horizontal momentum by convection is calculated. It is overestimated unless the effect of the sub-grid-scale horizontal pressure gradient force, which acts to adjust the direction of the horizontal wind in convection toward that of the wind in the environment, is introduced. A scheme based on that of Gregory et al. (1997) is adopted for the pressure gradient force. In this scheme, the pressure gradient force is set proportional to the vertical wind shear in the environment.

3.2.3. Kain-Fritsch scheme

The Kain-Fritsch (KF) scheme was developed for application to a meso-scale convection system (Kain and Fritsch, 1990, 1993; Kain, 2004). It assumes a one-dimensional cloud model in which cumulus updraft, entrainment of the surrounding cold, dry air, and detrainment from the updraft, are estimated at each vertical level. Entrainment and detrainment are considered not only at the cloud top and base but also at the sides of the cloud. A trigger function based on CAPE is used to generate convection. Convection removes the vertical instability of the grid scale while consuming CAPE. This scheme has been applied in JMA's operational regional model (Saito et al., 2001, 2006, 2007).

Cumulus updraft

One characteristic feature of a KF scheme is the method for determining entrainment and detrainment of the parameterized cumulus convection, in which entrainment and detrainment are considered not only at the cloud base and cloud top but also at each vertical level between them. It is assumed that there always exist many minute parts caused by mixing of the cloud updraft air with the surrounding air in various proportions, and that minute parts that acquire negative buoyancy drop out of the updraft (detrainment) whereas those with positive buoyancy flow into the cloud updraft (entrainment). Therefore, it is necessary to estimate the degree to which the cloud updraft mixes with the surrounding air. This mixing ratio is determined from the vertical atmospheric pressure, the upward mass flux of the cloud base, and the radius of the updraft. Refer to Kain and Fritsch (1990) and Kain (2004) for details. When the mixing ratio is small, the surrounding dry, cold air flow into the updraft (entrainment) is reduced and outflow of the moist, warm updraft air into the surrounding air is decreased, so the cloud top becomes higher. The cloud top is assumed to be at the level at which the temperature of the updraft parcel is equal to that of the surrounding air. In other words, the cloud top can be considered to intrude into the stable stratification (called overshooting).

Closure assumption

The closure assumption of the KF scheme adopts a method for removing the grid-scale CAPE by parameterized cumulus convection and adjusting the mass flux following Bechtold et al. (2001). The removal ratio can be set as a parameter.

Cumulus downdraft

In the KF scheme, the downdraft is caused by cooling by evaporation of the condensation. The downdraft starts at a saturated level that is more than 150 hPa above the lifting condensation level (LCL). Further, entrainment occurs only above the LCL; under the LCL, humidity decreases with height; and detrainment occurs only under the LCL. The downdraft method is simplified compared with that used for determining the entrainment and detrainment of the updraft.

Trigger function

A trigger function is used in the KF scheme to judge whether sub-grid-scale convection is generated. The trigger function is composed three terms: the temperature of the LCL (T_{LCL}), the temperature perturbation that depends on the buoyancy at the LCL (ΔT_{LCL}) (Kain, 2004), and the temperature perturbation that depends on the humidity (ΔT_{RH}) (Undén et al., 2002). When the trigger function ($T_{LCL} + \Delta T_{LCL} + \Delta T_{RH}$) has a value higher than the surrounding temperature, parameterized cumulus convection is generated.

Conversion of condensation to precipitation

In MRI-AGCM3, two different schemes can be used to generate precipitation with the KF scheme, one by Ogura and Cho (1973) and the other by Kessler (1969). Both schemes estimate the proportion of detrained condensed water from the updraft that falls as precipitation. We adopt the latter method in MRI-AGCM3 when the KF scheme is used for cumulus parameterization.

3.3. Radiation

The radiation processes in MRI-AGCM3 are briefly described here. For the most part, the radiation scheme is the same as that of JMA's operational global atmospheric model (see details in Numerical Prediction Division/JMA, 2007), but there are some differences, for example, in the interaction with aerosols. Because of relatively large computational costs, radiation processes are often calculated at coarser spatial and temporal scales than otherwise used in a model. In the standard ESM configuration, the full radiation computations are calculated for every two grids in the zonal direction, and for every hour and every 3 hours in the shortwave and longwave regions, respectively.

3.3.1. Radiative transfer model

In MRI-AGCM3 radiation scheme, infrared (i.e., longwave, hereafter LW) radiation of up to 3000 cm^{-1} and solar (shortwave, hereafter SW) radiation are treated separately. The LW region of the spectrum is divided into 9 bands (see Figure 5), and the SW region into 22 bands (see Figure 6). The radiative flux is calculated in each band. The model column is split into plane-parallel, homogeneous layers and vertical radiative transfer is solved numerically. In the LW scheme, the absorption approximation method is adopted and band-integrated upward and downward radiative fluxes are calculated by using the band-emissivity method with a diffusivity factor. In the SW scheme, a two-stream approximation (δ -eddington approximation; Joseph et al., 1976) method is used to solve direct and diffuse flux at each layer boundary. Downward (upward) diffuse fluxes in a column are calculated in descending (ascending) order, from the top to the bottom (the bottom to the top) level (as in APPENDIX A in Briegleb, 1992).

Band Number	1	2	3a	3b	3c	4	5	6	7	8	9	
(wave # / cm)	25	340	540	620	720	800	980	1100	1215	1380	1900	3000
H2O (Line)	T	T	K	K	K	K	K	K	K	T	K	
H2O (Continuum)	C	C	C	C	C	C	C	C	C	C	C	
CO2			T			K	K					
O3						(T)	T	(T)				
CH4								K	K			
N2O			K					K	K			
CFC-11						K	K					
CFC-12						K		K				
HCFC-22						K		K				

Figure 5 Spectral bands and absorber gases for LW. Letter T and K mean line absorptions calculated by table lookup method and k-distribution method, respectively. Letter C means use of parameterization for water vapor continuum absorption.

band (numbers)	near-infrared (#1 – 7)	visible (#8 – 12)	ultra-violet (#13 – 22)					
(wave length μm)	∞	1.61	0.870	0.685	0.599	0.364	0.231	0.174
H2O (line)	ESF (7-terms)							
CO2	F&R							
O3		Continuum						
O2		F&R						F&R

Figure 6 Spectral bands and absorber gases for SW. ESF means use of exponential sum fitting technique and F&R means employment of parameterization based on Freidenreich and Ramaswamy (1999).

3.3.2. Atmospheric radiation

In the LW and SW schemes, major absorptions due to water vapor (line and continuum absorption), carbon dioxide (e.g., in the 15 μm band and near-infrared region), and ozone (in the 9.6 μm band and the visible and ultraviolet regions) are considered. In addition, absorptions due to

methane (CH₄), dinitrogen monoxide (N₂O), and CFCs are taken into account in the LW scheme for their greenhouse effect. Absorption by oxygen and Rayleigh scattering by molecules of atmospheric gas are also calculated in the SW scheme.

In the LW scheme, absorption due to atmospheric gas is evaluated by the Planck weighted transmission function in each spectral band. Two types of parameterization obtained from an offline line-by-line (LBL) calculation based on a database of absorption lines are used in order to calculate line absorptions. If the effect of Doppler line broadening cannot be ignored in the stratosphere, a transmittance table made by LBL pre-computations for some pressures, temperatures, and absorber concentrations is referred (Chou and Kouvaris, 1991). This table was calculated by using the HITRAN 2000 (update 1; Rothman et al., 2003) line database and the LBLRTM (Clough et al., 1992) calculation package. For the other absorptions in which the Lorentz type of line broadening is just dominant, the transmittance is rapidly calculated by the k-distribution method (Arking and Grossman, 1972) with the absorber amount scaled by atmospheric pressure and temperature. For the continuum absorption of water vapor, self- and foreign-broadened absorption are considered after the method of Zhong and Haigh (1995) but updated with absorber coefficients from MT-CKD version 1.0, a refined version of the CKD continuum model (Clough et al., 1989).

The SW scheme calculates the optical depth of each absorption due to atmospheric gases. Absorption due to water vapor is calculated by the 7-band k-distribution method (or the exponential sum fitting technique; Lacis and Hansen, 1974) after Briegleb (1992). For ozone, carbon dioxide, and oxygen, the parameterization of Freidenreich and Ramaswamy (1999) is used to compute optical depth of the absorption. Their work is also referred in determining the Rayleigh scattering coefficients.

3.3.3. Cloud radiation and aerosol effect

To represent the direct effects of aerosols, optical parameters are configured for 5 aerosol species corresponding to those in the aerosol model (Section 6): sulfate, black carbon (soot), organic carbon, mineral dust, and sea-salt. The extinction and absorption coefficients and asymmetry factors of these species are computed under the assumption of Mie scattering by spherical particles by using the complex refraction index data of OPAC software (Hess et al., 1998). In the case of hygroscopic species, their dependence on ambient relative humidity is also considered (Chin et al., 2002).

The effect of aerosols on the optical properties of clouds (i.e., the first indirect effect) is considered in the configuration of the effective radius of cloud particles. The effective radius of a liquid water cloud particle is computed as a function of cloud droplet number density, based on Liu et al. (2006) and Peng and Lohmann (2003). If a two-moment scheme is selected for the cloud scheme (Section 3.4), then the aerosol indirect effect on ice cloud particles is also considered (Lohmann, 2002). Otherwise, the effective radius of ice cloud particles is parameterized as a function of temperature and ice-water content (Wyser, 1998).

In terms of the optical properties of cloud particle, LW emissivity is parameterized depending on cloud water content (Kiehl and Zender, 1995), and the corresponding absorption coefficient is parameterized as a function of effective radius (Hu and Stamnes, 1993, for liquid water clouds, and Ebert and Curry, 1992, for ice clouds). Optical depth, single scattering albedo, and the asymmetry factor in SW are similarly parameterized by cloud water content and effective radius (Slingo, 1989, for water clouds and Ebert and Curry, 1992, for ice clouds).

Though a cloud is approximated as a black body in the LW scheme, the calculation method of Räisänen (1998) is adopted, in which both cloudiness and cloud emissivity in a cloudy layer are properly considered and the calculation results have no dependency on the vertical resolution of the model layers. The vertical overlap of clouds greatly influences estimations of radiative fluxes in a cloudy column. In the LW scheme, maximum-random overlap (Geleyn and Hollingsworth, 1979) is assumed. In the SW scheme, total cloudiness in a column is first computed according to the maximum-random overlap assumption, and then random overlap is assumed to solve radiative fluxes in a cloudy sub-column.

3.4. Cloud model

Cloud water and fraction are the variables of the cloud scheme used to represent large-scale condensation in the AGCM. The Smith cloud scheme (Smith, 1990), which is based on probability distributions (Sommeria and Deardorff, 1977), is employed in JMA's operational weather prediction model. The Tiedtke cloud scheme (Tiedtke, 1993; ECMWF, 2004; Jakob, 2000), which treats cloud water and fraction as prognostic variables, is also incorporated in MRI-AGCM3.

In MRI-ESM1, the chemistry climate model (MRI-CCM2) and the aerosol model (MASINGAR mk-

2) can be coupled via the Scup coupler with MRI-AGCM3. This means that MRI-AGCM3 is able to recognize the spatial-temporal distribution of aerosol species. For projection of future global climate change, direct and indirect effects of aerosols are the primary factors leading to uncertainties in the assessment of radiative forcing, and they are therefore among the most important physical processes coupling the aerosol model with the AGCM. To represent the indirect effects of aerosols in detail, cloud droplet and ice crystal concentrations are important information. Furthermore, their efficient simulation is desirable for long-term predictions of the ESM. To increase the accuracy of the indirect aerosol effects in the ESM, it is necessary for the cloud scheme, which is represented by the cloud water mixing ratio and fraction, to be expanded to take into consideration at least the cloud liquid water mixing ratio, the cloud ice mixing ratio, cloud droplet and ice crystal concentrations, and cloud fraction.

Therefore, a new two-moment bulk cloud scheme (called the MRI-TMBC scheme) was developed by expanding the original equation system (i.e., prediction of the cloud water mixing ratio by the Tiedtke cloud scheme) to include the necessary variables. The new scheme predicts the cloud liquid water mixing ratio, the cloud ice mixing ratio, and cloud droplet and ice crystal concentrations (shown schematically in Fig. 7). The Smith, Tiedtke, and MRI-TMBC schemes can be arbitrarily selected in MRI-ESM1. The MRI-TMBC scheme is described by differential equations as follows.

$$\frac{\partial q_c}{\partial t} = adv(q_c) + S_{conv}^{liq} + S_{new}^{liq} + S_{old}^{liq} - E^{liq} - G^{rain} - (N_{imm} + N_{cont} + N_{homo}) + M_{melt} \quad (3.30)$$

$$\frac{\partial q_i}{\partial t} = adv(q_i) + S_{conv}^{ice} + S_{new}^{ice} + S_{old}^{ice} - E^{ice} - G^{snow} + (N_{imm} + N_{cont} + N_{homo}) - M_{melt} \quad (3.31)$$

$$\frac{\partial q_v}{\partial t} = adv(q_v) - (S_{conv}^{liq} + S_{new}^{liq} + S_{old}^{liq} + S_{conv}^{ice} + S_{new}^{ice} + S_{old}^{ice}) + E^{liq} + E^{ice} + E^{rain} + E^{snow} \quad (3.32)$$

$$\frac{\partial N_c}{\partial t} = adv(N_c) + NS_{conv}^{liq} + NS_{new}^{liq} - NE^{liq} - NG^{rain} - (NN_{imm} + NN_{cont} + NN_{homo}) + NM_{melt} \quad (3.33)$$

$$\frac{\partial N_i}{\partial t} = adv(N_i) + NS_{conv}^{ice} + NS_{new}^{ice} - NE^{ice} - NG^{snow} - (NN_{imm} + NN_{cont} + NN_{homo}) - NM_{melt} \quad (3.34)$$

where q_c , q_i , and q_v respectively indicate the cloud liquid water mixing ratio, the cloud ice mixing ratio, and the water vapor mixing ratio (kg kg^{-1}); N_c and N_i are respectively the cloud droplet concentration and the ice crystal concentration (m^{-3}); and S , E , G , N , M , and adv respectively represent the source, evaporation, precipitation, the interaction between cloud water and cloud ice, melting, and advection

terms. In addition, the superscripts *liq*, *ice*, *rain*, and *snow* respectively represent the cloud liquid water, cloud ice, rainfall, and snowfall components, and the subscripts *conv*, *new*, and *old* respectively represent the convective, stratiform formation, and stratiform growth components. Finally, the subscripts *imm*, *cont*, and *homo* represent immersion freezing, contact freezing, and homogeneous freezing, respectively. The differential equations for cloud droplet concentration and ice crystal concentration are formally described to be consistent with those for the cloud liquid water mixing ratio

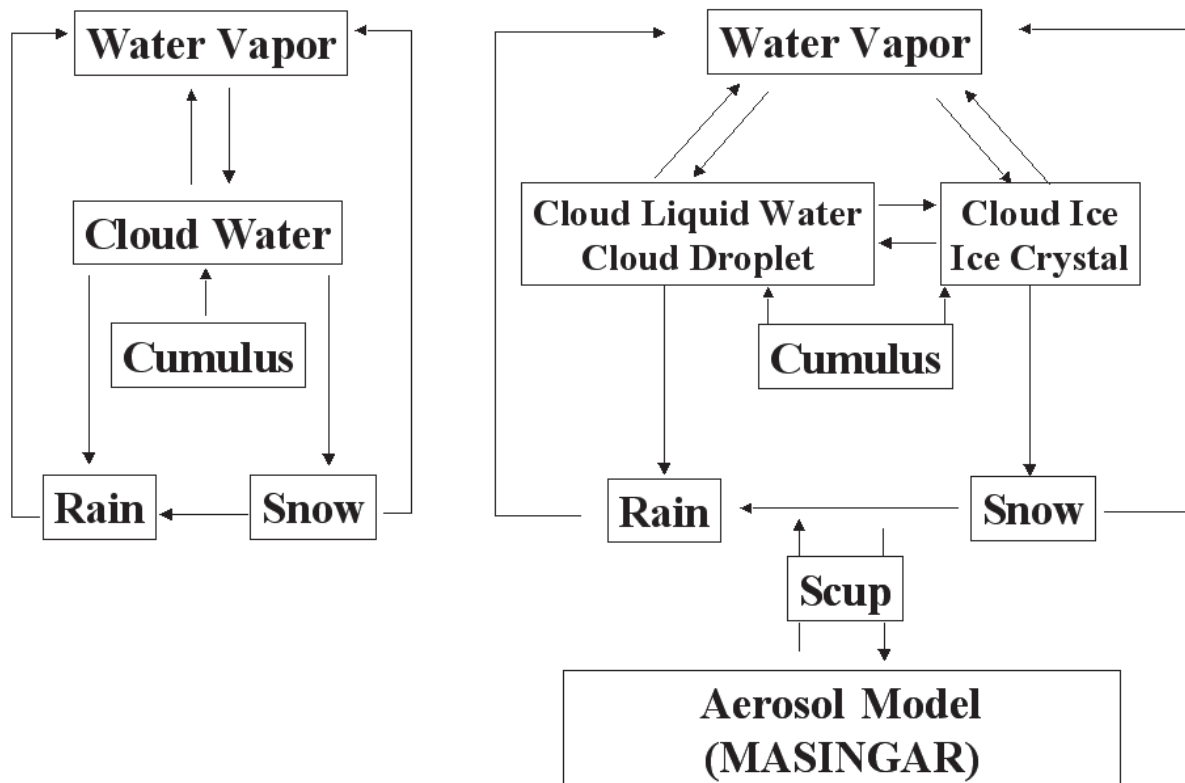


Figure 7 Framework of cloud scheme in the MRI-ESM1. Left figure indicates framework of the Smith cloud scheme and the Tiedtke cloud scheme. Right figure indicates a newly modeled double moment bulk cloud scheme.

and cloud ice mixing ratio.

The aerosol model is directly coupled to the MRI-TMBC scheme by activation of aerosol species into cloud droplets and ice crystals. The aerosol species employed in both MASINGAR mk-2 and the cloud scheme are SO_x + dimethyl sulfide (DMS), black carbon (BC), organic carbon (OC), sea salt (2 bins), and dust (6 bins). The activation of some aerosols into cloud droplets is based on the parameterizations of Abdul-Razzak and Ghan (2000, 2002) and Takemura et al. (2005). The activation of some aerosols into ice crystals is based on the parameterizations of Bigg (1953, immersion freezing), Lohman and Diehl (2006, contact freezing), and Kärcher et al. (2006, cirrus clouds). Cloud droplet and

through their effective radii.

The deposition and depositional growth terms are based on Murakami (1990) and Rutledge and Hobbs (1983), respectively, and the condensation and condensation growth terms on Tiedtke (1993). Melting occurs when the atmospheric temperature is above 273.15 K, and homogeneous freezing occurs at temperatures below 235.0 K. A semi-Lagrangian scheme (Section 3.1) is used for the advection process. The precipitation process is basically unchanged, except that the parameterization of Rotstaysn (2000) is adopted for the rainfall term (Fig. 7). The Bergeron-Findeisen process is also incorporated into the MRI-TMBC scheme. This process occurs when the cloud ice mixing ratio is greater than 0.5 mg kg⁻¹ (Lohman et al., 2007). Furthermore, a saturation adjustment proposed by Tao (1989) is introduced

3.5. Planetary boundary layer

The role of the boundary layer scheme in AGCM is to parameterize the vertical transport of momentum, heat, and moisture by turbulence in the atmosphere. The boundary layer scheme in JMA's operational model is the turbulence model advocated by Mellor and Yamada (1974, 1982) (the MY scheme), which is a second-order closure model based on the Reynolds averaging method. However, in the new MRI-AGCM3, the evaluation of the closure constants and the mixing length are optionally modified, following Nakanishi (2001) and Nakanishi and Niino (2004, 2006, 2009).

Additionally, a non-local scheme based on the parameterizations of Troen and Mahrt (1986) and Holtslag and Boville (1993), which can express non-local vertical mixing when conditions near the surface layer are unstable, is an optional PBL scheme that can be selected in MRI-AGCM3.

3.5.1. Mellor-Yamada scheme

The Mellor-Yamada scheme expresses the third moment quantity by the second moment by using the Reynolds averaging method. In all, there are 15 prognostic variables of the second moment (the Level 4 model), but in weather and climate models the scheme can be simplified according to the contribution of anisotropy because of the computational costs (Levels 3, 2.5, and 2; see Mellor and Yamada, 1974, 1982, for details). In Level 2, used in MRI-AGCM3, all prognostic equations become diagnostic ones, and all variables of the second moment are obtained by solving those equations. In addition, in the atmospheric boundary layer, because the horizontal variation of physical values is very

small compared with the vertical variation, horizontal differentiation is disregarded. This approximation is called the boundary layer approximation. In general, there exist two or more closure constants in the closure model. These constants should be determined empirically. Mellor and Yamada (1982) determined these closure constants from observations and wind tunnel experiments under neutral conditions. Moreover, the mixing length l is given beforehand:

$$\frac{1}{l} = \frac{1}{L_S} + \frac{1}{L_T} \quad (3.35)$$

$$L_S = \kappa z \quad (3.35a)$$

$$L_T = \alpha \frac{\int_0^\infty qz dz}{\int_0^\infty q dz} \quad (3.35b)$$

where L_S is the length determined according to the vertical log-profile of the physical value near the surface, L_T is the length reflecting the vertical profile of turbulent energy (q), α is an empirical constant, and κ is the Karman constant.

3.5.2. Mellor-Yamada-Nakanishi-Niino scheme

Nakanishi (2001) and Nakanishi and Niino (2004, 2006, 2009) proposed an improved version of the MY scheme (called the MYNN scheme) for determining closure constants, mixing length, and the stability of time integration. We introduced the first two improvements into MRI-AGCM3 as follows. First, on the basis of data obtained by large eddy simulation (LES), the MYNN scheme re-evaluates the closure constants and introduces terms for the effect of buoyancy and wind shear, which are neglected in MY model.

$$(A_1, A_2, B_1, B_2, C_1) = (0.92, 0.74, 16.6, 10.1, 0.08) \rightarrow (1.18, 0.665, 24.0, 15.0, 0.137) \quad (3.36)$$

$$(C_2, C_3, C_4, C_5) = (0, 0, 0, 0) \rightarrow (0.65, 0.294, 0, 0.2) \quad (3.37)$$

Here, C_2 and C_3 reflect the effect of buoyancy, and C_5 that of wind shear. Refer to the original paper for details.

Second, a new diagnostic equation for the mixing length l , which was considered an uncertain expression, is proposed here, based on LES:

$$\frac{1}{l} = \frac{1}{L_S} + \frac{1}{L_T} + \frac{1}{L_B} \quad (3.38)$$

$$L_S = \begin{cases} \kappa z / 3.7 & (\zeta \geq 1) \\ \kappa z / (1 + 2.7\zeta) & (0 \leq \zeta < 1) \\ \kappa z (1 - \alpha_4 \zeta)^{0.2} & (\zeta < 0) \end{cases} \quad (3.38a)$$

$$L_T = \alpha_1 \frac{\int_0^\infty qz dz}{\int_0^\infty q dz} \quad (3.38b)$$

$$L_B = \begin{cases} \alpha_2 q / N_1 & (\partial\theta/\partial z > 0, \zeta \geq 0) \\ [\alpha_2 q + \alpha_3 (q_c / L_T N_1)^{1/2}] N_1 & (\partial\theta/\partial z > 0, \zeta < 0) \\ \infty & (\partial\theta/\partial z \geq 0) \end{cases} \quad (3.38c)$$

where α_1 , α_2 , α_3 , and α_4 are empirical constants (= 0.23, 1.0, 5.0, and 100.0, respectively); $\zeta = z/L$; and L is the Monin-Obukhov length. This new equation thus evaluates the stability of the surface layer by using the Monin-Obukhov length and the effect of buoyancy (L_B) (Hara, 2007ab).

3.5.3. Non-local scheme

When conditions near the surface are unstable, especially in the daytime, momentum, heat, and moisture are often very efficiently transported through the entire boundary layer by the large turbulence in the PBL. Such characteristic large turbulence transport is called the non-local effect. We introduced a scheme to express these non-local effects following Troen and Mahrt (1986) and Holtslag and Boville (1993). However, it is well known that although this scheme can express well the development of a convective mixing layer in the daytime, it cannot adequately express the weakening of the mixing layer and the influence of the diurnal cycle on surface temperature and wind. Moreover, in some cases, the cold pool is destroyed when a cold layer is formed in the boundary layer. Therefore, development of this scheme has been postponed for the present.

3.6. Land surface models

Three land-surface models are available in MRI-AGCM3, and a model user can select any one of them. The first one is JMA/SiB (Simple Biosphere model; Sellers et al., 1986, Sato et al., 1989), which is

used mainly for short-range weather forecasting. The second, SiB0109 (Hirai et al., 2007), which was developed for climate research purposes and is used in MRI-CGCM2.3, both water mass and energy are perfectly conserved. The third one, HAL (Hosaka et al., in preparation), is newly developed and will be used for the CMIP5 simulations. In this subsection, HAL is briefly described.

HAL (the name is formed from the first letters of Hydrology, Atmosphere, and Landsurface, and means "spring" in Japanese) is MRI-AGCM3's new land-surface model. The major predicted variables are temperature and moisture content in the vegetation, soil, and snow submodels, and HAL diagnoses surface conditions. HAL also evaluates heat, moisture, and momentum fluxes and albedo, which are used in MRI-AGCM3 simulations as lower atmospheric boundary conditions. HAL can calculate variables related to the terrestrial carbon cycle, and they are used by the terrestrial carbon model (Section 8.1).

HAL consists of three submodels: SiByl, SNOWA, and SOILA, which are coupled to one another by the LCUP land-surface coupler, which also connects HAL to MRI-AGCM3. LCUP supports the mosaic and mixture strategy (Koster and Suarez, 1996), which enables more appropriate fluxes to be estimated over non-uniform surfaces.

SiByl has surface vegetation processes similar to JMA/SiB, on which it is based. SiByl has 2 vegetation layers (canopy and grass) and calculates heat, moisture, and momentum fluxes between the land surface and the atmosphere. The major predicted variables are the temperature of the canopy and the surface skin, and the moisture content of the canopy and the grass. Included moisture processes are precipitation intercepted by and dropped from the canopy and the grass, evaporation or sublimation from and dew or frost on bare soil and vegetation, and transpiration by vegetation. Heat processes implemented comprise shortwave radiation (direct/diffuse, visible/infrared), longwave radiation, sensible heat, latent heat, and ground heat fluxes. A bulk formulation scheme (Louis, 1979) is used for estimating surface flux. Air surface information such as the air temperature at 2 m height is diagnosed.

Some physical processes are improved in HAL from JMA/SiB. The overly simplified snow and soil processes in JMA/SiB are not used in HAL. The ground heat flux is calculated not by the force restore method but by solving heat conduction equations with temperatures of the lower (snow or soil) layers. When the snow water equivalent (SWE) is less than ~20 mm, partial snow is realized. For the estimation of stomatal resistance, in addition to the original JMA/SiB method, a new option for biochemical photosynthesis process is available that is able to output some variables for the terrestrial

carbon model (Section 8.1) and to evaluate the CO₂ flux between the land surface and the atmosphere. In JMA/SiB, many vegetation parameters depend only on 13 vegetation types. In contrast, in HAL, the default values, which depend on the types, are replaced by more appropriate values based on observational data at each grid point.

The snow submodel SNOWA can have more snow layers*¹ than SiB0109. The number of layers depends on the SWE and the snow accumulation history. The top layer is typically 10 mm SWE in thickness, and the thicknesses of the 2nd to 7th layers are 20 mm SWE. The lowest (8th) layer receives discharge from all the layers above it. Each layer also has an upper and lower SWE limit value. If the SWE of a snow layer exceeds the upper limit, the layer is divided into 2, and if it falls below the lower limit, the snow layer is combined with the layer beneath it. Therefore the snow properties are not affected by numerical diffusion so much.

The predicted variables for snow are temperature, SWE, density, and the aerosol contents*² of each layer. To predict the temperature, heat conduction equations are solved where the upper boundary condition is the ground heat flux calculated by the upper submodel (SiByl). When the temperature of each layer is higher than -1 °C, a water phase change occurs. If the mixing ratio of liquid water is more than 10%, the excess liquid water drops into the layer below. If the temperature of the uppermost underlying soil layer is higher than 1 °C, the excess energy is used for melting the snow at the bottom of the layer, and the meltwater infiltrates into the soil. SNOWA also has some snow albedo schemes (options). The default setting uses the aerosol mixing ratio (Aoki et al., 2003), and in another option the albedo is predicted and changes depending on the temperature (Aoki and Tanaka, 2008).

The soil submodel SOILA is composed of 14 soil layers with depths of 2, 3, 5, 10, 10, 20, 30, 30, 40, 100, 100, 150, 200, and 300 cm, for a total depth of 10 m*³. There are 5 layers in the top 30 cm, which allows diurnal temperature changes to be simulated. The temperature of each layer is predicted by solving heat conduction equations, where the upper boundary condition (heat flux) is given by an upper submodel (SiByl or SNOWA). The number of layers in which soil moisture is predicted depends on the vegetation type. For example, in forest grids, soil moisture is present in the uppermost 11 layers (the upper 350 cm), in grass grids in the uppermost 9 layers (150 cm), and in desert grids in the uppermost 6 layers (50 cm). The infiltration flux of liquid water is estimated by solving the Darcy

*1 The maximum number of snow layers and the typical upper and lower limits of SWE in each layer can be arbitrarily set by a user. The values described above are model defaults.

*2 Depending on the snow albedo schemes selected, the aerosol contents can be replaced with other parameters.

*3 The number of soil layers and their depths can be arbitrarily set by a user, with some limitations. The values described above are model defaults.

equation, in which hydraulic conductivity depends on the soil moisture. Drainage (gravitational runoff) occurs from the bottom layer, and surface runoff occurs from the top layer. The phase change of water occurs between $-1\text{ }^{\circ}\text{C}$ and $1\text{ }^{\circ}\text{C}$, and in colder regions the soil is frozen.

3.7. Ocean surface processes

In this section, the modeling of sea-surface and sea-ice surface processes is described. An important function of the ocean surface scheme is the calculation of turbulent heat, moisture, and momentum fluxes. The atmospheric variables, the (skin) surface temperature, and the fluxes are determined at the same time by the implicit method from the vertical diffusivity, which is calculated in the PBL scheme. The fluxes are calculated by the generally used bulk method. The bulk coefficients are from Louis (1979) and Louis et al. (1982), except those for turbulent fluxes in the unstable state, which are from Miller et al. (1992).

3.7.1. Sea surface

Sea-surface temperature (SST) is fixed during each time step in the calculation of the fluxes over the sea surface. When the conventional sea-surface scheme is used, SST is read from a boundary conditions file (bulk SST) in a typical AGCM experiment. It is set to the same temperature as that in the first layer (typically a few meters thick) of the OGCM in a typical CGCM simulation. However, when the simple skin SST scheme described here is used, the skin temperature provided by the scheme is used in the AGCM as the lower boundary over the sea surface .

Simple skin SST scheme

This scheme is designed to represent short-term temperature variation (e.g., diurnal variation) at the air–sea interface caused by short-term variations in wind and solar radiation (Fig. 8). The interface temperature is estimated from the heat fluxes to the atmosphere and from the bottom of the layer. Since the sub-skin layer is empirically known to be apt to mix with the underlying layer under windy conditions, the coefficient for the heat flux from the bottom of the layer depends on wind speed, being larger when the wind is stronger (Kawai and Wada, 2007).

This scheme has one sub-skin layer with a linear temperature profile within the layer, and its thickness (h_s) is 1 m. The temperature at $h_s/2$ depth is the sub-skin SST (T_s), which is the prognostic

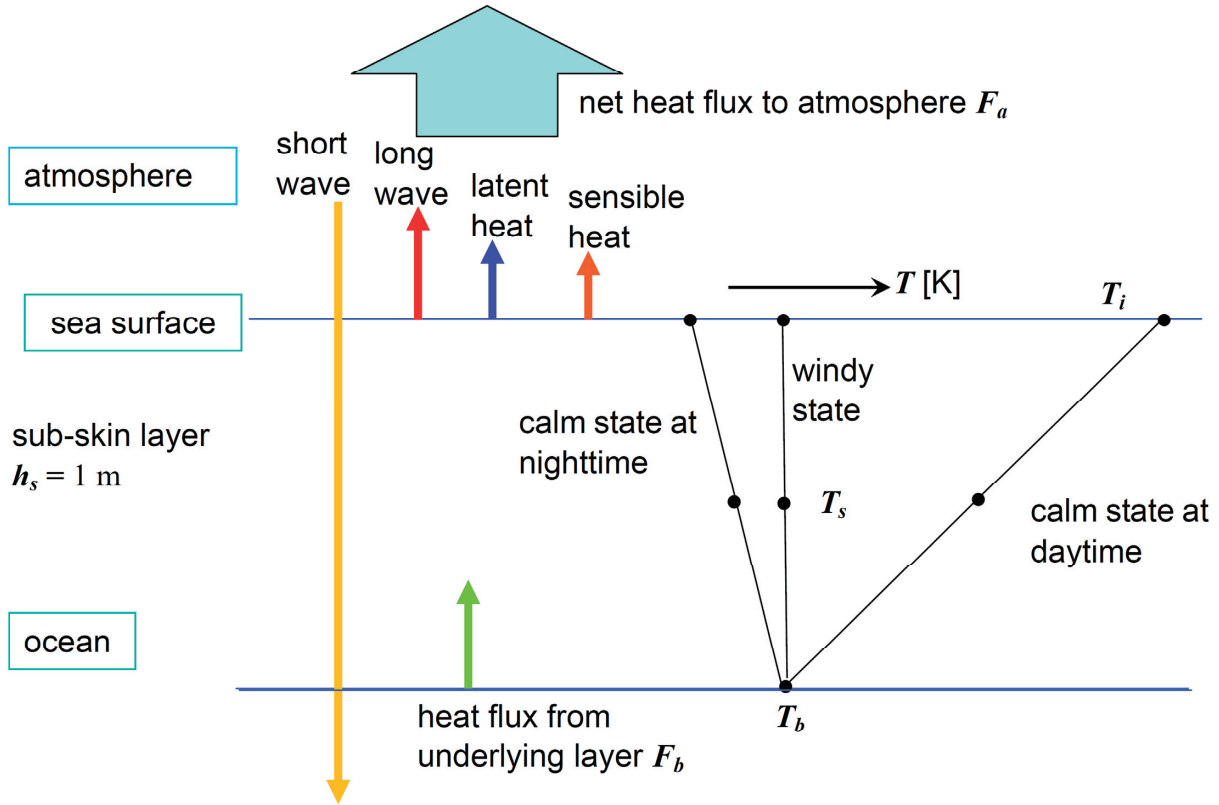


Figure 8 Conceptual illustration of the simple skin SST scheme

variable in the force restore method. The temperature at the bottom of the layer (T_b) is set as ‘bulk SST’ in this scheme. In AGCM, the bulk SST, T_b , is read from the boundary condition file, and in CGCM it is the first-layer temperature of the OGCM. The temperature at the top of the layer (T_i) is the interface SST, and is used for calculation of the fluxes at the next step. For simplicity, it is assumed that the temperature profile in the layer is linear:

$$T_i = T_b + 2(T_s - T_b) = 2T_s - T_b. \quad (3.39)$$

The tendency of the sub-skin SST is estimated by the following equation.

$$\rho C_p h_s dT_s / dt = F_b - F_a, \quad (3.40)$$

where ρ is the density of seawater (1030 kg m^{-3}), C_p is the specific heat of seawater ($3930 \text{ J K}^{-1} \text{ kg}^{-1}$), F_b is heat flux from bottom of the layer, and F_a is net heat flux to the atmosphere. Fluxes already calculated in this step are used for F_a , which includes latent heat, sensible heat, longwave radiation, and shortwave radiation flux. The shortwave radiation fluxes are calculated for visible and near-infrared wavelengths, taking penetration into account, with the following equation:

$$R_{sw} = R_{swvis}(1 - \exp(-h_s/h_{pvis})) + R_{swnir}(1 - \exp(-h_s/h_{pnir})), \quad (3.41)$$

where R_{sw} is solar radiation absorption in the sub-skin layer, R_{swvis} is net visible radiation at the surface (downward is positive), h_{pvis} is the e -folding depth for visible radiation (23 m), R_{swnir} is net near-infrared

radiation at the surface (downward is positive), and h_{pmir} is the e -folding depth for near-infrared radiation (0.35 m). F_b is estimated by the bulk equation,

$$F_b = \rho C_p h_s (T_b - T_s) / \tau. \quad (3.42)$$

(Notice that this equation uses T_s that would be changed by F_a for numerical stability, thus the method is an analogy of implicit method.) Here, τ is the relaxation time of T_s to T_b (time constant). Because the sub-skin layer is well mixed with the underlying layer under windy conditions, τ depends on the wind speed over the ocean. It is assumed that τ decreases exponentially as the wind speed increases, as in the following equation (see the equations in Gentemann et al., 2003, and Fig. 3a in Castro et al., 2003):

$$\tau = t_c \exp(-U/U_e), \quad (3.43)$$

where t_c is the time constant when the wind speed is zero, U is the wind speed, and U_e is the wind speed when τ becomes $1/e$. Because the typical target timescale of the temperature variation is shorter than a day (e.g., diurnal cycle), t_c is set to 24 hours ($T_s > T_b$). However, it is empirically known that the sub-skin layer tends to mix with the underlying layer because of unstable stratification when the sub-skin layer temperature is lower than the temperature of the underlying layer ($T_s < T_b$); thus, t_c is set to a value shorter than 24 hours when $T_s > T_b$. Since the observed skin temperature declines at night (e.g., Castro et al., 2003) by one-fourth to one-sixth, t_c is set to one-fifth of the daytime temperature. It is assumed that the relaxation time is 1 hour when $T_s > T_b$ and 12 minutes when $T_s < T_b$ at a wind speed of 10 m/s, so U_e is set to 3.15 ($= 10/\log 24$). This assumption (i.e., $1/U_e = 0.32$) is practical because the wind effect corresponding to $1/U_e$ has a value of 0.53 or 0.29 (Gentemann et al., 2003) or 0.27 (Castro et al., 2003).

3.7.2. Sea-ice surface

The sea-ice surface temperature is a prognostic variable even in a general AGCM, and its variation is calculated at the same time as the sensible and latent heat fluxes by the implicit method. The snow surface processes are calculated in the same way as those for snow on land when snow (either partial or full coverage) is on the sea ice. The roughness length is set to a constant (0.001 m). The other parameters are fundamentally the same as for the sea surface. The temperature at the bottom of the sea ice and the sea-ice thickness are set to constants during the calculation of fluxes, and are used as lower boundary conditions in the AGCM. They are input from the OGCM in the CGCM. The snow amount

(water equivalent) on sea ice is a prognostic variable in the AGCM, and input from the OGCM in the CGCM, like the temperature at the bottom of the sea ice and sea-ice thickness. The amount of snowfall and sublimation are output to the OGCM from the AGCM. When there are multiple categories for sea-ice thickness in a single grid, these values are calculated for each category.

Albedo on sea ice

The formulation of sea-ice surface albedo is fundamentally similar to that in the Los Alamos sea ice model CICE (Hunke and Lipscomb, 2001). Both the ice albedo and the snow albedo are estimated. The sea-ice surface albedo is determined as an average weighted by the snow cover percentage, which depends on the snow amount. However, the parameterization of Aoki and Tanaka (2008), who account for the albedo decline due to pollution by aerosol deposition, is applied to the estimation of snow albedo. Moreover, the effect of penetration of solar radiation on albedo is taken into account for both ice and snow for visible and near-infrared wavelengths, respectively.

3.8. River and lake model

3.8.1. GRiveT

GRiveT (Global River model using TRIP) is the river-flow component (Fig. 9) used in MRI-ESM1. The river channel is the Total River Integrated Pathway (TRIP, Oki and Sud, 1998), either the $1^\circ \times 1^\circ$ or the $0.5^\circ \times 0.5^\circ$ version. The land-surface model in MRI-AGCM3 calculates river runoff in all land grids, and all river runoffs are transported by GRiveT to the river mouths via the river channels. GRiveT also has a lake in each TRIP grid, which is connected to the lake-surface component in MRI-AGCM3.

The predicted variables in GRiveT are the water masses (W) of river (r) and lake (l) and their inertial energies (E). The equations governing the water masses are

$$dWr / dt = \Sigma Frr_{in} + \Sigma Flr_{in} - Frr_{out} - Frl + R_{Oland} \quad (3.44)$$

$$dWl / dt = Frl - Flr_{out} + P_{lake} - E_{lake} \quad (3.45)$$

$$Frr = a Wr (c\Delta t / L) \quad (3.46)$$

$$Frl = (1-a) Wr (c\Delta t / L) \quad (3.47)$$

$$Flr = Frl + (Wl - Wl_{std})/\tau \quad (3.48)$$

Here, Frl , Flr , and Frr are the water fluxes; R_{Oland} is the river runoff estimated by the land-surface component (area weighted average); P_{lake} and E_{lake} are precipitation and evaporation estimated by the

lake-surface component (area weighted average); c is the river flow velocity (global constant, 0.4 m s^{-1}); Δt is the time step; L is the distance between the center of the grid and that of the downstream grid; a is a global constant = 0.5; W_{std} is the standard water mass of each lake (the depth is a global constant; 10 m); and τ is the e -folding timescale of the lake water mass (global constant, $O(10 \text{ days})$).

The inertial energies (E) of river and lake are defined as $E = c_{water} W (T - T_{frez})$, where c_{water} is the specific heat constant of liquid water, T is the temperature, and T_{frez} is 273.15 K (freezing point). EI is also affected by the downward heat flux at the lake surface.

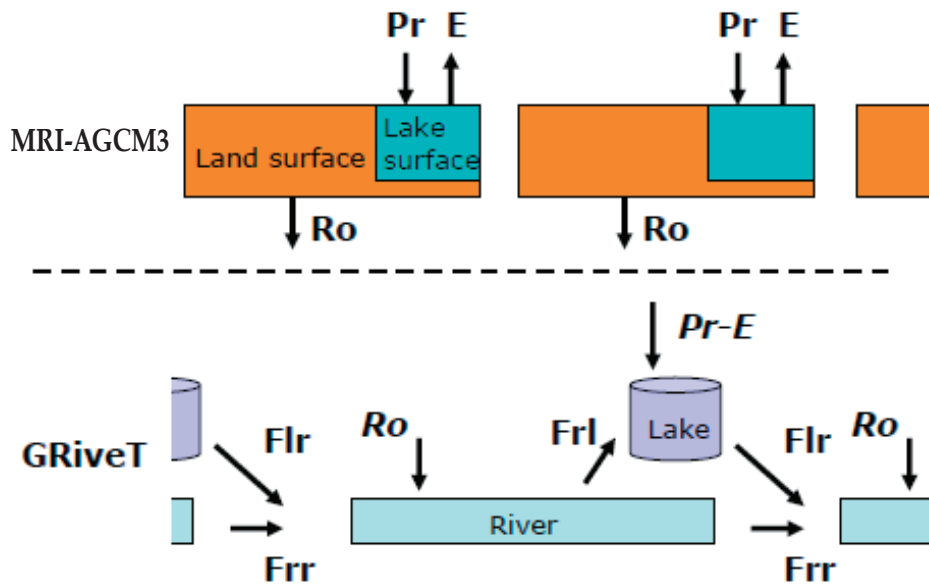


Figure 9 Schematics diagram of the river and lake model GRiveT

4. Ocean-ice model (MRI.COM3)

The ocean-ice component of ESM is the MRI Community Ocean Model Version 3 (MRI.COM3). Users are referred to its reference manual (Tsujino et al., 2010) for details. Its basic characteristics are listed in Table 2. This chapter is organized as follows. Section 4.1 explains the ocean model. Section 4.2 explains the sea ice model. Section 4.3 explains how MRI.COM3 is coupled with the atmospheric component MRI-AGCM3.

Table 2: Features of MRI.COM3

Coordinates Grid arrangement (Horizontal)	General orthogonal curvilinear coordinates Arakawa B grid (coastline is on the tracer point)
Coordinates Grid arrangement (Vertical)	σ -level over z-level Partial cell at the lowermost level Bottom boundary layer (option)
Free-surface	Explicit (Killworth et al., 1991)
Momentum advection	Quasi-estrophy conservation scheme (Ishizaki and Motoi, 1999)
Sea Ice model (Thermodynamics) (Thickness category) (Dynamics)	Mellor and Kantha (1989) Hunke and Lipscomb (2006) Hunke and Dukowicz (2002)

4.1. Ocean model

4.1.1. General features

MRI.COM3 is a free-surface, depth-coordinate ocean-ice model that solves primitive equations using Boussinesq and hydrostatic approximation. A split-explicit algorithm is used for the barotropic and baroclinic parts of the equations (Killworth et al., 1991). Several upper levels follow the undulation of sea surface, as in σ -coordinate models (Hasumi, 2006). MRI.COM3 can be used to simulate ocean and sea ice with various specific configurations. Here, we describe the MRI.COM3 specification used as the ESM component. Section 4.1.2 explains resolution and topography. Section 4.1.3 explains transport algorithms for momentum and tracers. Section 4.1.4 explains sub-grid-scale mixing. Section 4.1.5 explains the solution procedure. Basic settings are summarized in Table 3.

Table 3: Settings of MRI.COM3 when used as a component of the ESM

Grid	Tripolar grid (singularities of the bipolar grid are at (64°N, 80°E) and (64°N, 100°W))
Resolution	1° (zonal), 0.5° (meridional), 50 levels + BBL (Nakano and Suginohara, 2002) (Total: 364 × 368 × 51)
Thickness of vertical grid	4, 5, 6.5, 7.5, 9, 11.5, 14, 16, 17.5, 18, 18.5, 20, 20.5, 21, 22, 23, 24, 27, 30, 30, 35, 40, 40, 50, 60, 65, 70, 75, 80, 90, 100, 100, 125, 150, 150, 150, 175, 225, 250, 250, 250, 275, 300, 300, 300, 300, 300, 450, 600, 600 (m) Upper 5 layers: variable BBL: 50 m
Tracer advection	Second-Order Moment (Prather, 1986)
Epineutral mixing (coefficients)	Isopycnal diffusion ($5 \times 10^2 \text{ m}^2\text{s}^{-1}$) + GM ¹ thickness diffusion ($2.5 \times 10^{-3} \times \text{grid-size m}^2 \text{ s}^{-1}$)
Horizontal viscosity	Smagorinsky-like viscosity with flow-dependent anisotropy
Mixed layer model	Noh and Kim (1999), Noh et al. (2005)
Background viscosity and diffusion	Tsujino et al. (2000) + Tidally driven mixing near the Kuril Islands (St. Laurent et al., 2002)

4.1.2. Resolution and topography

Horizontal resolutions are 1° of longitude and 0.5° of latitude. The model uses the Arakawa B-grid arrangement, and the coastlines are created by connecting tracer points instead of velocity points. This feature is useful for coarse-resolution global models because a narrow passage can be represented by a single velocity cell. A generalized orthogonal coordinate system is used in the Arctic region (latitudes higher than 64°N, tripolar grid; see Fig. 10).

The model ocean consists of 50 vertical levels plus a bottom boundary layer (BBL; Nakano and Suginohara, 2002). The thickness of the surface layer is 4 m, and the upper layers above 1000 m are resolved by 30 layers. The vertical levels shallower than 32 m follow the surface topography, as in σ -coordinate models (Hasumi, 2006), enabling us to obtain a fine vertical resolution near the surface without causing the uppermost layer to vanish in the southern ocean, where the sea surface height is significantly lower than in other regions. Vertically partial cells in the lowermost level enable us to

¹ Gent and McWilliams (1990)

represent realistic (smooth) bottom topography despite the rather coarse resolution of the lower layers. BBLs with a thickness of 50 m are added in dense-water formation regions.

Model topography is constructed from the Global Gridded 2-minute Database (ETOPO2v2; National Geophysical Data Center). The depth of a model grid is obtained by taking an area-weighted average of the corresponding grids in the ETOPO2v2 data. The topography of the model is modified to represent important oceanic current systems, including around complex archipelagos such as the Philippine Islands.

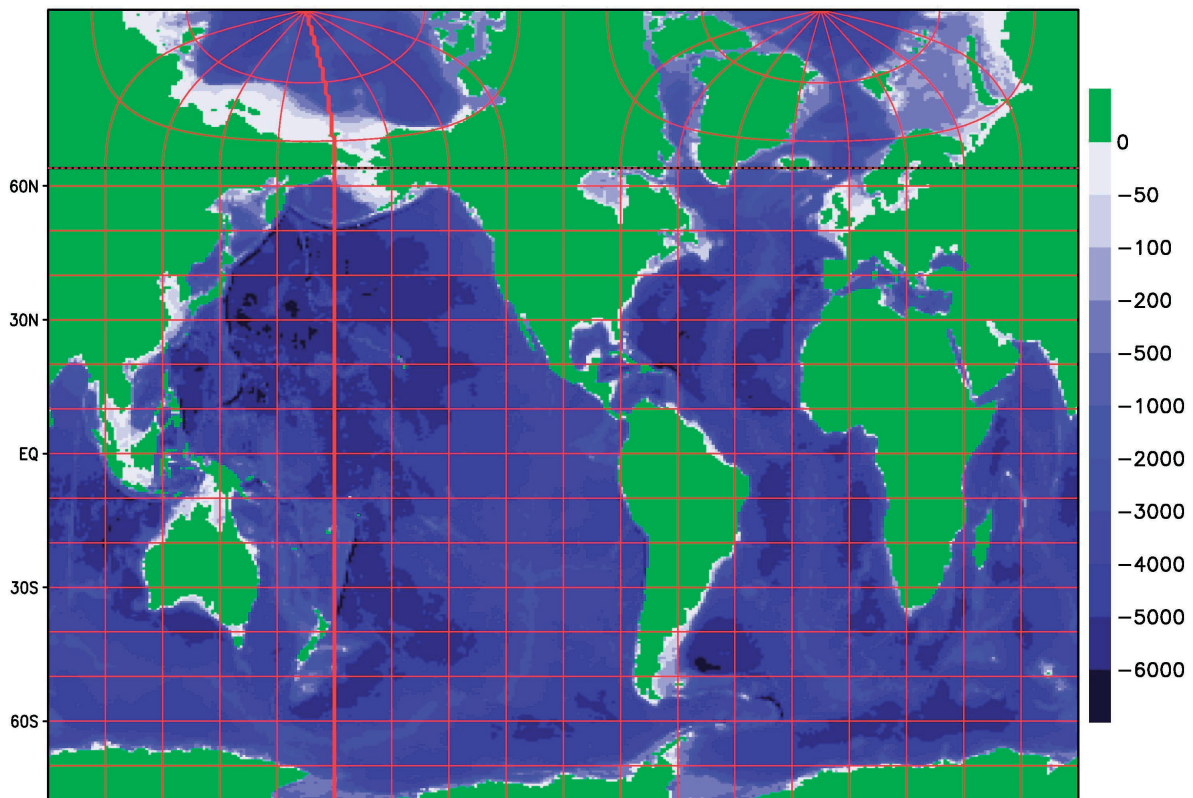


Figure 10 Topography of the ocean model component of ESM. The shades denote the bottom depth in m. The contours denote geographical latitudes and longitudes. The contour interval of latitude (longitude) is 10 (20) degree.

4.1.3. Transport algorithm

The generalized Arakawa scheme as described by Ishizaki and Motoi (1999) is used to calculate the momentum advection terms. This momentum advection scheme conserves total momentum and energy for three-dimensionally non-divergent flows over arbitrary topographies, and total quasi-entropy $((\partial v/\partial x)^2$ or $(\partial u/\partial y)^2$) for horizontally non-divergent flows.

A numerical advection scheme based on conservation of second order moments (SOM; Prather, 1986) is employed for advection of all tracers (temperature, salinity, and biogeochemical tracers). The

SOM scheme is computationally stable and almost free from numerical diffusion, so it can reproduce realistic tracer distributions in OGCMs (e.g., Hofmann and Maqueda, 2006).

4.1.4. Sub-grid-scale mixing

A flow-dependent anisotropic horizontal viscosity scheme (Smith and McWilliams, 2003) is adopted to reduce the viscosity in the direction normal to the flow (ν_N). The viscosity in the flow direction (ν_F) is set as Smagorinsky-type harmonic viscosity (Smagorinsky, 1963), $\nu_F = (4\Delta/\pi)^2 |D|$, where Δ is the grid size and $|D|$ is the strain rate. An anisotropic viscosity, $\nu_N = 0.2 \times \nu_F$, allows the equatorial undercurrent to be narrow and swift, as observed. At the lateral boundary, ν_N is set to be half of ν_F to produce a Munk boundary layer.

The following parameterizations are used for epineutral mixing processes: isopycnal diffusion (Redi, 1982; Cox, 1987) with a coefficient $500 \text{ m}^2 \text{ s}^{-1}$ and eddy-induced transport parameterized as isopycnal layer thickness diffusion (Gent and McWilliams, 1990) with a coefficient proportional to the grid size ($250 \text{ m}^2 \text{ s}^{-1}$ for 100 km).

The vertical diffusivity and viscosity are set by the turbulence closure model (Noh and Kim, 1999; Noh et al., 2005). The background vertical diffusivity consists of a horizontally uniform vertical profile, as proposed by Tsujino et al. (2000), and a parameterization for the tidally driven mixing (St. Laurent et al., 2002) near the Kuril Islands and the Sea of Okhotsk.

Seawater densities are calculated by an accurate equation of state (Tsujino et al., 2010). The vertical gravitational instabilities calculated by the model are completely eliminated at each time step by a convective adjustment scheme.

4.1.5. Solution procedure

Surface fluxes from the atmospheric component are received at the beginning of a coupling interval, and the ocean-ice component is subcycled while maintaining the global sum of the received fluxes. The relevant processes are solved in the following order.

After the local adjustments explained in section 4.3, the fluxes are used to solve the evolution of sea ice (section 4.2) and the fluxes received by the ocean are determined. Using these fluxes, the core

parts of the ocean model, the continuity equation, the baroclinic part of the momentum equation, the barotropic part of the momentum equation, and the tracer equations are solved in the order listed. The evolved states are checked for static stability, and the turbulence closure model is solved to determine vertical mixing coefficients for the next time step.

Snapshots of surface properties are sent to the atmospheric component at the end of each coupling interval.

Basically, a leap-frog scheme is employed for a time-integration. By default, the Matsuno (Euler-backward) scheme is used once per 12 time steps to suppress computational noise. This interval can be changed at run time by using a namelist parameter. A common time step is used for all processes except for the barotropic part of the momentum equation (the time step of which is independently specified). Starting at the same time as the baroclinic part, the barotropic part is subcycled (by the split-explicit method) and integrated for two baroclinic time steps. The average state during these two baroclinic time steps is returned. Typically, the time step of the ocean-ice component is 30 minutes and that of the barotropic part is 1 minute.

4.2. Sea ice model

4.2.1. General features

The sea ice part solves the fractional area, heat content, thickness, and the transport of ice categorized according to its thickness and the dynamics of the grid-cell-averaged ice pack. Heat, water, salt, and momentum fluxes are exchanged with the atmosphere and ocean. Using Scup, the sea ice part sends surface temperature, interior temperature, snow and ice thicknesses, and fractional area to the atmospheric component, and receives surface fluxes calculated by that component. The ice model is part of the ocean model and ice–ocean exchange processes are internal.

The thermodynamic part is based on Mellor and Kantha (1989). For processes that are neither explicitly discussed nor included by Mellor and Kantha (1989), such as categorization by thickness, ridging, and rheology, we adopt those of the Los Alamos sea ice model (CICE; Hunke and Lipscomb, 2006). The formulation and solving procedure of each process are briefly presented in later sections. See the MRI.COM reference manual (Tsujino et al., 2010) for details.

The fundamental property that defines the state of sea ice is its fractional area as a function of location (x, y) and thickness (h) . The equation for this distribution function, $g(x, y, h)$, is expressed as follows:

$$\frac{\partial g}{\partial t} = \frac{\partial}{\partial h} (fg) - \frac{1}{h_\mu h_\psi} \left(\frac{\partial (gh_\psi u_I)}{\partial \mu} + \frac{\partial (gh_\mu v_I)}{\partial \psi} \right) - \chi \quad (4.1)$$

where f is the thermodynamic growth rate of ice thickness, (u_I, v_I) is the velocity vector of an ice pack, and χ is the rate of change of the distribution function caused by mechanical ridging. We discretize the thickness into five categories, separated at $H_n = 0.0, 0.6, 1.4, 2.4, 3.6,$ and 30.0 m. The fractional area of the n -th category (a_n) is defined as follows:

$$a_n = \int_{H_{n-1}}^{H_n} g dh \quad (4.2)$$

Other major variables, ice and snow thickness, surface temperature, bottom temperature and salinity, and internal energy of ice, are defined for each category. Velocity is defined for an ice pack, the total ice mass in a grid cell. In the vertical direction, both ice and snow have one layer; the heat capacity of sea ice, but not of snow, is considered. The heat capacity of sea ice is due to brine and is represented by the temperature at the center of the ice. It is assumed that sea ice has the same energy (temperature) throughout the layer.

The growth rate of ice thickness is computed by solving thermodynamic processes (Section 4.2.2). Using this growth rate (f), thickness categories are remapped according to the first term on the right-hand side (r.h.s.) of Eq. (4.1) (Section 4.2.3). To compute the velocity of an ice pack (u_I, v_I) , we have to solve the momentum equation (Section 4.2.4). When the ice distribution is transported (second and third terms on the r.h.s. of Eq. (4.1)), other conservative properties such as volume and energy are also transported (Section 4.2.5). The ridging process (χ ; fourth term on the r.h.s. of Eq. (4.1)) is solved with the transported ice distribution function (Section 4.2.6).

4.2.2. Thermodynamics

In considering the thermodynamics, the thermal energy of sea ice should be defined. The energy base (i.e., zero energy) is defined here as that of seawater at 0°C . The thermal energy (enthalpy; $E(T, r)$)

of sea ice with temperature T_1 (<0 °C) and brine (salt water) fraction r is the negative of the energy needed to raise the temperature of the ice to 0 °C and melt all of it:

$$E(T, r) = r(C_{po}T) + (1-r)(-L_F + C_{pi}T) \quad (4.3)$$

where C_{po} and C_{pi} are the specific heats of seawater and sea ice, respectively, and L_F is the latent heat of melting/freezing. The brine fraction of sea ice is $r = S_I / S = mS_I/T_1$, where S_I (= 4.0 practical salinity units; psu) is the salinity of ice, T_1 is the temperature of ice defined at its center, and m determines the freezing temperature as a function of salinity.

Heat fluxes relevant to thermodynamic processes are surface heat fluxes from the atmosphere (short- and longwave radiations, latent and sensible heat fluxes), heat conduction within ice and snow, and heat fluxes between the ice bottom and the first ocean layer.

Operations to solve sea ice thermodynamic processes proceed as follows.

If the temperature of the first layer of the ocean model is below the freezing point as a function of salinity, the temperature is set to the freezing point, and the heat needed to raise the temperature, regarded as the release of latent heat, is used to form new and frazil ice. For a grid cell without sea ice, the initial ice thickness is set to 0.1 m and the fractional area is determined from the ice volume. For a grid cell where sea ice already exists, the grid mean thickness is added to each category and to open water.

The surface temperature at the top surface is computed so that the fluxes on both sides, the atmospheric heat flux and the ice interior flux, are the same. A semi-implicit method is adopted. If a new surface temperature is below the freezing point, melting does not occur. If it is not, the surface temperature is set to the freezing temperature (mS_I), and the heat flux in the ice interior is re-evaluated. The amount of melting is obtained from the imbalance.

In the ice interior, thermal energy changes according to the vertical heat flux budgets in the upper and lower parts of the ice.

At the bottom, the balances of the heat and salt fluxes, which involve the heat flux in the ice interior, fluxes caused by freezing or melting at the interface, and fluxes caused by molecular diffusion in the surface skin layer, are imposed and solved simultaneously. The same operation is applied to the open water using the air–sea flux (without solar radiation) and the surface skin layer flux.

Solar radiation in the infrared band is absorbed at the top surface. A fraction of radiation in the visible band penetrates into the ice layer and attenuates with an e -folding scale of 1.4 m^{-1} , warming the ice interior. The remainder penetrates into the ocean.

4.2.3. Vertical remapping

After the thermodynamic processes are solved, the resultant ice thickness in some thickness categories might not be within the specified bounds. Following the same method as that used in CICE, we assume that there is a thickness distribution function in each category and use it to redistribute the new thickness distribution into the original categories. Specifically, a thickness category is regarded as a Lagrange particle, and the category boundaries are displaced as a result of thermodynamics. The growth and melting rate in each category is linearly interpolated to obtain a the displacement speed of the category boundary. A linear thickness distribution function is assumed within each displaced category, and ice is remapped into the original categories by using these functions.

4.2.4. Dynamics

The equation of motion used for an ice pack is that for a continuous medium, as follows:

$$\rho_I \frac{\partial(Ah_I u_I)}{\partial t} - \rho_I Ah_I f v_I = -\rho_I Ah_I g \frac{1}{h_\mu} \frac{\partial h}{\partial \mu} + F_\mu(\sigma) + A(\tau_{AI\mu} + \tau_{IO\mu}) \quad (4.4)$$

$$\rho_I \frac{\partial(Ah_I v_I)}{\partial t} + \rho_I Ah_I f u_I = -\rho_I Ah_I g \frac{1}{h_\psi} \frac{\partial h}{\partial \psi} + F_\psi(\sigma) + A(\tau_{AI\psi} + \tau_{IO\psi}) \quad (4.5)$$

where A is concentration, h_I is thickness, and ρ_I is density of an ice pack. An ice pack is forced by stress from wind at the top (τ_{AI}) and stress from oceanic currents at the bottom (τ_{IO}). The motion is also affected by the Coriolis force (the terms with the Coriolis parameter f), the sea-level slope (h), and the internal stress of the ice ($F(\sigma)$).

To estimate the internal stress, the elastic-plastic-viscous (EVP) model by Hunke and Dukowicz (2002) is adopted as the constitutive law (the relation between stress and strain rate). The EVP model is a computationally efficient modification of the viscous-plastic model (Hibler, 1979). The EVP model treats the ice as an elastic medium, and a large local force is released by elastic waves, which would be

damped within the timescale of the wind forcing. The dynamics scheme is subcycled within the thermodynamic time step.

4.2.5. Transport

Fractional area, snow volume, ice volume, ice energy, and ice surface temperature of each category are transported using the drifting velocity of the ice pack. A multidimensional positive definite advection transport algorithm (MPDATA; Smolarkiewicz, 1984) is used. The MPDATA scheme is suitable for the transport of ice because all transported properties should be sign-definite in the ice model.

4.2.6. Ridging and adjustment

As a result of advection, the sum of the fractional areas of a grid cell might exceed one, especially where the velocity field is convergent. In such a case, it is assumed that ridging occurs in the ice to yield a sum equal to or less than one. Even if the sum is less than one, ridging or rafting might occur where the concentration of ice is high. The ridging rate is a function of deformation rates. The ridging scheme of MRI.COM3 follows that of CICE, as detailed in the MRI.COM3 reference manual.

Finally, the part of snow that is below freeboard in accordance with Archimedes' principle absorbs seawater to become sea ice. The appropriate amount of salt is extracted from the ocean.

4.2.7. Solution procedure

The sea ice model is called from the ocean model once during each oceanic time step. Thus, the time step of the processes except for the dynamics (momentum equation) is the same as that of the ocean model. The momentum equation is subcycled. Typically, the time step for the thermodynamics is 30 minutes and that for the momentum equation is 1 minute (the time steps can be specified by the user at run time).

The sea ice model uses the forward scheme of time integration and is not called from the ocean model in the backward phase of the Matsuno (Euler-backward) scheme. The momentum equation uses the backward scheme.

All variables except for ice pack velocity and stresses are defined at the tracer point of Arakawa's B-grid arrangement. Spatial discretization for transport and momentum equations uses the centered difference.

4.3. Exchange of properties with the atmospheric component

The exchange of properties with the MRI-AGCM3 atmospheric component is realized by using the simple Scup coupler developed by Yoshimura and Yukimoto (2008). The coordinate transformation tables in both exchange directions should be prepared prior to integration. The coupling interval can be specified by the user at run time. It should be a common multiple of the time steps in the atmosphere and ocean components. It is normally set to 1 hour. The time step for the ocean model is normally 30 minutes.

The boundary between MRI-AGCM3 and MRI.COM3 is placed at the bottom of the atmosphere. The fluxes above the boundary are computed by MRI-AGCM3 and received by MRI.COM3 at the beginning of a coupling interval (section 4.3.1). Sea-surface properties are sent to MRI-AGCM3 at the end of a coupling interval (section 4.3.2).

4.3.1. From atmosphere to ocean

Surface fluxes are calculated in MRI-AGCM3 and accumulated during a coupling interval. The mean fluxes during this interval are then sent to MRI.COM3. Thus, MRI.COM3 uses the surface fluxes averaged over the last 1 hour. These fluxes are kept unchanged during a coupling interval.

The following properties are exchanged.

Grid cell mean:

- Precipitation
- Sea-level pressure
- Scalar wind speed above seawater at 10 m height
- Surface wind stress on seawater
- Scalar wind stress (friction velocity) on seawater
- Scalar wind speed above sea ice at 10 m height

- Surface wind stress on sea ice
- Scalar wind stress (friction velocity) on sea ice
- Water flux due to river discharge
- Heat flux due to river discharge
- Water flux due to iceberg discharge
- Heat flux due to iceberg discharge

Separated into open-water and ice-thickness categories:

- Net long-wave radiation (upward + downward)
- Latent heat flux
- Sensible heat flux
- Net shortwave radiation (direct and visible)
- Net shortwave radiation (diffuse and visible)
- Net shortwave radiation (direct and near infrared)
- Net shortwave radiation (diffuse and near infrared)
- Evaporation/condensation/sublimation
- Surface skin temperature
- CO₂ flux at the sea surface

4.3.2. From ocean to atmosphere

The following properties (snapshots) are sent to MRI-AGCM3 at the end of a coupling interval.

- Temperature in the first level
- Salinity in the first level
- Velocity vector in the first level
- Fractional area of ice pack (all categories)
- Ice thickness (all categories)
- Snow thickness (all categories)
- Temperature at the ice or snow surface (all categories)
- Interior temperature of ice (all categories)
- Oceanic pCO₂

4.3.3. Use of surface fluxes and adjustment for conservation

The atmospheric component evaluates surface fluxes, and the ocean-ice MRI.COM3 component uses these fluxes to solve the evolution of sea-surface states and the growth and melting of sea ice.

The surface fluxes are kept basically unchanged in MRI.COM3 during a coupling interval. The following three-step procedure is used to ensure conservation. First, a numerical error that could arise during coordinate transformation is adjusted: Globally averaged total fluxes of heat and freshwater are evaluated before and after the transformation. The difference in the globally averaged heat fluxes is added to the total long-wave flux and that in the freshwater fluxes is added to precipitation or evaporation, depending on the sign of the difference.

Second, the evolution of the sea ice area during a coupling interval is considered because it would immediately result in changes to the globally averaged fluxes. These changes are evaluated at each time step, and global flux adjustments are imposed on the heat flux and freshwater flux as in the first step.

Finally, the evolution of ice surface temperature is considered. Without a feedback mechanism (i.e., with fluxes fixed), the ice surface skin temperature obtained by imposing the flux balance would exhibit unstable behavior. To prevent this, the ice surface skin temperature used for evaluating upward blackbody radiation is updated at each time step of MRI.COM3 during a coupling interval. The resultant inconsistencies in total longwave fluxes are averaged globally and added to the heat flux between ice and ocean. Thus, the residual flux is consumed by the ocean. Note that the sum of heat flux adjustments arising from these procedures is typically less than 1 W m^{-2} .

5. Aerosol model (MASINGAR mk-2)

Atmospheric aerosols influence the climate by perturbing the Earth's radiation budgets in several ways. A direct radiative effect is caused by the direct scattering and absorption of atmospheric radiation by aerosols. An indirect radiative effect is caused by aerosols also acting as cloud condensation nuclei, which affects properties of clouds such as cloud albedo (Twomey, 1974; Twomey, 1991), precipitation formation, and cloud lifetime (Albrecht, 1989). Absorptive aerosols such as black carbon or mineral dust warm the atmosphere and reduce solar radiation at the surface, which increases atmospheric stability. Absorptive aerosols can locally inhibit cloud formation or reduce cloud cover by heating cloud droplets. This effect is called the semi-direct aerosol effect (Hansen et al., 1997). Moreover, absorptive aerosols deposited on a snow surface reduce the albedo of the snow surface and enhance the melting of the snow (Hansen and Nazarenko, 2004).

In MRI-ESM1, atmospheric aerosols are calculated with a global aerosol model called MASINGAR mk-2 (Model of Aerosol Species in the Global Atmosphere), which is coupled with the Scup coupler library (Yoshimura and Yukimoto, 2008). MASINGAR mk-2 is an improved version of the MASINGAR aerosol model (Tanaka et al., 2003) modified to work as a component of MRI-ESM1. The model treats five aerosol species: non-sea-salt sulfate, black and organic carbon, sea salt, and mineral dust. The grid resolution of the model is variable, and can be different from that of the coupled AGCM.

5.1. Coupling with the atmospheric general circulation model MRI-AGCM3

The aerosol model receives the meteorological fields and surface conditions from the AGCM through the coupler. The meteorological fields include horizontal wind components, air temperature, specific humidity, convective mass flux, precipitation and evaporation with convective and large-scale clouds, the vertical eddy diffusion coefficient, and surface pressure. The surface conditions include near-surface wind speed, surface air temperature, ground temperature, snow amount, land-use type, vegetation amount, and leaf area index. The MASINGAR mk-2 aerosol model sends the concentrations of the five aerosol species and the deposition fluxes of absorptive aerosols (black carbon and mineral dust) to MRI-AGCM3 to be used in calculations of the direct and indirect radiative effects of the

aerosols and of the snow albedo. The sea-salt aerosol is calculated in 6 size bins in the aerosol model, but is sent in 2 bins (smaller and larger than 1 μm).

5.2. Coupling with the chemistry climate model MRI-CCM2

The interaction of aerosols with atmospheric chemistry is incorporated into MRI-ESM1 by coupling of the MASINGAR mk-2 aerosol model with the MRI-CCM2 atmospheric chemistry model, which is described in section 6. MASINGAR mk-2 receives concentrations of OH, H₂O₂, HO₂, O₃, NO₃, and O(³P) for the calculation of chemical reactions involving the sulfate aerosol. If MRI-CCM2 is not coupled with MRI-ESM1, then MASINGAR mk-2 uses monthly averaged concentrations of the chemical species pre-calculated by MRI-CCM2. On the other hand, MASINGAR mk-2 sends the three-dimensional surface area density of the aerosols to MRI-CCM2, enabling it to incorporate heterogeneous chemical reactions on the aerosol surface.

5.3. Processes in the global aerosol model

5.3.1. Atmospheric transport

Atmospheric transport is calculated using a semi-Lagrangian advection scheme and schemes for sub-grid turbulent vertical diffusion and convective transport. The vertical eddy diffusion coefficient is taken from that of water vapor, calculated in the AGCM. Convective transport is calculated using the updraft mass flux from the cumulus convection scheme (AS-type or Yoshimura scheme) in MRI-AGCM3.

Aerosol particles are subject to gravitational settling relative to air motion and are assumed to fall with the terminal velocity V_s . The terminal velocity V_s is calculated under the assumption that the particles are spherical as

$$V_s = \frac{2C_c(\rho_p - \rho_a)gr_p^2}{9\mu}, \quad (5.1)$$

where ρ_a is the air density; ρ_p and r_p are the density and radius of the particle, respectively; g is gravitational acceleration; and μ is the viscosity of the air. C_c is the Cunningham slip-flow correction, expressed as

$$C_c = 1 + Kn[A + B\exp(-C / Kn)] \quad (5.2)$$

where Kn is the Knudsen number for air, and the coefficients A , B , and C are set to 1.257, 0.4, and 1.1.

5.3.2. Dry and wet deposition processes

Dry deposition is parameterized by the resistance-in-series model (Seinfeld and Pandis, 1997), which includes turbulent impaction and gravitational settling. Wet deposition is distinguished between in-cloud and below-cloud scavenging and is also categorized by cloud type (convective or large-scale) and species (aerosol or gas; accommodation with water droplets). For in-cloud scavenging by large-scale precipitation, we used the parameterization developed by Giorgi and Chameides (1986). Both the dry and wet deposition schemes for sea salt and mineral dust aerosols are particle-size dependent.

For water-soluble gases such as SO_2 , wet scavenging is calculated simultaneously with the aqueous-phase chemistry. The fraction of a water-soluble gas that is in liquid water is assumed to follow Henry's law of equilibrium, which is temperature and pH dependent. The rate of wet deposition is calculated as the ratio of the new rainwater formation rate to the total water in the grid box (cloud water plus rainwater formation). At temperatures below -20 °C, all cloud droplets are assumed to be frozen and precipitation is assumed to be snow; thus, wet scavenging of water-soluble gases is ignored, whereas aerosol particles are assumed to be scavenged by either rain or snow. Evaporation of rainwater is considered when calculating the wet deposition rate. When evaporation occurs, a fraction of the trace elements is released back to the air. This fraction of released trace elements is assumed to be proportional to the amount of evaporated rainwater.

5.3.3. Emission processes and chemical reactions

For the emission processes of anthropogenic sulfur compounds and carbonaceous aerosols, prescribed emission inventories are used. The emissions of oceanic DMS, sea salt, and mineral dust are calculated from the meteorological and surface conditions.

Sulfate

The emission and formation of sulfate aerosol is based on Tanaka et al. (2003), but some modifications are applied. Sulfate aerosols are mainly formed from gaseous and aqueous phase reactions of SO₂ and DMS. Emissions of SO₂ from fuel consumption, ships, and biomass burning are taken from prescribed inventories. The global source distribution from volcanos is taken from GEIA (Andres and Kasgnoc, 1998).

Emission of DMS from the ocean is calculated as a function of the surface seawater DMS concentration and its piston velocity. Climatological monthly averaged surface seawater DMS concentrations are adopted from Kettle et al. (1999). The piston velocity of DMS is calculated as a function of the 10-m wind velocity and the Schmidt number of DMS at the sea-surface temperature. This model implements two parameterizations of DMS piston velocity. First, the widely used empirical scheme of Liss and Merlivat (1986) is employed as the default scheme:

$$k_{\text{DMS}} = k_u \left(\frac{\text{Sc}_{\text{DMS}}(T_{\text{SST}})}{\text{Sc}_{\text{CO}_2}(20)} \right)^\alpha \quad (5.3)$$

where α is an empirical parameter that is $-2/3$ if wind speed at 10 m height (U_{10}) is below 3.6 m s^{-1} and $-1/2$ otherwise. $\text{Sc}_{\text{CO}_2}(20)$ is the Schmidt number of CO₂ at the sea surface temperature of 20 °C (= 595), $\text{Sc}_{\text{DMS}}(T_{\text{SST}})$ is the Schmidt number of DMS at sea-surface temperature T_{SST} (°C) calculated by the formula of Saltzman et al. (1993),

$$\text{Sc}_{\text{DMS}} = 2674.0 - 147.12T_{\text{SST}} + 3.726T_{\text{SST}}^2 - 20.038T_{\text{SST}}^3 \quad (5.4)$$

The coefficient k_u is expressed as a function of U_{10} :

$$k_u = \begin{cases} 0.17U_{10} & \text{for } U_{10} \leq 3.6 \text{ m s}^{-1} \\ 2.85U_{10} - 9.65 & \text{for } 3.6 < U_{10} \leq 13 \text{ m s}^{-1} \\ 5.9U_{10} - 49.3 & \text{for } U_{10} > 13 \text{ m s}^{-1} \end{cases} \quad (5.5)$$

To reduce computational costs, hydrogen sulfide (H₂S), carbon disulfide (CS₂), methane sulfonic acid (MSA), dimethyl sulfoxide (DMSO), and dimethyl sulfone (DMSO₂) are not considered.

For the formation of stratospheric sulfate aerosols, carbonyl sulfide (OCS) and SO₃ are added. Because the lifetime of OCS is very long and its mixing ratio is almost stable, the mixing ratio of OCS is assumed to be a constant at 500 pptv near the ground.

Black and organic carbon

Carbonaceous aerosols are classified as BC or OC. We assume that 80% of BC and 50% of OC are emitted as hydrophobic material, following Cooke et al. (1999). We also assume that the hydrophobic carbonaceous aerosols become hydrophilic over time, with an e -folding time of 1.2 days. Hydrophobic carbonaceous aerosols are scavenged by dry deposition only, whereas hydrophilic carbonaceous aerosols are scavenged by both dry and wet deposition. No chemical sinks for carbonaceous aerosols are assumed in this model. The particle densities of OC and BC are assumed to be 1.5 and 1.25 g cm⁻³.

Sources of carbonaceous aerosols are roughly divided into anthropogenic emissions, biomass burning, and volatile organic compound (VOC) gas emissions. Emissions of BC and OC from fuel consumption, ships, and biomass burning, and emission of BC from aircraft are taken from prescribed inventories. In the production of OC aerosol from the terrestrial emission of VOCs, we assume that terpene is converted to OC by gas-to-particle conversion. The monthly mean terpene emission inventory is adopted from the 1° × 1° resolution maps of GEIA databases (Guenther et al. 1995). We assume that 10% of emitted terpene is converted to OC aerosol. This secondary source of OC accounts for 11.8 TgC yr⁻¹.

Sea salt

Sea-salt aerosol is logarithmically divided into size bins ranging from 0.2 to 20 μm in diameter. The number of size bins is reduced from 10 of previous version (Tanaka et al. 2003) to 6, considering the computational cost of long-term climate simulations. Strong winds over the ocean surface produce sea salt, indirectly by bursting air bubbles during whitecap formation and directly by spume production. We adopted the empirical parameterization of the production mechanisms developed by Gong (2003), who improved the parameterization of Gong et al. (1997) and Monahan et al. (1986). The density function dF/dr (particles m⁻² s⁻¹ μm⁻¹) of the sea-salt production rate by indirect mechanisms is

$$\frac{dF_0}{dr} = 1.373U_{10}^{3.41}r^{-A}\left(1 + 0.057r^{3.45}\right) \times 10^{\left(1.607\exp(-B^2)\right)} \quad (5.6)$$

where U_{10} is the wind speed at 10 m (m s⁻¹) and r is the particle radius (μm). The parameters A and B are defined as

$$A = 4.7(1 + \Theta r)^{-0.017r^{-1.44}} \quad (5.7)$$

$$B = (0.433 - \log r) / 0.433 \quad (5.8)$$

Following Gong (2003), the parameter Θ is set to 30. Because the size range of the direct mechanism is larger than the maximum size bin (20 μm), the direct mechanism is neglected. The sea-salt emission flux of each size bin is calculated by integrating the formula (5.6) over the size range of each size bin.

Mineral dust

In this model, the dust emission flux into the atmosphere is calculated according to saltation-bombardment theory and source areas are determined by vegetation cover, snow cover, land-use type, and soil type. Here, we briefly describe the calculation of the dust emission flux. Tanaka and Chiba (2005, 2006) give more detailed descriptions for the treatment of mineral dust aerosol.

The mobilization of soil particles is initiated when the friction velocity on a bare surface (u_*) exceeds a threshold value called the threshold friction velocity (u_{*t}), which is calculated using the formula of Shao and Lu (2000) with the soil moisture factor (f_w) of Fécan et al. (1999),

$$u_{*t}(D) = f_w \sqrt{A_N \left(\frac{\rho_p g D}{\rho_a} + \frac{\Gamma}{\rho_a D} \right)} \quad (5.9)$$

where D is the particle diameter, g is gravitational acceleration, ρ_a is air density, ρ_p is particle density, $A_N = 0.0123$, and $\Gamma = 3 \times 10^{-4} \text{ kg s}^{-2}$. The factor f_w is calculated by

$$f_w = \begin{cases} 1 & w \leq w_r \\ \sqrt{1 + a[100(w - w_r)]^b} & w > w_r \end{cases} \quad (5.10)$$

where w is the gravimetric soil water content and w_r is the threshold gravimetric soil water content. The empirical constants a and b are set to $a = 1.21$ and $b = 0.68$.

The dust flux in the size range $[D_i, D_{i+1}]$ is calculated by using the theory of Shao et al. (1996),

$$\Delta F_{i0} = CA \frac{2}{3} \frac{\rho_p \gamma}{\rho_a} \int_{D_i}^{D_{i+1}} \frac{\beta_2(D_d)}{u_{*t}(D_d)^2} p(D_d) dD_d \int_0^\infty \beta_1(D_s) \tilde{Q}(D_s) p(D_s) dD_s \quad (5.11)$$

where D_d is the diameter of emitted dust particles, D_s is the diameter of saltating particles, $\tilde{Q}(D_s)$ is the mass flux of saltating particles, $p(D)$ is the size distribution of the parent soil, A is the erodible areal fraction of the model grid, and C is a global tuning factor, chosen to yield an annual global source strength of about 2100 Tg yr $^{-1}$ (Penner et al., 2001).

Following Shao et al. (1996), $\gamma \sim 2.5$, and β_1 and β_2 appear as functions of D_s and D_d ,

$$\beta_1(D_s) = 0.125 \times 10^{-4} \ln(D_s) + 0.328 \times 10^{-4} \quad (5.12)$$

$$\beta_2(D_d) = \exp(-140.7D_d + 0.37) \quad (5.13)$$

The saltation flux $\tilde{Q}(D_s)$ is calculated with a formula from Owen (1964)

$$\tilde{Q}(D_s) = \begin{cases} \frac{c_s(D_s) \rho_a u_{*s}^3}{g} \left(1 - \frac{u_{*t}(D_s)^2}{u_{*s}^2} \right) & u_{*s} > u_{*t} \\ 0 & u_{*s} \leq u_{*t} \end{cases} \quad (5.14)$$

where

$$c_s(D_s) = 0.25 + \frac{V_s(D_s)}{3u_{*s}}, \quad (5.15)$$

and $V_s(D_s)$ is the gravitational settling velocity of a saltating particle of diameter D_s . The size distribution of the parent soil is specified by using the global soil texture database of Webb et al. (2000).

The erodible areal fraction A is expressed in the following factorial form:

$$A = (1 - A_v)(1 - A_s)(1 - A_w) A_l A_t \quad (5.16)$$

where A_v , A_s , A_w , A_l , and A_t represent the factors of vegetation cover, snow cover, water cover, land-use type, and soil type. We used the soil-type data set from Zobler (1986), which divides the soil into 106 types, with a horizontal resolution of $1^\circ \times 1^\circ$. The soil type ‘‘lithosol’’ is excluded as a possible dust source, because it consists of hard rocks from the mountainous regions, according to Tegen and Fung (1995). The soil-type erodibility factor is $A_t = 0$ for lithosol, and $A_t = 1$ for other soil types.

The size distribution of mineral dust aerosol is logarithmically divided into size bins ranging from diameter of 0.2 to 20 μm . The number of size bins is reduced from 10 of previous version (Tanaka et al. 2003) to 6, considering the computational cost of long-term climate simulations.

6. Atmospheric (Ozone) chemistry model (MRI-CCM2)

Tropospheric ozone is a major greenhouse gas now ranked third following CO₂ and CH₄ (IPCC-AR4, 2007), whereas the destruction of stratospheric ozone during the most recent several decades by man-made ozone-depleting gases such as CFCs potentially increases surface ultraviolet radiation (e.g., WMO/UNEP, 2007) and impacts on the earth's climate (e.g., Son et al., 2008), especially over the Southern extra-tropics. The increase in photochemical oxidants near the earth's surface since the industrial era can also harm humans and vegetation. A CCM for predicting global distributions of atmospheric trace gases such as ozone along with chemistry–climate interactions is an invaluable tool for addressing these environmental issues. A CCM developed at MRI (Deushi and Shibata, 2010; Shibata et al., 2005) called MRI-CCM2 is incorporated into MRI-ESM1 as a component model to evaluate the impacts of changes in ozone and other trace gases on the earth's climate. The target region of MRI-CCM2 is from the surface to the upper stratosphere. In MRI-ESM1, concentrations of radiatively active gases (ozone, CH₄, N₂O, and CFCs) calculated by MRI-CCM2 are used in the AGCM radiation module to consider chemistry–radiation coupling processes. Chemical coupling processes between trace gases and aerosols can also be considered, wherein MRI-CCM2 takes into account heterogeneous reactions on sulfate and sea-salt aerosol surfaces using concentrations predicted by the MASINGAR mk-2 aerosol model. MRI-CCM2 simulates the following processes: chemical conversion of trace gases, (grid-scale) advective transport, (sub-grid-scale) convective transport and boundary-layer diffusion, dry and wet deposition, and emissions. MRI-CCM2 incorporates a detailed tropospheric ozone chemical mechanism, which includes elaborate HO_x-NO_x-CH₄-CO photochemistry and a near-explicit degradation mechanism of nonmethane hydrocarbons (NMHCs), and a major stratospheric ozone chemical mechanism that treats heterogeneous reactions on type I and II polar stratospheric clouds and sulfate aerosols as well as gas-phase reactions. In all, MRI-CCM2 includes 90 chemical species and treats 243 chemical reactions: 168 gas-phase reactions, 59 photochemical reactions, and 16 heterogeneous reactions. A hybrid semi-Lagrangian transport scheme is used for chemical species, in which the advection equation is solved with the mass conservation equation. Emissions of NO_x, CH₄, CO, NMHCs, N₂O, CFCs, and halons include sources from industry, biomass burning, vegetation, soil, ocean, aircraft, lightning, and cosmic rays.

The seasonal cycle of the zonal-mean total ozone during 1978–1980 simulated by MRI-ESM1 as a function of months is compared with observation in Figure 11. The observed ozone is from satellite measurements by the total ozone mapping spectrometer (TOMS) and solar backscattered ultraviolet (SBUV) (TOMS/SBUV merged total and profile ozone data sets based on the version 8 retrieval algorithm; http://code916.gsfc.nasa.gov/Data_services/merged). The model generally captures well the observed features of the total ozone distribution. In the tropics, the simulated total ozone shows little bias throughout the year and the seasonal cycle is fairly well reproduced. The model also simulates the observed seasonal march in the northern extratropics, where a high-latitude total ozone maximum occurs in the late winter and early spring. In the southern mid-latitudes, however, positive biases of several tens of Dobson units (DU) are simulated from winter to spring. Figure 12 illustrates latitude–pressure cross sections of observed and simulated zonal-mean ozone volume mixing ratios in the stratosphere for January and July. The observations for 1978–1985 are based on SBUV satellite data, which cover the middle atmosphere from 50 to about 0.3 hPa. The model reproduces well the ozone core region in the equatorial upper stratosphere centered at 10 hPa, although it slightly underestimates the volume mixing ratio by up to 1 ppmv. The simulated and observed annually averaged zonal-mean ozone in the troposphere during the 1990s are shown in Figure 13. The simulated tropospheric ozone quantitatively captures observed features such as tropical low ozone mixing ratios near the surface extending upward due to intensive convective activity and sharp vertical gradients in the extratropics that approximately parallels the tropopause.

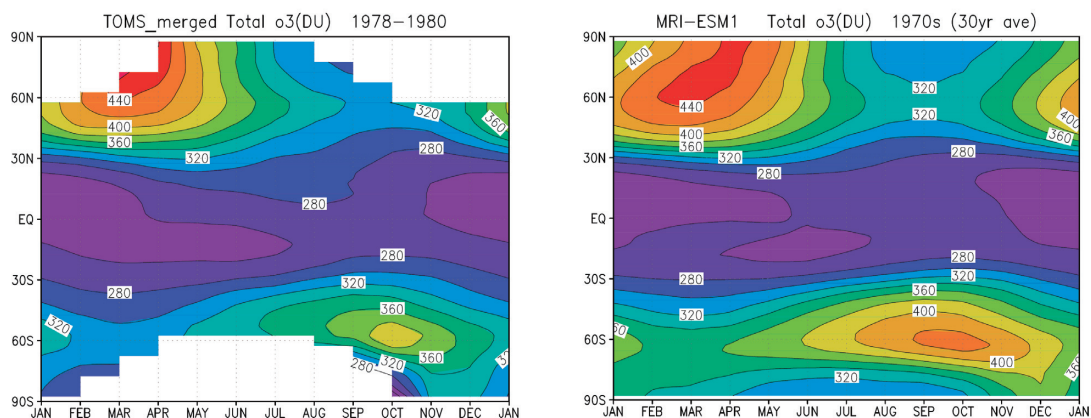


Figure 11 Month-latitude cross sections of the zonal-mean total ozone (in DU) for TOMS/SBUV observation averaged over the period of 1978–1980 (left) and the 1970s climatology of the MRI-ESM1 simulation (right). Contour interval is 20 DU.

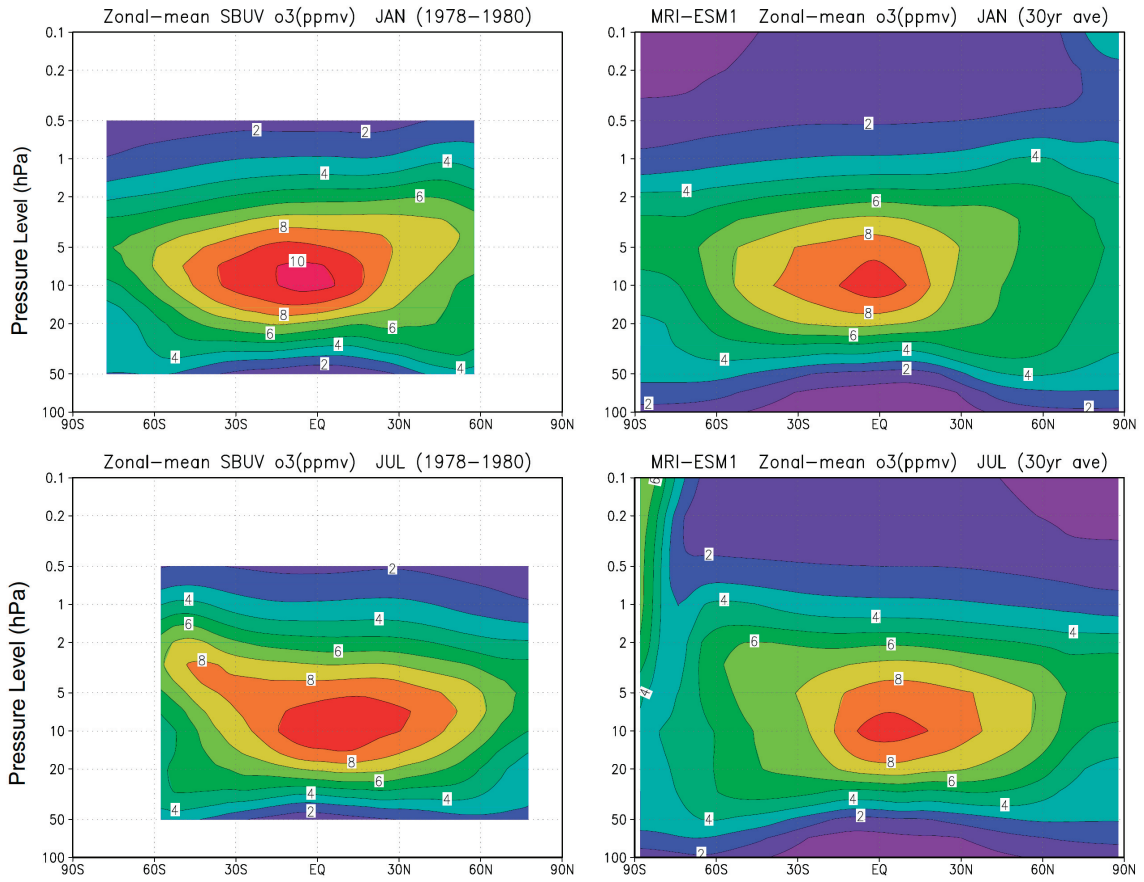


Figure 12 Latitude-pressure cross section of zonal-mean stratospheric ozone mixing ratios (in ppmv) in January (upper) and July (lower) for SBUV observation averaged over the period of 1978-1980 (left) and the 1970s climatology of the MRI-ESM1 simulation (right). Contour interval is 1 ppmv.

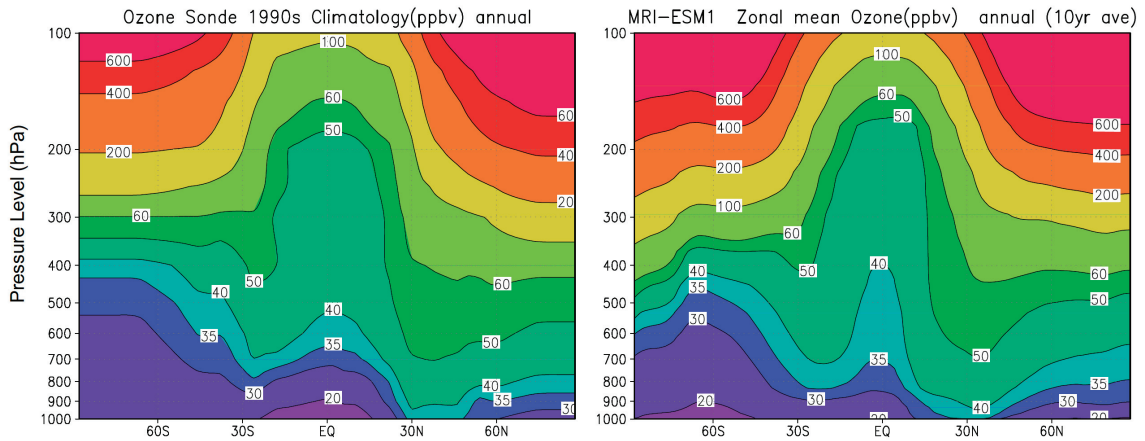


Figure 13 Annually averaged zonal-mean ozone mixing ratios (in ppbv) in the troposphere for sonde observation compiled by Logan (1999) (left) and the 1990s climatology of the MRI-ESM1 simulation (right).

7. Ice-sheet and Iceberg discharge

SMIST (Simple Model of Ice SheeT) is used as the ice-sheet component of MRI-ESM1. When the SWE is larger than 10 m over the land surface, the excess snow is taken away from the land surface model and treated as an iceberg. The ice mass and its energy are passed to SMIST and transported by SMIST to the ocean through a TRIP channel (Oki and Sud, 1998). The algorithm is almost the same as the GRiveT algorithm (Section 3.8), but without any lake ($a = 0$). The energy E is defined as

$$E = (c_{\text{ice}} (T - T_{\text{frez}}) - L') I.$$

Here, c_{ice} is the specific heat constant of ice, T is the temperature, T_{frez} is 273.15 K (freezing point), L' is the latent heat of fusion of ice, and I is the ice mass.

SICOPOLIS (SImulation COde for POLythermal Ice Sheets; Greve 1997), a 3-D dynamic/thermodynamic model that simulates the evolution of large ice sheets, is also planned to be a component of MRI-ESM1. For the present, the effect of long-term (longer than a millennium) change of ice sheets can be calculated by a semi-offline method using SICOPOLIS.

8. Carbon cycle

8.1. Terrestrial carbon cycle

The terrestrial biosphere absorbs CO₂ from the atmosphere by producing vegetation and releases CO₂ into the atmosphere by decomposition of soil organic carbon. These processes of the terrestrial biosphere can significantly affect the atmospheric CO₂ concentration. For example, the terrestrial biosphere is considered to enhance future global warming by warming-enhanced decomposition of soil organic carbon (climate–carbon cycle positive feedback, e.g., Friedlingstein et al., 2006). Therefore, the terrestrial carbon cycle process is an essential component of the earth system model for the accurate estimation of climate change. The terrestrial carbon cycle model included in MRI-ESM1 is based on models of the biochemical processes of photosynthesis on the organism-leaf level (Woodward et al., 1995; Sellers et al., 1996) and on a dynamic global vegetation model on the ecosystem-biogeochemical level (Sitch et al., 2003). The model is fundamentally improved from the previous MRI carbon cycle model (Obata, 2007), in which biological processes such as net primary production (NPP) are simply and empirically represented by meteorological factors such as temperature and precipitation and by a simple CO₂ fertilization effect. The simple, empirical processes in the previous model led to overestimation of NPP at higher temperatures, and would thus lead to the underestimation of projected warming. This NPP overestimation should be improved by considering more detailed biochemical and ecosystem processes. The processes of the improved model are briefly described below.

On the leaf level, the model calculates biochemical photosynthesis processes and the dependence of CO₂ exchange on stomatal conductance, which in turn depends on temperature and soil moisture (Woodward et al., 1995). The following information is mainly from Woodward et al. (1995), who describe the methods and parameters of the model in detail. The model is able to simulate the net photosynthetic effects of changes in the photorespiratory rate, for example in response to changes in CO₂ concentration or irradiance. The photosynthetic rate of a leaf is determined by the minimum rate of at least two biochemical processes: [1] the rate of carboxylation W_c due to the amount, kinetic properties, and activation state of ribulose biphosphate carboxylase-oxygenase (Rubisco), and [2] the rate of carboxylation W_j controlled by the rate of ribulose biphosphate (RuBP) regeneration in the Calvin cycle, a process that is limited by the rate of electron transport (Farquhar et al., 1980).

The net rate of CO₂ assimilation implied by these biochemical processes is

$$A_b = V_c (1 - 0.5p_o/\tau pCO_2) - R_d, \quad (8.1)$$

where the rate of carboxylation $V_c = \min(W_c, W_j)$; p_o and pCO_2 are the internal partial pressures of O₂ and CO₂ respectively; τ is the specificity factor of Rubisco for CO₂ relative to O₂; and R_d is the rate of respiration in light due to processes other than photorespiration. Typical values of p_o and R_d are 21 000 Pa and 0.82 $\mu\text{mol m}^{-2} \text{s}^{-1}$. The specificity factor τ depends on temperature: $\tau(T_k) = \exp(-3.949 + 28.99/0.00831T_k)$, where T_k is absolute temperature.

[1] If Rubisco controls photosynthesis, then the carboxylation rate is a hyperbolic function of pCO_2 :

$$W_c = V_c^{max} pCO_2 / [pCO_2 + K_c(1+p_o/K_o)], \quad (8.2)$$

where V_c^{max} is the maximum rate of carboxylation by Rubisco. The parameters K_c and K_o are Michaelis coefficients for carboxylation and the competing process of oxygenation by Rubisco (Farquhar et al., 1980).

[2] If the RuBP regeneration rate controls photosynthesis, then the carboxylation rate depends on the rate of electron transport J :

$$W_j = J pCO_2 / 4(pCO_2 + p_o/\tau). \quad (8.3)$$

Irradiance drives the electron transport J (e.g., Farquhar et al., 1980).

Stomatal conductance controls the diffusion of CO₂ from the atmosphere into the intercellular air spaces and thus the supply of CO₂, which affects the rates of carboxylation W_c and W_j . Internal CO₂ adjusts to balance supply by diffusion and demand by biochemical photosynthetic processes.

The CO₂ assimilation rate implied by the diffusion gradient in the CO₂ concentration from the atmosphere to the intercellular air spaces is

$$A_d = (pCO_{2\text{air}} - pCO_2) g_s / 160, \quad (8.4)$$

where A_d is the CO₂ assimilation rate ($\mu\text{mol m}^{-2} \text{s}^{-1}$), g_s is stomatal conductance to water vapor ($\text{mmol m}^{-2} \text{s}^{-1}$), and $pCO_{2\text{air}}$ is atmospheric CO₂ partial pressure (Pa). The stomatal conductance is empirically derived from environmental conditions, modified to account for the effects of soil moisture: $g_s = (g_0(T) + g_1(T)AR_h/pCO_{2\text{air}}) k_g(w_s)$, where R_h is the relative humidity of the air surrounding the leaf and A is the CO₂ assimilation rate. The parameter g_0 is the stomatal conductance when A_d is zero at the light compensation point, and g_1 is an empirical sensitivity coefficient. The function $k_g(w_s)$ describes the response of stomatal conductance to soil water content w_s .

The internal CO₂ partial pressure, $p\text{CO}_2$, is determined by iteratively solving the nonlinear equation that arises by setting the assimilation rate implied by the diffusion gradient (Eq. (8.4)) equal to the assimilation rate indicated by biochemical processes (Eq. (8.1)) with carboxylation rate V_c equal to the minimum of W_c and W_j .

The model described above is for C₃ photosynthesis plants. In the case of C₄ photosynthesis plants, the model can be extended by incorporating a corresponding representation of C₄ photosynthesis (Sellers et al., 1996; Haxeltine and Prentice, 1996), in which CO₂ fertilization is saturated. The leaf-level photosynthesis model is calculated with a time interval of 30 minutes to 1 hour in conjunction with the land-surface model (Section 3.6) of the AGCM. The calculated stomatal conductance is used for water and latent heat fluxes to the atmosphere in the land-surface model. The calculated net photosynthesis is averaged over a day or a month and then used to drive the following vegetation model.

On the ecosystem level, the terrestrial biosphere is subdivided into leaves, stems, roots, litter, and humus. The driving input for the ecosystem is NPP (gross primary production minus plant maintenance respiration), which is partitioned among leaves, stems, and roots. The carbon content of each component is predicted by the carbon outflow equivalent to its fractional content, depending on the component's turnover time, and by carbon inflow from the donor component. The exchange of CO₂ between the atmosphere and the ecosystem is evaluated by the difference between NPP and soil respiration. These calculations are carried out in each terrestrial grid of the AGCM. These basic model structures are the same as in the previous model (Obata, 2007). In the improved model, the vegetation consists of 10 plant functional types (PFTs): 8 woody (2 tropical, 3 temperate, 3 boreal) and 2 herbaceous (tropical, temperate) types. Responses of the PFTs, litter, and humus are calculated with formulations similar to those in the Lund-Potsdam-Jena Dynamic Global Vegetation Model (Sitch et al., 2003), who describe the methods and parameters in detail.

Each PFT population is characterized by a set of variables describing the state of the average individual, and by the population density. For woody PFTs, the average individual is defined by its crown area (m²) and the sizes of three tissue pools (gC): leaf mass, sapwood mass, and fine root mass. Herbaceous PFTs are treated more simply: population density is arbitrarily set to 1, so that leaf mass and fine root mass represent grid cell area averages (gC m⁻²), and sapwood is undefined. Above- and below-ground litter carbon pools with a turnover time of about 3 years and 2 soil carbon pools with intermediate (~30 years) and slow (~1000 years) turnover times are defined for the entire grid cell.

In the calculation, maintenance and growth respiration are subtracted from net photosynthesis, obtained from the leaf-level biochemical model described above, and tissue turnover reduces individual plant biomass, with dead leaf and root tissue entering the litter pools. The remaining photosynthate is allocated to the vegetation parts, satisfying allometric relationships. Litter and soil organic matter decomposition are driven by seasonal temperatures and soil moisture status. These calculations are carried out for a time interval of 1 day to 1 month. Population densities are updated annually based on establishment and mortality. If 20-year mean values of bioclimatic variables fall outside the PFT's survival limits, the entire population is killed.

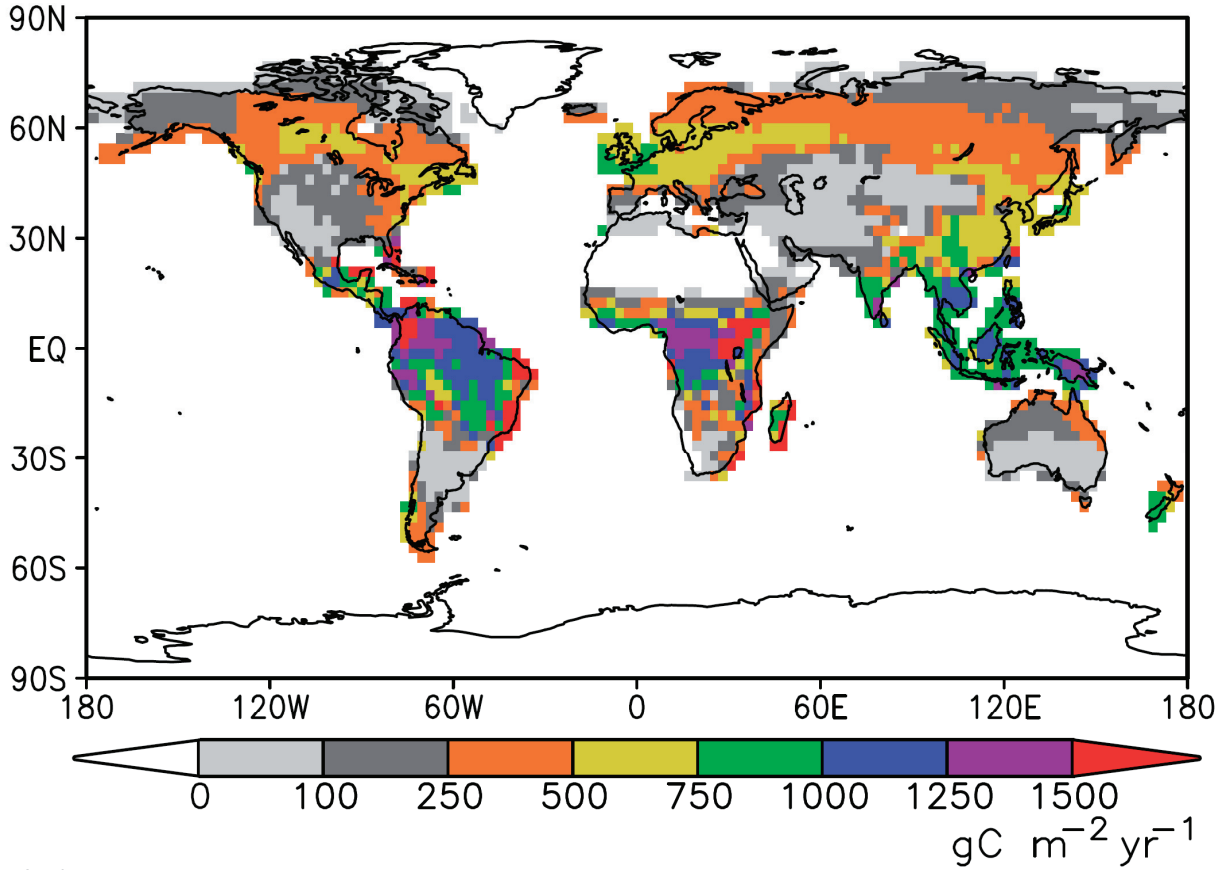
In a preliminary trial, the terrestrial carbon cycle model described above was included in an MRI climate-carbon cycle model (Obata, 2007) based on MRI-CGCM2 (Yukimoto and Kitamura, 2003) instead of the previous simple terrestrial carbon cycle model. The preindustrial steady state is well reproduced, with high values of NPP and leaf area index in the tropics because of the warm, wet conditions (Fig. 14), and a global NPP of 56 GtC yr^{-1} , consistent with previous estimates (e.g., Prentice et al., 2001).

8.2. Oceanic Carbon Cycles

Biogeochemical models [see Tsujino et al., 2010, for details] are composed of inorganic carbon-cycle and ecosystem component models. In the inorganic carbon-cycle component, $p\text{CO}_2$ at the sea surface is determined from dissolved inorganic carbon (DIC) and Alkalinity (Alk) values at the sea surface, which needs the ecosystem component. The difference in $p\text{CO}_2$ between the atmosphere and ocean determines uptake or release of CO_2 from the ocean to the atmosphere, and is essential for simulating the CO_2 concentration in the atmosphere. Inorganic carbonate chemistry and partial pressure physics are well understood and can be reproduced with fair accuracy. The ecosystem component treats various biological activities, and gives sources and sink of the nutrients, DIC, Alk, and dissolved oxygen through these activities, but our knowledge of them is far from complete.

The ocean ecosystem model is based on Oschiles (2001). The prognostic variables for the ecosystem model are phytoplankton (P), zooplankton (Z), detritus (D), dissolved Inorganic Nitrate (NO_3), dissolved inorganic phosphate (PO_4), and dissolved oxygen (O_2). The Tracer concentrations follow advective diffusive equations with source-minus-sink (SMS) terms of exchange between different

(a) Net Primary Production



(b) Leaf Area Index

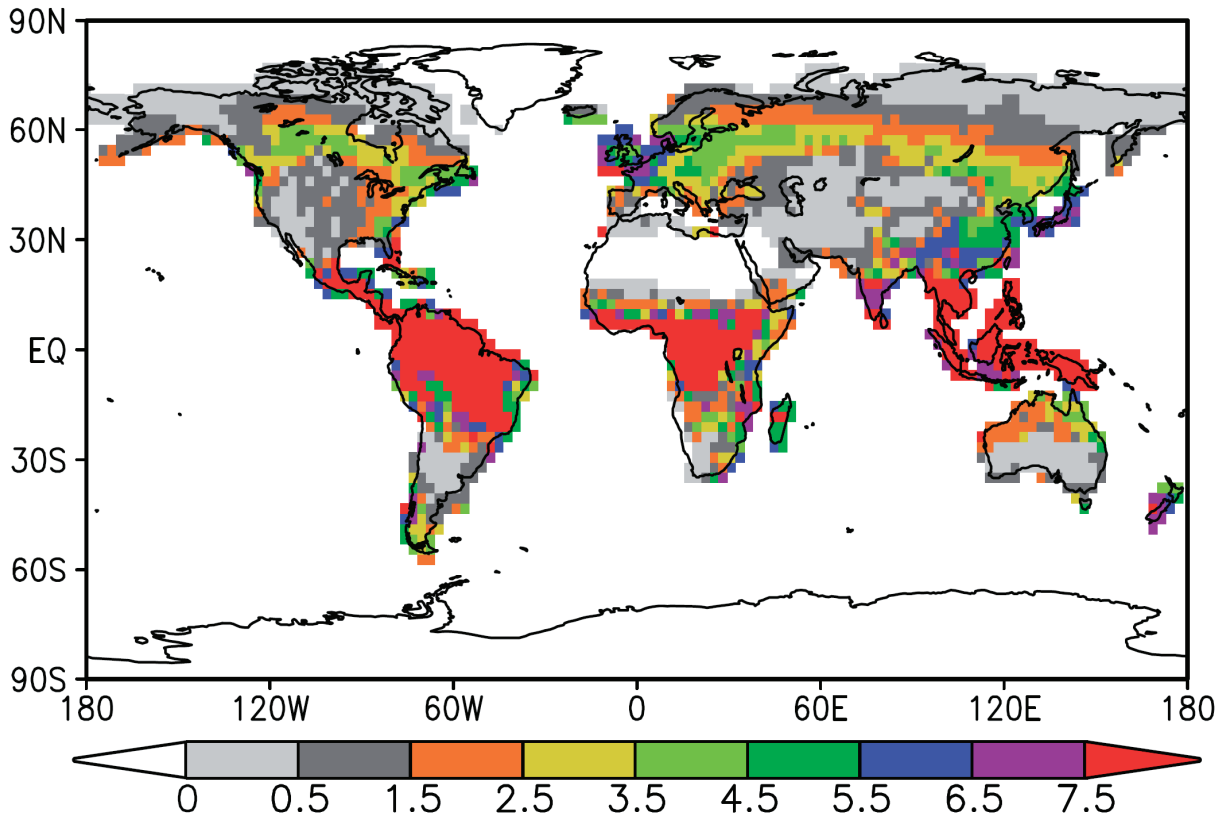


Figure 14 (a) Net primary production and (b) leaf area index in the preindustrial state of the land carbon cycle model.

tracers. The units of the SMS terms are ($\text{mol m}^{-3}\text{s}^{-1}$).

$$\begin{aligned}
 SMS(P) &= J(I, NO_3, PO_4)P - \varphi_P P - \varphi_{PP} P^2 - G(P)Z \\
 SMS(Z) &= f_a G(P)Z - \varphi_Z Z - \varphi_{ZZ} Z^2 \\
 SMS(D) &= (1 - f_a)G(P)Z + \varphi_{PP} P^2 + \varphi_{ZZ} Z^2 - \varphi_D D - w_D \frac{\partial D}{\partial z} \\
 SMS(NO_3) &= \varphi_P P + \varphi_Z Z + \varphi_D D - J(I, NO_3, PO_4)P \\
 SMS(PO_4) &= SMS(NO_3) \cdot R_{pn} \\
 SMS(O_2) &= -SMS(PO_4) \cdot R_{on} \cdot R_{np}
 \end{aligned} \tag{8.5-8.10}$$

Here, the grazing function $G(P)$ is $g\epsilon P^2 / (g + \epsilon P^2)$. Other variables and their values are listed in Table 4.

The growth rate of phytoplankton $J(I, NO_3, PO_4)$ is limited by either light or and nutrient levels. For the nutrient limitation, we adopt optimal uptake kinetics, which assumes a physiological trade-off between the efficiency of nutrient encounters at the cell surface and the maximum assimilation rate (Smith et al., 2009).

$$J_I = \frac{J_{\max} \alpha I}{[J_{\max}^2 + (\alpha I)^2]^{1/2}} \tag{8.12}$$

$$I = I_{z=0} PAR \exp(-k_w \tilde{z} - k_e \int_0^{\tilde{z}} P dz) \tag{8.13}$$

$$J_{\max} = a \cdot b^{cT} \tag{8.14}$$

$$J_N = \frac{V_o N}{N + 2\sqrt{\alpha_{OU} N} + \alpha_{OU}} \quad (N = NO_3 \text{ or } PO_4) \tag{8.15}$$

$$V_o = 0.5 \left(1 + \sqrt{\frac{\alpha_{OU}}{K_N}}\right) \tag{8.16}$$

Here, $\tilde{z} = z/\cos\theta = z / (\sin 2\theta / 1.33^2)^{1/2}$ is the effective vertical coordinate for a refraction index of 1.33 according to

Snell's law relating the zenith angle of incidence in air (θ) to the angle of incidence in water.

Formulations for the production of DIC and Alk are based on Schmittner et al. (2008, 2009).

Production changes in inorganic nutrients and calcium carbonate (CaCO_3), in molar numbers, are

Table 4 Notations and their values in the terrestrial carbon cycle model

notation	description	units	value
α	Initial slope of P-I curve	$(W m^{-2})^{-1} day^{-1}$	0.1d0
a	Maximum growth rate parameter	day^{-1}	0.2d0
b	Maximum growth rate = ab^{cT}		1.066d0
c			1.d0
PAR	Photosynthetically active radiation		0.43d0
k_e	Light attenuation due to phytoplankton	$m^{-1} (mol m^{-3})^{-1}$	0.03d3
k_w	Light attenuation in the water	m^{-1}	0.04d0
k_{NO_3}	Half-saturation constant for NO_3 uptake	$mol m^{-3}$	0.7d-3
k_{PO_4}	Half-saturation constant for PO_4 uptake	$mol m^{-3}$	0.d0
α_{OU}	Fitting constant for Optical Uptake kinetics		0.19d0
g	Maximum grazing rate	day^{-1}	1.575d0
ε	Prey capture rate	$(mol m^{-3})^{-2} day^{-1}$	1.6d6
ϕ_P	Specific mortality/recycling rate	s^{-1}	0.014d0
ϕ_{PP}	Quadratic mortality rate	$(mol m^{-3})^{-1} day^{-1}$	0.05d3
f_a	Assimilation efficiency		0.925d0
ϕ_{ZZ}	Quadratic mortality of zooplankton	$(mol m^{-3})^{-1} day^{-1}$	0.34d3
ϕ_Z	Excretion	day^{-1}	0.01d0
ϕ_D	Remineralization rate	day^{-1}	0.048d0
w_D	Sinking velocity	$m day^{-1}$	2.d0
$R_{C/N}$	Molar elemental ratio (C/N)		7.d0
$R_{O/N}$	Molar elemental ratio (O ₂ /N)		10.d0
$R_{N/P}$	Molar elemental ratio (N/P)		16.d0
$R_{CaCO_3/poc}$	$CaCO_3$ over nonphotosynthetic POC production ratio		0.05d0
D_{CaCO_3}	$CaCO_3$ remineralization e-folding depth	m	3500.d0

$$\begin{aligned}
 SMS(DIC) &= Sb(PO_4) \cdot R_{CP} - Sb(CaCO_3) \\
 SMS(Alk) &= -Sb(NO_3) - 2 \cdot Sb(CaCO_3) \\
 SMS(CaCO_3) &= Pr(CaCO_3) - Di(CaCO_3)
 \end{aligned}
 \tag{8.17-8.19}$$

$$Pr(CaCO_3) = ((1 - f_a)G(P)Z + \varphi_{PP}P^2 + \varphi_{ZZ}Z^2) \cdot R_{CaCO_3/POC} \cdot R_{CN} \tag{8.20}$$

$$Di(CaCO_3) = \int Pr(CaCO_3) dz \cdot \frac{d}{dz} (\exp(-z/D_{CaCO_3})) \tag{8.21}$$

Formulations of air-sea gas exchange and carbon chemistry follow protocols of the Ocean Carbon-Cycle Model Intercomparison Project (Orr et al., 1999).

9. Coupler (Scup)

The simple Scup coupler was developed at MRI as a general-purpose coupler for coupling component models for integration into an ESM. Each component model in MRI-ESM1, the atmospheric model, ocean-ice model, aerosol model, and atmospheric chemistry model, uses Scup to exchange data with the other component models. Scup makes it easy to develop an integrated model composed of an arbitrary combination of these component models.

Scup has several excellent features (see Yoshimura and Yukimoto, 2008, for more details).

- High-speed data transfer is possible owing to direct communication between the parallelized component model processes via Scup.
- Different coordinates and grids can be used for each coupled component model, since Scup supports 2-dimensional and 3-dimensional grid transformation with good conservation accuracy.
- Component models to be coupled, variables to be exchanged, and the timing of the data exchange can be flexibly changed by modifying the settings of the configuration file 'Scup Namelist'.
- All Scup subroutines are coded with Fortran95, so the Scup library can be compiled on any platform that has a Fortran95 compiler and an MPI library.

As shown in Fig. 15, distributing the communications reduces the amount of transferred data and leads to high computational efficiency. Using the settings in the Scup Namelist configuration file, the models can be executed in parallel or sequentially (Fig. 16); accordingly, we can distribute the execution of the component models in the most efficient way on the computer being used.

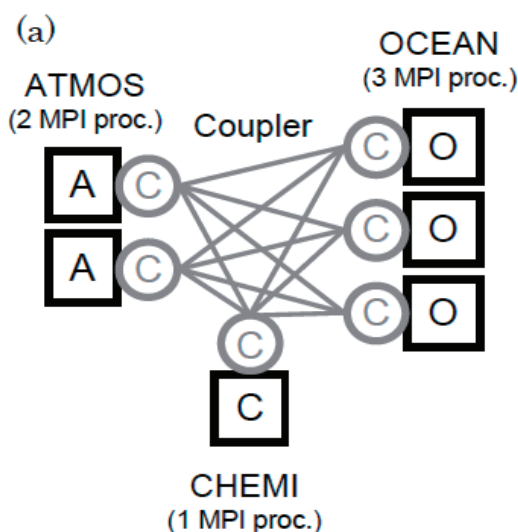


Figure 15 Schematic diagram of communication with Scup among three component models (ATMOS, OCEAN, and CHEMI).

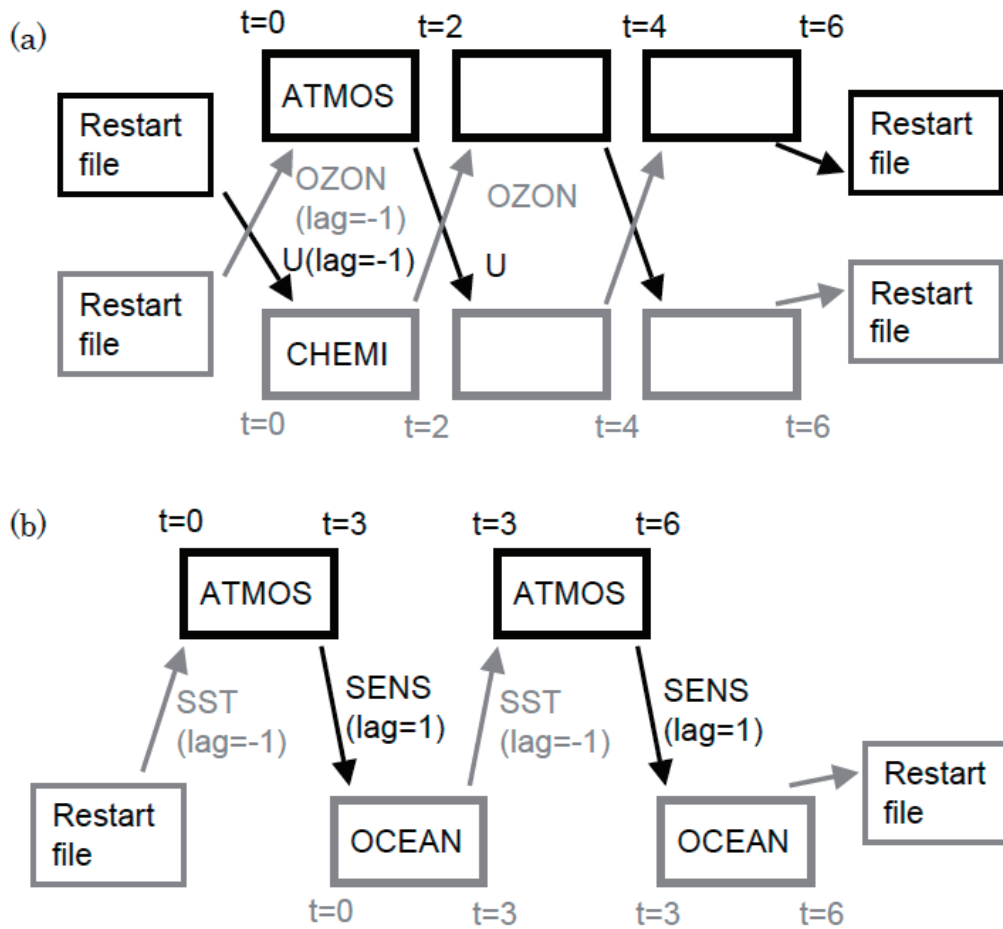


Figure 16 Schematic diagrams for patterns of model coupling. (a) Concurrent coupling, where two component models are executed concurrently. (b) Sequential coupling, where two component models are executed sequentially and alternatively at given time intervals.

References

- Abdul-Razzak, H., and S. J. Ghan, 2000: A parameterization of aerosol activation: 2. Multiple aerosol type, *J. Geophys. Res.*, **105**, 6837–6844.
- Abdul-Razzak, H., and S. J. Ghan, 2002: A parameterization of aerosol activation 3. Sectional representation. *J. Geophys. Res.*, **107 (D3)**, 4026, doi:10.1029/2001JD000483
- Albrecht, B. A., 1989: Aerosols, cloud microphysics, and fractional cloudiness. *Science*, **245**, 1227–1230.
- Andres, R. J. and A. D. Kasgnoc, 1998: A time-averaged inventory of subaerial volcanic sulfur emissions. *J. Geophys. Res.* **103**, 25251–25261.
- Aoki, T, A. Hachikubo and M. Hori, 2003: Effects of snow physical parameters on shortwave broadband albedos. *J. Geophys. Res.*, **108 (D19)**, 4616, doi: 10.1029/2003JD003506.
- Aoki, T., and Y. T. Tanaka, 2008: Influence of atmospheric aerosol deposition on snow albedo. *Tenki* (in Japanese), **55**, 538-547.
- Arakawa, A., and M.-D. Cheng, 1993: The Arakawa–Schubert cumulus parameterization. The Representation of Cumulus Convection in Numerical Models, *Meteor. Monogr.*, No. 46, Amer. Meteor. Soc., 123–136.
- Arakawa, A., and W. H. Schubert, 1974: Interaction of a cumulus cloud ensemble with the large-scale environment. Part I. *J. Atmos. Sci.*, **31**, 674–701.
- Arking, A. A. and K. Grossman, 1972 : The influence of line shape and band structure on temperatures in planetary atmospheres. *J. Atmos. Sci.*, **29**, 937–949.
- Bechtold P., E. Bazile, F. Guichard, P. Mascart, and E. Richard, 2001: A mass-flux convection scheme for regional and global models. *Quart. J. Roy. Meteor. Soc.*, **127**, 869–886.
- Bigg, E.K., 1953: The supercooling of water. *Proc. Phys. Soc. London*, **B66**, 688-694.
- Bony, S, and J.-L. Dufresne, 2005: Marine boundary layer clouds at the heart of tropical cloud feedback uncertainties in climate models. *Geophys. Res. Lett.*, **32**, L20806, doi:10.1029/2005GL023851.
- Briegleb, B. P., 1992 : Delta-Eddington approximation for solar radiation in the NCAR Community Climate Model. *J. Geophys. Res.*, **97**, 7603-7612.
- Castro S. L., G. A. Wick, and W. J. Emery, 2003: Further refinements to models for the bulk-skin sea surface temperature difference. *J. Geophys. Res.*, **108**, 3377, doi:10.1029/2002JC001641.
- Cheng M.-D., and A. Arakawa, 1997: Inclusion of rainwater budget and convective downdrafts in the Arakawa–Schubert cumulus parameterization. *J. Atmos. Sci.*, **54**, 1359–1378.
- Chin, M., P. Ginoux, S. Kinne, O. Torres, B. N. Holben, B. N. Duncan, R. V. Martin, J. A. Logan, A.

- Higurashi, and T. Nakajima, 2002: Tropospheric aerosol optical thickness from the GOCART model and comparisons with satellite and sun photometer measurements. *J. Atmos. Sci.*, **59**, 461–483.
- Chou, M. D. and L. Kouvaris, 1991 : Calculations of transmission functions in the IR CO₂ and O₃ bands. *J. Geophys. Res.*, **96**, 9003-9012.
- Clough, S. A., M. J. Iacono, and J.-L. Moncet, 1992 : Line-by-line calculations of atmospheric fluxes and cooling rates: Application to water vapor. *J. Geophys. Res.*, **97**, 15761–15785.
- Clough, S. A., F. X. Kneizys, and R. W. Davies, 1989 : Line shape and the water vapor continuum. *Atmos. Res.*, **23**, 229–241.
- Cooke, W. F., C. Liou, H. Cachier and J. Feichter, 1999: Construction of a 1° × 1° fossil fuel emission data set for carbonaceous aerosol and implementation and radiative impact in the ECHAM4 model. *J. Geophys. Res.*, **104**, 22137–22162.
- Cox, M. D. 1987: Isopycnal diffusion in a z-coordinate ocean model. *Ocean Modelling*, **74**, 1-5.
- Deushi, M., and K. Shibata, 2010: Development of an MRI Chemistry-Climate Model ver. 2 for the Study of Tropospheric and Stratospheric Chemistry. *submitted to Pap. Meteor. Geophys.*
- Ebert, E. E., and J. A. Curry, 1992 : A parameterization of ice cloud optical properties for climate models, *J. Geophys. Res.*, **97**, 3831-3836.
- European Centre for Medium-Range Weather Forecasts, 2004: IFS Documentation CY28r1, <http://www.ecmwf.int/research/ifsdocs/CY28r1>. Part IV, Chapter 6.
- Farquhar, G. D., S. von Caemmerer, and J. A. Berry, 1980: A biochemical model of photosynthetic CO₂ assimilation in leaves of C₃ species. *Planta*, **149**, 78-90.
- Fécan, F., B. Marticorena and G. Bergametti, 1999: Parameterization of the increase of the aeolian erosion threshold wind friction velocity due to soil moisture for arid and semi-arid areas. *Annales Geophysicae*, **17**, 149–157.
- Freidenreich, S. M. and V. Ramaswamy, 1999: A new multiple-band solar Radiative parameterization for general circulation models. *J. Geophys. Res.*, **104**, 31389–31409.
- Friedlingstein, P., and coauthors, 2006: Climate-carbon cycle feedback analysis: results from the C4MIP model intercomparison. *J. Climate*, **19**, 3337-3353.
- Geleyn, J.-F. and A. Hollingsworth, 1979 : An economical analytical method for the computation of the interaction between scattering and line absorption of radiation. *Beitr. Phys. Atmos.*, **52**, 1–16.
- Gent P. R., and J. C. McWilliams, 1990: Isopycnal mixing in ocean circulation models. *J. Phys. Oceanogr.*, **20**, 150-155.
- Gentemann, C., C. J. Donlon, A. Stuart-Menteth, and F. J. Wentz, 2003: Diurnal signals in satellite sea surface temperature measurements, *Geophys. Res. Lett.*, **30(3)**, 1140, doi:10.1029/2002GL016291.

- Giorgi, F. and W. L. Chameides, 1986: Rainout lifetimes of highly soluble aerosols and gases as inferred from simulations with a general circulation model. *J. Geophys. Res.*, **91**, 14367–14376.
- Gong, S. L., 2003: A parameterization of sea-salt aerosol source function for sub- and super-micron particles. *Global Biogeochem. Cycles*, **17**, 1097, doi:10.1029/2003GB002079.
- Gong, S. L., L. A. Barrie and J.-P. Blanchet, 1997: Modeling sea-salt aerosols in the atmosphere 1. model development. *J. Geophys. Res.*, **102**, 3805–3818.
- Gravel, S. and A. Staniforth, 1994: A mass-conserving semi-Lagrangian scheme for the shallow-water equations, *Mon. Wea. Rev.*, **122**, 243-248.
- Gregory, D., Kershaw, R., and Inness, P. M., 1997: Parametrization of momentum transport by convection. II: Tests in single-column and general circulation models. *Quart. J. Roy. Meteor. Soc.*, **123**, 1153-1183.
- Greve, R., 1997: A continuum-mechanical formulation for shallow polythermal ice sheets. *Philosophical Transactions of the Royal Society London A* , **355 (1726)**, 921-974.
- Guenther, A., C. N. Hewitt, D. Erickson, R. Fall, C. Geron, T. Graedel, P. Harley, L. Klinger, M. Lerdau, W. A. Mckay, T. Pierce, B. Scholes, R. Steinbrecher, R. Tallamraju, J. Taylor, and P. Zimmerman, 1995: A global model of natural volatile organic compound emissions. *J. Geophys. Res.*, **100(D5)**, 8873–8892, doi:10.1029/94JD02950.
- Hansen, J. and L. Nazarenko, 2004: Soot climate forcing via snow and ice albedos. *Proc. Natl. Acad. Sci. USA*, **101**, 423–428, doi:10.1073/pnas.2237157100.
- Hansen, J., M. Sato, and R. Ruedy, 1997: Radiative forcing and climate response, *J. Geophys. Res.*, **102 (D6)**, 6831–6864.
- Hara, T., 2007a: Update of the operational JMA mesoscale model and implementation of improved Mellor-Yamada level 3 scheme. *Extended Abstracts, 22nd Conf. on Weather Analysis and Forecasting/18th Conf. on Numerical Weather Prediction*, Utah, USA, J3.5
- Hara, T., 2007b: Implementation of improved Mellor-Yamada Level 3 scheme and partial condensation scheme to JMANHM and their performance. *CAS/JSC WGNE Res. Act. in Atmos. and Ocea. Modelling*, **37**, 0407-0408.
- Hasumi, H, 2006: CCSR Ocean Component Model (COCO) Version 4.0. Center for Climate System Research, *CCSR report*, No. 25.
- Haxeltine, A., and I. C. Prentice, 1996: BIOME3: An equilibrium terrestrial biosphere model based on ecophysiological constraints, resource availability, and competition among plant functional types. *Global Biogeochem. Cycles*, **10**, 693-709.
- Hess, M., P. Koepke, and I. Schult, 1998 : Optical properties of aerosols and clouds: The software package OPAC. *Amer. Meteor. Soc.*, **79**, 831-843.

- Hibler, W. D., III, 1979: A dynamic thermodynamic sea ice model. *J. Phys. Oceanogr.*, **9**, 815-846.
- Hines, C. O., 1997: Doppler-spread parameterization of gravity-wave momentum deposition in the middle atmosphere. Part 1: Basic formulation. *J. Atmos. Solar-Terr. Phys.*, **59**, 371-386
- Hirai, M., T. Sakashita, H. Kitagawa, T. Tsuyuki, M. Hosaka and M. Oh'izumi, 2007: Development and validation of a new land surface model for JMA's operational global model using the CEOP observation dataset. *J. Meteor. Soc. Japan*, **85A**, 1-24.
- Hofmann, M., and M. A. M. Maqueda, 2006: Performance of a second-order moments advection scheme in an Ocean General Circulation Model. *J. Geophys. Res.*, **111**, C05006.
- Holtslag, A., and B. Boville, 1993: Local Versus Nonlocal Boundary-Layer Diffusion in a Global Climate Model. *J. Climate*, **6**, 1825-1842.
- Hortal, M., 2002: The development and testing of a new two-time-level semi-Lagrangian scheme (SETTLS) in the ECMWF forecast model. *Quart. J. Roy. Meteor. Soc.*, **128**, 1671-1687.
- Hu, Y. X., and K. Stamnes. 1993 : An accurate parameterization of the radiative properties of water clouds suitable for use in climate models. *J. Climate*, **6**, 728-742.
- Hunke, E. C., and J. K. Dukowicz, 2002: The elastic-viscous-plastic sea ice dynamics model in general orthogonal curvilinear coordinates on a sphere-incorporation of metric terms. *Mon. Wea. Rev.*, **130**, 1848-1865.
- Hunke, E. C., and W. H. Lipscomb, 2001: CICE: The Los Alamos Sea Ice Model documentation and software, version 3. *Los Alamos National Laboratory Tech. Rep.* LA-CC-98-16 v. 3, Los Alamos, NM, 52 pp.
- Hunke, E. C, and W. H. Lipscomb, 2006: CICE: the Los Alamos Sea Ice Model Documentation and Software User's Manual, 59pp.
(Available at <http://climate.lanl.gov/source/projects/climate/Models/CICE/index.shtml>.)
- IPCC, 1996: Climate Change 1995: The Science of Climate Change, Contribution of Working Group I to the Second Assessment Report of the Intergovernmental Panel on Climate Change, (Eds. Houghton, J.T., L.G. Meira Filho, B.A. Callander, N. Harris, A. Kattenberg, and K. Maskell), Cambridge University Press, Cambridge, United Kingdom and New York, NY, USA, 572pp.
- IPCC, 2001: Climate Change 2001: The Scientific Basis. Intergovernmental Panel on Climate Change, Contribution of Working Group I to the Third Assessment Report of the Intergovernmental Panel on Climate Change, (Eds. Houghton, J.T., Y. Ding, D.J. Griggs, M. Noguer, P.J. van der Linden, X. Dai, K. Maskell, and C.A. Johnson), Cambridge University Press, Cambridge, United Kingdom and New York, NY, USA, 881pp.
- IPCC, 2007: Climate Change 2007: The Physical Science Basis. Contribution of Working Group I to the Fourth Assessment Report of the Intergovernmental Panel on Climate Change. (Eds. Solomon, S., D. Qin, M. Manning, Z. Chen, M. Marquis, K.B. Averyt, M. Tignor and H.L. Miller), Cambridge University Press, Cambridge, United Kingdom and New York, NY, USA, 996pp.

- Ishizaki, H., and T. Motoi, 1999: Reevaluation of the Takano-Onishi scheme for momentum advection on bottom relief in ocean models. *J. Atmos. Oceanic. Technol.*, **16**, 1994-2010.
- Iwasaki, T., S. Yamada, and K. Tada, 1989: A parameterization scheme of orographic gravity wave drag with the different vertical partitioning, part 1: Impact on medium range forecast. *J. Meteor. Soc. Japan*, **67**, 11-41.
- Jakob, C., 2000: The representation of cloud cover in Atmospheric General Circulation Models, *A thesis submitted to the Fakultat fur Physik der Ludwig-Maximilians-Universitat*, ECMWF.
- JMA, 2002: Outline of the operational numerical weather prediction at the Japan Meteorological Agency (Appendix to WMO numerical weather prediction progress report). Japan Meteorological Agency, 157pp.
- Joseph, J. H., W. J. Wiscombe, and J. A. Weinman, 1976 : The Delta-Eddington approximation for radiative flux transfer. *J. Atmos. Sci.*, **33**, 2452-2459.
- Kain, J. S., 2004: The Kain–Fritsch convective parameterization: An update. *J. Appl. Meteor.*, **43**, 170–181.
- Kain, J. S., and J. M. Fritsch, 1990: A one-dimensional entraining/detraining plume model and its application in convective parameterization. *J. Atmos. Sci.*, **47**, 2784-2802.
- Kain, J. S., and J. M. Fritsch, 1993: Convective parameterization for mesoscale models: The Kain–Fritsch scheme. The Representation of Cumulus Convection in Numerical Models, *Meteor. Monogr.*, No. 46, Amer. Meteor. Soc., 165–170.
- Kärcher, B., J. Hendricks, U. Lohmann, 2006: Physically based parameterization of cirrus cloud formation for use in global atmospheric models. *J. Geophys. Res.*, **111**, D01205, doi: 10.1029/2005JD006219.
- Kawai, Y., and A. Wada, 2007: Diurnal Sea Surface Temperature Variation and Its Impact on the Atmosphere and Ocean: A Review. *J. Oceanogr.*, **63**, 721-744.
- Kessler, E., 1969: On the distribution and continuity of water substance in atmospheric circulation. *Meteor. Monogr.*, Amer. Meteor. Soc., **32**, 84 pp.
- Kettle, A. J., M. O. Andreae, D. Amouroux, T. W. Andreae, T. S. Bates, H. Berresheim, H. Bingemer, R. Boniforti, M. A. J. Curran, G. R. DiTullio, G. Helas, G. B. Jones, M. D. Keller, R. P. Kiene, C. Leck, M. Lévassieur, G. Malin, M. Maspero, P. Matrai, A. R. McTaggart, N. Mihalopoulos, B. C. Nguyen, A. Novo, J. P. Putaud, S. Rapsomanikis, G. Roberts, G. Schebeske, S. Sharma, R. Sim, R. Staubes, S. Turner and G. Uher, 1999: A global database of sea surface dimethylsulfide (DMS) measurements and a procedure to predict sea surface DMS as a function of latitude, longitude and month. *Global Biogeochem. Cycles* **13**, 399–444.
- Kiehl, J. T. and C. S. Zender, 1995 : A Prognostic Ice Water Scheme for Anvil Clouds. World Climate Programme Research, WCRP-90, WMO/TD-No. 713, 167-188.
- Killworth, P. D., D. Stainforth, D.J. Webb, and S.M. Paterson, 1991: The development of a free-surface

Bryan-Cox-Semtner ocean model. *J. Phys. Oceanogr.*, **21**, 1333-1348.

Kitoh, A., A. Noda, Y. Nikaidou, T. Ose, and T. Tokioka, 1995: AMIP simulations of the MRI GCM. *Pap. Meteor. Geophys.*, **45**, 121-148.

Koster, R. D. and M. J. Suarez, et al., 1996: The influence of land surface moisture retention on precipitation statistics. *J. Climate*, **5**, 1379-1390.

Kusunoki, S., J. Yoshimura, H. Yoshimura, A. Noda, K. Oouchi and R. Mizuta, 2006: Change of Baiu rain band in global warming projection by an atmospheric general circulation model with a 20-km grid size. *J. Meteor. Soc. Japan*, **84**, 581-611.

Lacis, A. A., and J. E. Hansen, 1974 : A parameterization for the absorption of solar radiation in the earth's atmosphere. *J. Atmos. Sci.*, **31**, 118-133.

Liss, P. S. and L. Merlivat, 1986: Air-sea exchange rates : Introduction and synthesis. P. Buat-Ménard (Ed.), *The Role of Air-Sea Exchange in Geochemical Cycling*, Vol. C 185 of NATO ASI Series, D. Reidel Publishing Company, 113-127.

Liu, Y., P. H. Daum, and S. S. Yum, 2006 : Analytical expression for the relative dispersion of the cloud droplet size distribution, *Geophys. Res. Lett.*, **33**, L02810, doi:10.1029/2005GL024052.

Logan, J. A., 1999: An analysis of ozonesonde data for the troposphere: Recommendations for testing 3-D models and development of a gridded climatology for tropospheric ozone. *J. Geophys. Res.*, **104**, 16,115-16,149,

Lohmann, U., 2002 : Possible aerosol effects on ice clouds via contact nucleation. *J. Atmos. Sci.*, **59**, 647-656.

Lohmann, U., and K. Diehl, 2006: Sensitivity studies of the importance of dust ice nuclei for the indirect aerosol effect on stratiform mixed-phase clouds. *J. Atmos. Sci.*, **63**, 968-982.

Lohmann, U., P. Stier, C. Hoose, S. Ferrachat, S. Kloster, E. Roeckner, and J. Zhang, 2007: Cloud microphysics and aerosol indirect effects in the global climate model ECHAM5-HAM, *Atmos. Chem. Phys.*, **7**, 3425-3446.

Louis, J.-F., 1979: A parametric model of vertical eddy fluxes in the atmosphere. *Boundary Layer Meteor.*, **17**, 187-202.

Louis, J. F., M. Tiedtke and J.F. Geleyn, 1982: A short history of the operational PBL-parameterization at ECMWF. *Workshop on Planetary boundary layer parameterization*, ECMWF, Reading, U.K., 25-27 November 1981, 59-80.

Mellor, L. G., and L. Kantha, 1989: An ice-ocean coupled model. *J. Geophys. Res.*, **94**, 10937-10954.

Mellor, G.L., and T. Yamada, 1974: A hierarchy of turbulence closure models for planetary boundary layers. *J. Atmos. Sci.*, **31**, 1791-1806.

- Mellor, G.L. and T. Yamada, 1982: Development of a turbulence closure model for geophysical fluid problems. *Rev. Geophys. Space Phys.*, **20**, 851-875.
- Miller, M., A. Beljaars, and T. Palmer, 1992: The sensitivity of the ECMWF model to the parameterization of evaporation from the tropical oceans. *J. Climate*, **5**, 418-434.
- Mizuta, R., K. Oouchi, H. Yoshimura, A. Noda, K. Katayama, S. Yukimoto, M. Hosaka, S. Kusunoki, H. Kawai and M. Nakagawa, 2006: 20-km-mesh global climate simulations using JMA-GSM model – mean climate states –. *J. Meteor. Soc. Japan*, **84**, 165-185.
- Monahan, E. C., D. E. Spiel and K. L. Davidson, 1986: A model of marine aerosol generation via whitecaps and wave disruption. E. C. Monahan and G. M. Niocaill, Eds., *Oceanic Whitecaps*, D. Reidel, 167–174.
- Moorthi, S., and M. J. Suarez, 1992: Relaxed Arakawa-Schubert: A parameterization of moist convection for general circulation models. *Mon. Wea. Rev.*, **120**, 978–1002.
- Murakami, M., 1990: Numerical modeling of dynamical and microphysical evolution of an isolated convective cloud - the 19 July 1981 CCOPE cloud. *J. Meteor. Soc. Japan*, **68**, 107-128.
- Nagai, T., T. Tokioka, M. Endoh, Y. Kitamura, 1992: El Nino-Southern Oscillation simulated in an MRI atmosphere-ocean coupled general circulation model. *J. Climate*, **5**, 1202-1233.
- Nakanishi, M., 2001: Improvement of the Mellor-Yamada turbulence closure model based on large-eddy simulation data. *Boundary -Layer Meteorol.*, **25**, 63-88.
- Nakanishi, M. and Niino, H., 2004: An improved Mellor-Yamada level-3 model with condensation physics: Its design and verification. *Boundary -Layer Meteorol.*, **112**, 1-31.
- Nakanishi, M. and Niino, H., 2006: An improved Mellor-Yamada level-3 model: Its numerical stability and application to a regional prediction of advection fog. *Boundary -Layer Meteorol.*, **119**, 397-407.
- Nakanishi, M. and H. Nino, 2009: Development of an Improved Turbulence Closure Model for the Atmospheric Boundary Layer. *J. Meteor. Soc. Japan*, **87**, 895-912.
- Nakano, H., and N. Sugihara, 2002: Effects of bottom boundary layer parameterization on reproducing deep and bottom waters in the world ocean model. *J. Phys. Oceanogr.*, **32**, 1209-1227.
- Noh, Y., and H.-J. Kim, 1999: Simulation of temperature and turbulence structure of the oceanic boundary layer with the improved near-surface process. *J. Geophys. Res.*, **104**, 15621-15634.
- Noh, Y., Y.-J. Kang, T. Matsuura, and S. Iizuka, 2005: Effect of the Prandtl number in the parameterization of vertical mixing in an OGCM of the tropical Pacific. *Geophys. Res. Lett.*, **32**, L23609, doi:10.1029/2005GL024540.
- Noda, A., S. Yukimoto, S. Maeda, T. Uchiyama, K. Shibata, and S. Yamaki, 2001: A New Meteorological Research Institute Coupled GCM (MRI-CGCM2) –Transient Response to Greenhouse Gas and Aerosol Scenarios—. *CGER'S SUPERCOMPUTER MONOGRAPH REPORT Vol.7*, National

Institute for Environmental Studies.

- Nordeng, T. E., 1994: Extended versions of the convective parametrization scheme at ECMWF and their impact upon the mean and transient activity of the model in the tropics. *Research Department Technical Memorandum* No. 206, ECMWF.
- Numerical Prediction Division / Japan Meteorological Agency, 2007: Outline of the operational numerical weather prediction at the Japan Meteorological Agency. 194pp. [Available from JMA, 1-3-4 Otemachi, Chiyoda-ku, Tokyo 100-8122, Japan.]
- Obata, A., 2007: Climate-carbon cycle model response to freshwater discharge into the North Atlantic. *J. Climate*, **20**, 5962-5976.
- Obata, A., and Y. Kitamura, 2003: Interannual variability of the sea-air exchange of CO₂ from 1961 to 1998 simulated with a global ocean circulation-biogeochemistry model, *J. Geophys. Res.*, **108**, 3337, doi:10.1029/2001JC001088.
- Ogura, Y., and H.R. Cho, 1973: Diagnostic Determination of Cumulus Cloud Populations from Observed Large-Scale Variables. *J. Atmos. Sci.*, **30**, 1276–1286.
- Oki, T. and Y. C. Sud, 1998: Design of total runoff integrating pathways (TRIP) - a global river channel network., *Earth Interactions*, **2**, 1-37.
- Oouchi, K., J. Yoshimura, H. Yoshimura, R. Mizuta, S. Kusunoki and A. Noda, 2006: Tropical cyclone climatology in a global-warming climate as simulated in a 20km-mesh global atmospheric model: Frequency and wind intensity analyses. *J. Meteor. Soc. Japan*, **84**, 259-276.
- Orr, J., R. Najjar, C. Sabine, and F. Joos, 1999, *Abiotic-HOWTO internal OCMIP report*, LSCE/CEA Saclay 25 pp, Gif-sur-Yvette, France
- Oschlies, A., (2001), Model-derived estimates of new production: New results point toward lower values, *Deep-Sea Res. II*, **48**, 2173–2197.
- Owen, P. R., 1964: Saltation of uniform grains in air. *J. Fluid. Mech.*, **20**, 225–242.
- Pan, D.-M., and D. Randall, 1993: Implementation of the Arakawa-Schubert cumulus parameterization with a prognostic closure. *Meteor. Monogr.*, No.46, Amer.Meteor.Soc., 137-144.
- Pan, D.-M., and D. A. Randall, 1998: A cumulus parameterization with a prognostic closure. *Quart. J. Roy. Meteor. Soc.*, **124**, 949–981.
- Peng, Y., and U. Lohmann, 2003 : Sensitivity study of the spectral dispersion of the cloud droplet size distribution on the indirect aerosol effect. *Geophys. Res. Lett.*, **30**, 1507, doi:10.1029/2003GL017192.
- Penner, J. E., M. Andreae, H. Annegarn, L. Barrie, J. Feichter, D. Hegg, A. Jayaraman, R. Leaitch, D. Murphy, J. Nganga and G. Pitari, 2001: Aerosols: Their direct and indirect effects. J. T. Houghton, Y. Ding, D. Griggs, M. Noguier, P. J. van der Linden, X. Dai, K. Maskell and C. A. Johnson, Eds., *Climate Change 2001: The Scientific Basis*, Contribution of Working Group I to the Third

Assessment Report of the Intergovernmental Panel on Climate Change, Cambridge Univ. Press., New York, chapter 5, 289–348.

- Prather, M. J., 1986: Numerical advection by conservation of second order moments. *J. Geophys. Res.*, **91**, 6671-6681.
- Prentice, I. C., and Coauthors, 2001: The carbon cycle and atmospheric carbon dioxide. *Climate Change 2001: The Scientific Basis*, J. T. Houghton et al., Eds., Cambridge University Press, 183-237.
- Priestley, A. 1993: A quasi-conservative version of the semi-Lagrangian advection scheme. *Mon. Wea. Rev.*, **121**, 621-629.
- Räisänen, P., 1998 : Effective longwave cloud fraction and maximum-random overlap of clouds: A problem and a solution. *Mon. Wea. Rev.*, **126**, 3336–3340.
- Randall, D. A., and D.-M. Pan, 1993a: Implementation of the Arakawa-Schubert cumulus parameterization with a prognostic closure. *Bull. Amer. Meteor. Soc.*, **74**, 137–144.
- Randall, D. A., and D.-M. Pan, 1993b: Implementation of the Arakawa-Schubert cumulus parameterization with a prognostic closure. *Meteorological Monograph/The representation of cumulus convection in numerical models*, **46**, 145-150.
- Redi, M. H., 1982: Oceanic isopycnal mixing by coordinate rotation. *J. Phys. Oceanogr.*, **12**, 1154-1158.
- Ritchie, H., C. Temperton, A. Simmons, M. Hortal, T. Davies, D. Dent, and M. Hamrud, 1995: Implementation of the semi-Lagrangian method in a high-resolution version of the ECMWF forecast model. *Mon. Wea. Rev.*, **123**, 489-514.
- Rothman, L. S., A. Barbe, D. C. Benner, L. R. Brown, C. Camy-Peyret, M. R. Carleer, K. Chance, C. Clerbaux, V. Dana, V. M. Devi, A. Fayt, J.-M. Flaud, R. R. Gamache, A. Goldman, D. Jacquemart, K. W. Jucks, W. J. Lafferty, J.-Y. Mandin, S. T. Massie, V. Nemtchinov, D. A. Newnham, A. Perrin, C. P. Rinsland, J. Schroeder, K. M. Smith, M. A. H. Smith, K. Tang, R. A. Toth, J. Vander Auwera, P. Varanasi, and K. Yoshino, 2003 : The HITRAN molecular spectroscopic database: edition of 2000 including updates through 2001. *J. Quant. Spectrosc. Radiat. Transfer*, **82**, 5–44.
- Rotstayn, L.D., 2000: On the “tuning”_of autoconversion parameterization. *J. Geophys. Res.*, **105** (D12) ,15495-15507.
- Rutledge, S. A. and P. V. Hobbs, 1983: The mesoscale and microscale structure and organization of clouds and precipitation in midlatitude cyclones. VIII: A model for the “seeder-feeder” process in warmfrontal rainbands. *J. Atmos. Sci.*, **40**, 1185-1206.
- Saito, K., T. Kato, H. Eito and C. Muroi, 2001: Documentation of the Meteorological Research Institute/Numerical Prediction Division unified nonhydrostatic model. *Tech. Rep. MRI*, **42**, 133 pp.
- Saito, K., T. Fujita, Y. Yamada, J. Ishida, Y. Kumagai, K. Aranami, S. Ohmori, R. Nagasawa, S. Kumagai, C. Muroi, T. Kato, H. Eito and Y. Yamazaki, 2006: The operational JMA nonhydrostatic model. *Mon. Wea. Rev.*, **134**, 1266-1298.

- Saito, K., J. Ishida, K. Aranami, T. Hara, T. Segawa, M. Narita, and Y. Honda, 2007: Nonhydrostatic atmospheric models and operational development at JMA. *J. Meteor. Soc. Japan*, **85B**, 271-304.
- Saltzman, E. S., D. B. King, K. Holmen and C. Leck, 1993: Experimental determination of the diffusion coefficient of dimethylsulfide in water. *J. Geophys. Res.* **98**, 16481–16486.
- Sasaki, H., K. Kurihara, I. Takayabu, K. Murazaki, Y. Sato, and H. Tsujino, 2006: Preliminary Results from the Coupled Atmosphere-Ocean Regional Climate Model at the Meteorological Research Institute. *J. Meteor. Soc. Japan*, **84**, 389-403.
- Sato, N., P. J. Sellers, D. A. Randall, E. K. Schneider, J. Shukla, J. L. Kinter III, Y.-T. Hou, and E. Albertazzi, 1989: Effects of implementing the simple biosphere model (SiB) in a general circulation model. *J. Atmos. Sci.*, **46**, 2657-2782.
- Schmittner, A., A. Oeschies, H. Matthews, and E. Galbraith, (2008), Future changes in climate, ocean circulation, ecosystems, and biogeochemical cycling simulated for a business-as-usual CO2 emission scenario until year 4000 AD. *Global Biogeochem. Cycles*, **22**, GB1013, doi:10.1029/2007GB002953.
- Schmittner, A., A. Oeschies, H. Matthews, and E. Galbraith, (2009), Correction to “Future changes in climate, ocean circulation, ecosystems, and biogeochemical cycling simulated for a business-as-usual CO2 emission scenario until year 4000 AD”. *Global Biogeochem. Cycles*, **23**, GB3005, doi:10.1029/2009GB003577.
- Seinfeld, J. H. and S. N. Pandis, 1997: Atmospheric chemistry and physics: From air pollution to climate change. A Wiley-Interscience publication, New York, NY, 1326pp.
- Sellers, P. J., and coauthors, 1996: A revised land surface parameterization (SiB2) for atmospheric GCMs. Part I: Model Formulation. *J. Climate*, **9**, 676-705.
- Sellers, P.J., Y. Mintz, Y.C. Sud, and A. Dalcher, 1986: A simple biosphere model (SiB) for use within general circulation models, *J. Atmos. Sci.*, **43**, 505-531.
- Shao, Y. and H. Lu, 2000: A simple expression for wind erosion threshold friction velocity. *J. Geophys. Res.*, **105**, 22437–22443.
- Shao, Y., M. R. Raupach and J. F. Leys, 1996: A model for predicting aeolian sand drift and dust entrainment on scales from paddock to region. *Aust. J. Soil. Res.*, **34**, 309–342.
- Shibata, K. and T. Aoki, 1989: An infrared radiative scheme for the numerical models of weather and climate, *J. Geophys. Res.*, **94**, 14923-14943.
- Shibata, K., M. Deushi, T. T. Sekiyama, and H. Yoshimura, 2005: Development of an MRI chemical transport model for the study of stratospheric chemistry. *Pap. Geophys. Meteorol.*, **55**, 75-119.
- Shibata, K. and A. Uchiyama, 1992: Accuracy of the delta-four-stream approximation in inhomogeneous scattering atmospheres. *J. Meteor. Soc. Japan*, **70**, 1097-1109.

- Simmons, A. J. and D. M. Burridge 1981: An energy and angular momentum conserving vertical finite difference scheme and hybrid vertical coordinates. *Mon. Wea. Rev.*, **109**, 758-766.
- Sitch, S., and coauthors, 2003: Evaluation of ecosystem dynamics, plant geography and terrestrial carbon cycling in the LPJ dynamic global vegetation model. *Global Change Biology*, **9**, 161-185.
- Slingo, A., 1989: A GCM parameterization for the shortwave radiative properties of water clouds. *J. Atmos. Sci.*, **46**, 1419-1427.
- Smagorinsky, J., 1963: General circulation experiments with the primitive equations. I. The basic experiment. *Mon. Wea. Rev.*, **91**, 99-164.
- Smith, L. and Y. Yamanaka, M. Pahlow, A. Oschlies, 2009: Optimal uptake kinetics: physiological acclimation explains the pattern of nitrate uptake by phytoplankton in the ocean, *Mar Ecol Prog Ser*, in press.
- Smith, R. N. B., 1990: A scheme for prediction layer clouds and their water content in a general circulation model. *Quart. J. Roy. Meteor. Soc.*, **116**, 435-460.
- Smith, R. D., and J. C. McWilliams, 2003: Anisotropic horizontal viscosity for ocean models. *Ocean Modelling*, **5**, 129-156.
- Smolarkiewicz, P. K., 1984: A fully multidimensional positive definite advection transport algorithm with small implicit diffusion. *J. Comput. Phys.*, **54**, 325-362.
- Sommeria, G., and J. W. Deardorff, 1977: Subgridscale condensation in models of non-precipitating clouds. *J. Atmos. Sci.*, **34**, 345-355.
- Son, S.-W., L. M. Polvani, D. W. Waugh, H. Akiyoshi, R. Garcia, D. Kinnison, S. Pawson, E. Rozanov, T. G. Shepherd, and K. Shibata, 2008: The Impact of Stratospheric Ozone Recovery on the Southern Hemisphere Westerly Jet. *Science*, **320**, 1486-1489, doi: 10.1126/science.1155939.
- St. Laurent, L., H. Simmons, and S. Jayne, 2002: Estimating tidally driven energy in the deep ocean. *Geophys. Res. Lett.*, **29**, 2106-2110.
- Takayabu, I., H. Kato, K. Nishizawa, Y. N. Takayabu, Y. Sato, H. Sasaki, K. Kurihara, and A. Kitoh, 2007: Future Projections in Precipitation over Asia Simulated by Two RCMs Nested into MRI-CGCM2.2. *J. Meteor. Soc. Japan*, **85**, 511-519.
- Takemura, T., T. Nozawa, S. Emori, T. Y. Nakajima, and T. Nakajima, 2005: Simulation of climate response to aerosol direct and indirect effects with aerosol transport-radiation model. *J. Geophys. Res.*, **110**, D02202, doi:10.1029/2004JD005029.
- Tanaka, T. Y. and Chiba, M., 2005. Global simulation of dust aerosol with a chemical transport model, MASINGAR. *J. Meteor. Soc. Japan*, **83A**, 255-278.
- Tanaka, T. Y. and M. Chiba, 2006: A numerical study of the contributions of dust source regions to the global dust budget. *Global and Planetary Changes*, **52**, 88-104, doi:10.1016/j.gloplacha.2006.02.002.

- Tanaka, T. Y., K. Orito, T. T. Sekiyama, K. Shibata, M. Chiba, H. Tanaka, 2003: MASINGAR, a global tropospheric aerosol chemical transport model coupled with MRI/JMA98 GCM: Model description. *Pap. Meteor. Geophys.*, **53(4)**, 119–138.
- Tao, W.-K., 1989: An Ice-Water Saturation Adjustment. *Mon. Wea. Rev.*, **117**, 231–235.
- Tegen, I., and I. Fung, 1995: Contribution to the atmospheric mineral aerosol load from land surface modification, *J. Geophys. Res.*, **100(D9)**, 18707–18726, doi:10.1029/95JD02051.
- Temperton, C., M. Hortal, and A. Simmons, 2001: A two-time-level semi-Lagrangian global spectral model. *Quart. J. Roy. Meteor. Soc.*, **127**, 111-127.
- Tiedtke, M., 1989: A comprehensive mass flux scheme for cumulus parameterization in large scale models. *Mon. Wea. Rev.*, **117**, 1779-1800.
- Tiedtke, M., 1993: Representation of clouds in large scale models. *Mon. Wea. Rev.*, **121**, 3040–3061.
- Tokioka, T., A. Noda, A. Kitoh, Y. Nikaidou, S. Nakagawa, T. Motoi, S. Yukimoto, and K. Takata, 1995: A transient CO₂ experiment with the MRI CGCM. *J. Meteor. Soc. Japan*, **73**, 817-826.
- Tokioka, T., K. Yamazaki, A. Kitoh and T. Ose, 1988: Equatorial 30-60 day oscillation and the Arakawa-Schubert penetrative cumulus parameterization. *J. Meteor. Soc. Japan*, **66**, 883-901.
- Tokioka, T., K. Yamazaki, I. Yagai, and A. Kitoh, 1984: A Description of the MRI Atmospheric General Circulation Model (The MRI GCM-I). *Technical Report of the Meteorological Research Institute*, **13**, 249 pp.
- Troen, I. and L. Mahrt, 1986: A simple model of the atmospheric boundary layer; sensitivity to surface evaporation. *Boundary-Layer Meteorol.*, **37**, 129-148.
- Tsujino, H., H. Hasumi, and N. Sugimoto, 2000: Deep pacific circulation controlled by vertical diffusivity at the lower thermocline depth. *J. Phys. Oceanogr.*, **30**, 2853-2865.
- Tsujino, H., T. Motoi, I. Ishikawa, M. Hirabara, H. Nakano, G. Yamanaka, T. Yasuda, and H. Ishizaki, 2010: Reference manual for the Meteorological Research Institute Community Ocean Model (MRI.COM) Version 3.). *Technical Report of the Meteorological Research Institute*, **59**, 241pp..
- Twomey, S., 1974: Pollution and the planetary albedo. *Atmos. Environ.*, **8**, 1251–1256.
- Twomey, S., 1991: Aerosols, Clouds and Radiation. *Atmos. Environ.*, **25A(11)**, 2435–2442.
- Undén, P., L. Rontu, H. Järvinen, P. Lynch, J. Calvo, G. Cats, J. Cuxart, K. Eerola, C. Fortelius, J. A. Garcia-Moya, C. Jones, G. Lenderlink, A. McDonald, R. McGrath, B. Navascues, N. W. Nielsen, V. Ødegaard, E. Rodriguez, M. Rummukainen, R. Rõõm, K. Sattler, B. H. Sass, H. Savijärvi, B. W. Schreur, R. Sigg, H. The, and A. Tijm, 2002: HIRLAM-5 Scientific Documentation, 144 pp.
- Webb, R. W., C. E. Rosenzweig and E. R. Levine, 2000: Global soil texture and derived water-holding capacities (Webb et al.). data set. Available on-line [<http://www.daac.ornl.gov>] from Oak Ridge

National Laboratory Distributed Active Archive Center, Oak Ridge, Tennessee, U.S.A.

- Woodward, F. I., T. M. Smith, and W. R. Emanuel, 1995: A global land primary productivity and phytogeography model. *Global Biogeochem. Cycles*, **9**, 471-490.
- World Meteorological Organization/United Nations Environment Programme (WMO/UNEP), 2007: Scientific Assessment of Ozone Depletion: 2006, *Global Ozone Research and Monitoring Project-Report No. 50*, Geneva.
- Wyser, K., 1998: The effective radius in ice clouds. *J. Climate*, **11**, 1793–1802.
- Xiao, F. and X. Peng, 2004: A convexity preserving scheme for conservative advection transport. *J. Comput. Phys.*, **198**, 389-402.
- Yoshimura, H. and T. Matsumura, 2003: A semi-Lagrangian scheme conservative in the vertical direction. *CAS/JSC WGNE Research Activities in Atmospheric and Ocean Modeling*, **33**, 3.19-3.20.
- Yoshimura, H. and T. Matsumura, 2005: A two-time-level vertically-conservative semi-Lagrangian semi-implicit double Fourier series AGCM. *CAS/JSC WGNE Research Activities in Atmospheric and Ocean Modeling*, **35**, 3.25-3.26.
- Yoshimura, H. and S. Yukimoto, 2008: Development of a Simple Coupler (Scup) for Earth System Modeling. *Pap. Meteor. Geophys.*, **59**, 19-29.
- Yukimoto, S., and Y. Kitamura, 2003: An investigation of the irregularity of El Niño in a coupled GCM. *J. Meteor. Soc. Japan*, **81**, 599-622.
- Yukimoto, S., A. Noda, A. Kitoh, M. Sugi, Y. Kitamura, M. Hosaka, K. Shibata, S. Maeda, and T. Uchiyama, 2001: A new Meteorological Research Institute Coupled GCM (MRI-CGCM2) — Model climate and its variability —. *Pap. Meteor. Geophys.*, **51**, 47-88, doi:10. 2467/mripapers.51.47.
- Yukimoto, S., A. Noda, A. Kitoh, M. Hosaka, H. Yoshimura, T. Uchiyama, K. Shibata, O. Arakawa, and S. Kusunoki, 2006: Present-day climate and climate sensitivity in the Meteorological Research Institute Coupled GCM version 2.3 (MRI-CGCM2.3). *J. Meteor. Soc. Japan*, **84**, 333-363.
- Zhong, W. and J. D. Haigh, 1995 : Improved broadband emissivity parameterization for water vapor cooling rate calculations. *J. Atmos. Sci.*, **52**, 124–138.
- Zobler, L., 1986: A world soil file for global climate modeling. *NASA Tech. Memo.*, 87802, NASA, 33pp.

気象研究所技術報告一覧表

- 第1号 バックグラウンド大気汚染の測定法の開発 (地球規模大気汚染特別研究班, 1978)
Development of Monitoring Techniques for Global Background Air Pollution. (MRI Special Research Group on Global Atmospheric Pollution, 1978)
- 第2号 主要活火山の地殻変動並びに地熱状態の調査研究 (地震火山研究部, 1979)
Investigation of Ground Movement and Geothermal State of Main Active Volcanoes in Japan. (Seismology and Volcanology Research Division, 1979)
- 第3号 筑波研究学園都市に新設された気象観測用鉄塔施設 (花房龍男・藤谷徳之助・伴野 登・魚津 博, 1979)
On the Meteorological Tower and Its Observational System at Tsukuba Science City. (T. Hanafusa, T. Fujitani, N. Banno, and H. Uozu, 1979)
- 第4号 海底地震常時観測システムの開発 (地震火山研究部, 1980)
Permanent Ocean-Bottom Seismograph Observation System. (Seismology and Volcanology Research Division, 1980)
- 第5号 本州南方海域水温図-400m (又は 500m) 深と 1,000m 深- (1934-1943 年及び 1954-1980 年) (海洋研究部, 1981)
Horizontal Distribution of Temperature in 400m (or 500m) and 1,000m Depth in Sea South of Honshu, Japan and Western-North Pacific Ocean from 1934 to 1943 and from 1954 to 1980. (Oceanographical Research Division, 1981)
- 第6号 成層圏オゾンの破壊につながる大気成分及び紫外日射の観測 (高層物理研究部, 1982)
Observations of the Atmospheric Constituents Related to the Stratospheric ozone Depletion and the Ultraviolet Radiation. (Upper Atmosphere Physics Research Division, 1982)
- 第7号 83 型強震計の開発 (地震火山研究部, 1983)
Strong-Motion Seismograph Model 83 for the Japan Meteorological Agency Network. (Seismology and Volcanology Research Division, 1983)
- 第8号 大気中における雪片の融解現象に関する研究 (物理気象研究部, 1984)
The Study of Melting of Snowflakes in the Atmosphere. (Physical Meteorology Research Division, 1984)
- 第9号 御前崎南方沖における海底水圧観測 (地震火山研究部・海洋研究部, 1984)
Bottom Pressure Observation South off Omaezaki, Central Honsyu. (Seismology and Volcanology Research Division and Oceanographical Research Division, 1984)
- 第10号 日本付近の低気圧の統計 (予報研究部, 1984)
Statistics on Cyclones around Japan. (Forecast Research Division, 1984)
- 第11号 局地風と大気汚染質の輸送に関する研究 (応用気象研究部, 1984)
Observations and Numerical Experiments on Local Circulation and Medium-Range Transport of Air Pollutions. (Applied Meteorology Research Division, 1984)
- 第12号 火山活動監視手法に関する研究 (地震火山研究部, 1984)
Investigation on the Techniques for Volcanic Activity Surveillance. (Seismology and Volcanology Research Division, 1984)
- 第13号 気象研究所大気大循環モデル-I (MRI・GCM-I) (予報研究部, 1984)
A Description of the MRI Atmospheric General Circulation Model (The MRI・GCM-I). (Forecast Research Division, 1984)
- 第14号 台風の構造の変化と移動に関する研究-台風 7916 の一生- (台風研究部, 1985)
A Study on the Changes of the Three-Dimensional Structure and the Movement Speed of the Typhoon through its Life Time. (Typhoon Research Division, 1985)
- 第15号 波浪推算モデル MRI と MRI-II の相互比較研究-計算結果図集- (海洋気象研究部, 1985)
An Intercomparison Study between the Wave Models MRI and MRI-II - A Compilation of Results - (Oceanographical Research Division, 1985)
- 第16号 地震予知に関する実験的及び理論的研究 (地震火山研究部, 1985)
Study on Earthquake Prediction by Geophysical Method. (Seismology and Volcanology Research Division, 1985)
- 第17号 北半球地上月平均気温偏差図 (予報研究部, 1986)
Maps of Monthly Mean Surface Temperature Anomalies over the Northern Hemisphere for 1891-1981. (Forecast Research Division, 1986)
- 第18号 中層大気の研究 (高層物理研究部・気象衛星研究部・予報研究部・地磁気観測所, 1986)
Studies of the Middle Atmosphere. (Upper Atmosphere Physics Research Division, Meteorological Satellite Research Division, Forecast Research Division, MRI and the Magnetic Observatory, 1986)
- 第19号 ドップラーレーダによる気象・海象の研究 (気象衛星研究部・台風研究部・予報研究部・応用気象研究部・海洋研究部, 1986)
Studies on Meteorological and Sea Surface Phenomena by Doppler Radar. (Meteorological Satellite Research Division, Typhoon Research Division, Forecast Research Division, Applied Meteorology Research Division, and Oceanographical Research Division, 1986)
- 第20号 気象研究所対流圏大気大循環モデル (MRI・GCM-I) による 12 年間分の積分 (予報研究部, 1986)
Mean Statistics of the Tropospheric MRI・GCM-I based on 12-year Integration. (Forecast Research Division, 1986)

- 第 21 号 宇宙線中間子強度 1983-1986 (高層物理研究部, 1987)
Multi-Directional Cosmic Ray Meson Intensity 1983-1986. (Upper Atmosphere Physics Research Division, 1987)
- 第 22 号 静止気象衛星「ひまわり」画像の噴火噴煙データに基づく噴火活動の解析に関する研究 (地震火山研究部, 1987)
Study on Analysis of Volcanic Eruptions based on Eruption Cloud Image Data obtained by the Geostationary Meteorological satellite (GMS). (Seismology and Volcanology Research Division, 1987)
- 第 23 号 オホーツク海海洋気候図 (篠原吉雄・四電信行, 1988)
Marine Climatological Atlas of the sea of Okhotsk. (Y. Shinohara and N. Shikama, 1988)
- 第 24 号 海洋大循環モデルを用いた風の応力異常に対する太平洋の応答実験 (海洋研究部, 1989)
Response Experiment of Pacific Ocean to Anomalous Wind Stress with Ocean General Circulation Model. (Oceanographical Research Division, 1989)
- 第 25 号 太平洋における海洋諸要素の季節平均分布 (海洋研究部, 1989)
Seasonal Mean Distribution of Sea Properties in the Pacific. (Oceanographical Research Division, 1989)
- 第 26 号 地震前兆現象のデータベース (地震火山研究部, 1990)
Database of Earthquake Precursors. (Seismology and Volcanology Research Division, 1990)
- 第 27 号 沖縄地方における梅雨期の降水システムの特徴 (台風研究部, 1991)
Characteristics of Precipitation Systems During the Baiu Season in the Okinawa Area. (Typhoon Research Division, 1991)
- 第 28 号 気象研究所・予報研究部で開発された非静水圧モデル (猪川元興・斉藤和雄, 1991)
Description of a Nonhydrostatic Model Developed at the Forecast Research Department of the MRI. (M. Ikawa and K. Saito, 1991)
- 第 29 号 雲の放射過程に関する総合的研究 (気候研究部・物理気象研究部・応用気象研究部・気象衛星・観測システム研究部・台風研究部, 1992)
A Synthetic Study on Cloud-Radiation Processes. (Climate Research Department, Physical Meteorology Research Department, Applied Meteorology Research Department, Meteorological Satellite and Observation System Research Department, and Typhoon Research Department, 1992)
- 第 30 号 大気と海洋・地表とのエネルギー交換過程に関する研究 (三上正男・遠藤昌宏・新野 宏・山崎孝治, 1992)
Studies of Energy Exchange Processes between the Ocean-Ground Surface and Atmosphere. (M. Mikami, M. Endoh, H. Niino, and K. Yamazaki, 1992)
- 第 31 号 降水日の出現頻度からみた日本の季節推移-30年間の日降水量資料に基づく統計- (秋山孝子, 1993)
Seasonal Transition in Japan, as Revealed by Appearance Frequency of Precipitating-Days. - Statistics of Daily Precipitation Data During 30 Years - (T. Akiyama, 1993)
- 第 32 号 直下型地震予知に関する観測的研究 (地震火山研究部, 1994)
Observational Study on the Prediction of Disastrous Intraplate Earthquakes. (Seismology and Volcanology Research Department, 1994)
- 第 33 号 各種気象観測機器による比較観測 (気象衛星・観測システム研究部, 1994)
Intercomparisons of Meteorological Observation Instruments. (Meteorological Satellite and Observation System Research Department, 1994)
- 第 34 号 硫黄酸化物の長距離輸送モデルと東アジア地域への適用 (応用気象研究部, 1995)
The Long-Range Transport Model of Sulfur Oxides and Its Application to the East Asian Region. (Applied Meteorology Research Department, 1995)
- 第 35 号 ウインドプロファイラーによる気象の観測法の研究 (気象衛星・観測システム研究部, 1995)
Studies on Wind Profiler Techniques for the Measurements of Winds. (Meteorological Satellite and Observation System Research Department, 1995)
- 第 36 号 降水・落下塵中の人工放射性核種の分析及びその地球化学的研究 (地球化学研究部, 1996)
Geochemical Studies and Analytical Methods of Anthropogenic Radionuclides in Fallout Samples. (Geochemical Research Department, 1996)
- 第 37 号 大気と海洋の地球化学的研究 (1995年及び1996年) (地球化学研究部, 1998)
Geochemical Study of the Atmosphere and Ocean in 1995 and 1996. (Geochemical Research Department, 1998)
- 第 38 号 鉛直 2 次元非線形問題 (金久博忠, 1999)
Vertically 2-dimensional Nonlinear Problem (H. Kanehisa, 1999)
- 第 39 号 客観的予報技術の研究 (予報研究部, 2000)
Study on the Objective Forecasting Techniques (Forecast Research Department, 2000)
- 第 40 号 南関東地域における応力場と地震活動予測に関する研究 (地震火山研究部, 2000)
Study on Stress Field and Forecast of Seismic Activity in the Kanto Region (Seismology and Volcanology Research Department, 2000)
- 第 41 号 電量滴定法による海水中の全炭酸濃度の高精度分析および大気中の二酸化炭素と海水中の全炭酸の放射性炭素同位体比の測定 (石井雅男・吉川久幸・松枝秀和, 2000)
Coulometric Precise Analysis of Total Inorganic Carbon in Seawater and Measurements of Radiocarbon for the Carbon Dioxide in the Atmosphere and for the Total Inorganic Carbon in Seawater (I. Masao, H. Y. Inoue and H. Matsueda, 2000)
- 第 42 号 気象研究所/数値予報課統一非静力学モデル (斉藤和雄・加藤輝之・永戸久喜・室井ちあし, 2001)
Documentation of the Meteorological Research Institute / Numerical Prediction Division Unified Nonhydrostatic Model (Kazuo Saito, Teruyuki Kato, Hisaki Eito and Chiashi Muroi, 2001)

- 第 43 号 大気および海水中のクロロフルオロカーボン類の精密測定と気象研究所クロロフルオロカーボン類標準ガスの確立 (時枝隆之・井上(吉川)久幸, 2004)
Precise measurements of atmospheric and oceanic chlorofluorocarbons and MRI chlorofluorocarbons calibration scale (Takayuki Tokieda and Hisayuki Y. Inoue, 2004)
- 第 44 号 PostScript コードを生成する描画ツール"PLOTIPS"マニュアル (加藤輝之, 2004)
Documentation of "PLOTIPS": Outputting Tools for PostScript Code (Teruyuki Kato, 2004)
- 第 45 号 気象庁及び気象研究所における二酸化炭素の長期観測に使用された標準ガスのスケールとその安定性の再評価に関する調査・研究 (松枝秀和・須田一人・西岡佐喜子・平野礼朗・澤 庸介・坪井一寛・堤 之智・神谷ひとみ・根本和宏・長井秀樹・吉田雅司・岩野園城・山本 治・森下秀昭・鎌田匡俊・和田 晃, 2004)
Re-evaluation for scale and stability of CO₂ standard gases used as long-term observations at the Japan Meteorological Agency and the Meteorological Research Institute (Hidekazu Matsueda, Kazuto Suda, Sakiko Nishioka, Toshirou Hirano, Yousuke, Sawa, Kazuhiro Tuboi, Tsutumi, Hitomi Kamiya, Kazuhiro Nemoto, Hideki Nagai, Masashi Yoshida, Sonoki Iwano, Osamu Yamamoto, Hideaki Morishita, Kamata, Akira Wada, 2004)
- 第 46 号 地震発生過程の詳細なモデリングによる東海地震発生の推定精度向上に関する研究 (地震火山研究部, 2005)
A Study to Improve Accuracy of Forecasting the Tokai Earthquake by Modeling the Generation Processes (Seismology and Volcanology Research Department, 2005)
- 第 47 号 気象研究所共用海洋モデル (MRI.COM) 解説 (海洋研究部, 2005)
Meteorological Research Institute Community Ocean Model (MRI.COM) Manual (Oceanographical Research Department, 2005)
- 第 48 号 日本海降雪雲の降水機構と人工調節の可能性に関する研究 (物理気象研究部・予報研究部, 2005)
Study of Precipitation Mechanisms in Snow Clouds over the Sea of Japan and Feasibility of Their Modification by Seeding (Physical Meteorology Research Department, Forecast Research Department, 2005)
- 第 49 号 2004 年日本上陸台風の概要と環境場 (台風研究部, 2006)
Summary of Landfalling Typhoons in Japan, 2004 (Typhoon Research Department, 2006)
- 第 50 号 栄養塩測定用海水組成標準の 2003 年国際共同実験報告 (青山道夫, 2006)
2003 Intercomparison Exercise for Reference Material for Nutrients in Seawater in a Seawater Matrix (Michio Aoyama, 2006)
- 第 51 号 大気および海水中の超微量六フッ化硫黄(SF₆)の測定手法の高度化と SF₆ 標準ガスの長期安定性の評価 (時枝隆之、石井雅男、斉藤 秀、緑川 貴, 2007)
Highly developed precise analysis of atmospheric and oceanic sulfur hexafluoride (SF₆) and evaluation of SF₆ standard gas stability (Takayuki Tokieda, Masao Ishii, Shu Saito and Takashi Midorikawa, 2007)
- 第 52 号 地球温暖化による東北地方の気候変化に関する研究 (仙台管区气象台、環境・応用気象研究部, 2008)
Study of Climate Change over Tohoku District due to Global Warming (Sendai District Meteorological Observatory, Atmospheric Environment and Applied Meteorology Research Department, 2008)
- 第 53 号 火山活動評価手法の開発研究 (地震火山研究部, 2008)
Studies on Evaluation Method of Volcanic Activity (Seismology and Volcanology Research Department, 2008)
- 第 54 号 日本における活性炭冷却捕集およびガスクロ分離による気体計数システムによる ⁸⁵Kr の測定システムの構築および 1995 年から 2006 年の測定結果 (青山道夫、藤井憲治、廣瀬勝己、五十嵐康人、磯貝啓介、新田 済、Hartmut Sartorius, Clemens Schlosser, Wolfgang Weiss, 2008)
Establishment of a cold charcoal trap-gas chromatography-gas counting system for ⁸⁵Kr measurements in Japan and results from 1995 to 2006 (Michio Aoyama, Kenji Fujii, Katsumi Hirose, Yasuhito Igarashi, Keisuke Isogai, Wataru Nitta, Hartmut Sartorius, Clemens Schlosser, Wolfgang Weiss, 2008)
- 第 55 号 長期係留による 4 種類の流速計観測結果の比較 (中野俊也、石崎 廣、四竈信行, 2008)
Comparison of Data from Four Current Meters Obtained by Long-Term Deep-Sea Moorings (Toshiya Nakano, Hiroshi Ishizaki and Nobuyuki Shikama, 2008)
- 第 56 号 CMIP3 マルチモデルアンサンブル平均を利用した将来の海面水温・海氷分布の推定 (水田 亮、足立恭将、行本誠史、楠 昌司, 2008)
Estimation of the Future Distribution of Sea Surface Temperature and Sea Ice Using the CMIP3 Multi-model Ensemble Mean (Ryo Mizuta, Yukimasa Adachi, Seiji Yukimoto and Shoji Kusunoki, 2008)
- 第 57 号 閉流路中のフローセルを用いた分光光度法自動分析装置による海水の高精度 pH_T 測定 (斉藤 秀、石井雅男、緑川 貴、井上 (吉川) 久幸, 2008)
Precise Spectrophotometric Measurement of Seawater pH_T with an Automated Apparatus using a Flow Cell in a Closed Circuit (Shu Saito, Masao Ishii, Takashi Midorikawa and Hisayuki Y. Inoue, 2008)
- 第 58 号 栄養塩測定用海水組成標準の 2006 年国際共同実験報告 (青山道夫, J. Barwell-Clarke, S. Becker, M. Blum, Braga E.S., S. C. Coverly, E. Czobik, I. Dahllöf, M. Dai, G. O. Donnell, C. Engelke, Gwo-Ching Gong, Gi-Hoon Hong, D. J. Hydes, Ming-Ming Jin, 葛西広海, R. Kerouel, 清本容子, M. Knockaert, N. Kress, K. A. Kroglund, 熊谷正光, S. Leterme, Yarong Li, 増田真次, 宮尾 孝, T. Moutin, 村田昌彦, 永井直樹, G. Nausch, A. Nybakk, M. K. Ngirchchol, 小川浩史, J. van Ooijen, 太田秀和, J. Pan, C. Payne, O. Pierre-Duplessix, M. Pujon-Pay, T. Raabe, 齊藤一浩, 佐藤憲一郎, C. Schmidt, M. Schuett, T. M. Shammon, J. Sun, T. Tanhua, L. White, E.M.S. Woodward, P. Worsfold, P. Yeats, 芳村 毅, A. Youénu, Jia-Zhong Zhang, 2008)
2006 Inter-laboratory Comparison Study for Reference Material for Nutrients in Seawater (M. Aoyama, J. Barwell-Clarke, S. Becker, M. Blum, Braga E. S., S. C. Coverly, E. Czobik, I. Dahllöf, M. H. Dai, G. O. Donnell, C. Engelke, G. C. Gong, Gi-Hoon Hong, D. J. Hydes, M. M. Jin, H. Kasai, R. Kerouel, Y. Kiyomono, M. Knockaert, N. Kress, K. A. Kroglund, M.

- Kumagai, S. Leterme, Yarong Li, S. Masuda, T. Miyao, T. Moutin, A. Murata, N. Nagai, G. Nausch, M. K. Ngirchchol, A. Nybakk, H. Ogawa, J. van Ooijen, H. Ota, J. M. Pan, C. Payne, O. Pierre-Duplessix, M. Pujo-Pay, T. Raabe, K. Saito, K. Sato, C. Schmidt, M. Schuett, T. M. Shammon, J. Sun, T. Tanhua, L. White, E.M.S. Woodward, P. Worsfold, P. Yeats, T. Yoshimura, A. Youéno, J. Z. Zhang, 2008)
- 第 59 号 気象研究所共用海洋モデル(MRI.COM)第 3 版解説(辻野博之, 本井達夫, 石川一郎, 平原幹俊, 中野英之, 山中吾郎, 安田珠幾, 石崎廣 (気象研究所海洋研究部), 2010)
- Reference manual for the Meteorological Research Institute Community Ocean Model (MRI.COM) Version 3 (Hiroyuki Tsujino, Tatsuo Motoi, Ichiro Ishikawa, Mikitoshi Hirabara, Hideyuki Nakano, Goro Yamanaka, Tamaki Yasuda, and Hiroshi Ishizaki (Oceanographic Research Department), 2010)
- 第 60 号 栄養塩測定用海水組成標準の 2008 年国際共同実験報告 (青山道夫, Carol Anstey, Janet Barwell-Clarke, François Baurand, Susan Becker, Marguerite Blum, Stephen C. Coverly, Edward Czobik, Florence D' amico, Ingela Dahllöf, Minhan Dai, Judy Dobson, Magali Duval, Clemens Engelke, Gwo-Ching Gong, Olivier Grosso, 平山篤史, 井上博敬, 石田雄三, David J. Hydes, 葛西広海, Roger Kerouel, Marc Knockaert, Nurit Kress, Katherine A. Kroglund, 熊谷正光, Sophie C. Leterme, Claire Mahaffey, 光田均, Pascal Morin, Thierry Moutin, Dominique Munaron, 村田昌彦, Günther Nausch, 小川浩史, Jan van Ooijen, Jianming Pan, Georges Paradis, Chris Payne, Olivier Pierre-Duplessix, Gary Prove, Patrick Raimbault, Malcolm Rose, 齊藤一浩, 齊藤宏明, 佐藤憲一郎, Cristopher Schmidt, Monika Schütt, Theresa M. Shammon, Solveig Olafsdottir, Jun Sun, Toste Tanhua, Sieglinde Weigelt-Krenz, Linda White, E. Malcolm. S. Woodward, Paul Worsfold, 芳村毅, Agnès Youéno, Jia-Zhong Zhang, 2010)
- 2008 Inter-laboratory Comparison Study of a Reference Material for Nutrients in Seawater (青山道夫, Carol Anstey, Janet Barwell-Clarke, François Baurand, Susan Becker, Marguerite Blum, Stephen C. Coverly, Edward Czobik, Florence D' amico, Ingela Dahllöf, Minhan Dai, Judy Dobson, Magali Duval, Clemens Engelke, Gwo-Ching Gong, Olivier Grosso, 平山篤史, 井上博敬, 石田雄三, David J. Hydes, 葛西広海, Roger Kerouel, Marc Knockaert, Nurit Kress, Katherine A. Kroglund, 熊谷正光, Sophie C. Leterme, Claire Mahaffey, 光田均, Pascal Morin, Thierry Moutin, Dominique Munaron, 村田昌彦, Günther Nausch, 小川浩史, Jan van Ooijen, Jianming Pan, Georges Paradis, Chris Payne, Olivier Pierre-Duplessix, Gary Prove, Patrick Raimbault, Malcolm Rose, 齊藤一浩, 齊藤宏明, 佐藤憲一郎, Cristopher Schmidt, Monika Schütt, Theresa M. Shammon, Solveig Olafsdottir, Jun Sun, Toste Tanhua, Sieglinde Weigelt-Krenz, Linda White, E. Malcolm. S. Woodward, Paul Worsfold, 芳村毅, Agnès Youéno, Jia-Zhong Zhang, 2010)
- 第 61 号 強雨をもたらす線状降水帯の形成機構等の解明及び降水強度・移動速度の予測に関する研究 (大阪管区気象台・彦根地方気象台・京都地方気象台・奈良地方気象台・和歌山地方気象台・神戸海洋気象台・松江地方気象台・鳥取地方気象台・舞鶴海洋気象台・広島地方気象台・徳島地方気象台・予報研究部, 2010)
- Studies on formation process of line-shaped rainfall systems and predictability of rainfall intensity and moving speed (Osaka District Meteorological Observatory, Hikone Local Meteorological Observatory, Kyoto Local Meteorological Observatory, Nara Local Meteorological Observatory, Wakayama Local Meteorological Observatory, Kobe Marine Observatory, Matsue Local Meteorological Observatory, Tottori Local Meteorological Observatory, Maizuru Marine Observatory, Hiroshima Local Meteorological Observatory, Tokushima Local Meteorological Observatory AND Forecast Research Department, 2010)
- 第 62 号 WWRP 北京オリンピック 2008 予報実証/研究開発プロジェクト(齊藤和雄, 國井勝, 原昌弘, 瀬古弘, 原旅人, 山口宗彦, 三好建正, 黄偉健, 2010)
- WWRP Beijing Olympics 2008 Forecast Demonstration/Research and Development Project (B08FDP/RDP) (Kazuo Saito, Masaru Kunii, Masahiro Hara, Hiromu Seko, Tabito Hara, Munchiko Yamaguchi, Takemasa Miyoshi and Wai-kin Wong, 2010)
- 第 63 号 東海地震の予測精度向上及び東南海・南海地震の発生準備過程の研究, 地震火山研究部, 2011)
- Improvement in prediction accuracy for the Tokai earthquake and research of the preparation process of the Tonankai and the Nankai earthquakes (Seismology and Volcanology Research Department, 2011)